Tufts UNIVERSITY | School of Dental Medicine

Tissue Engineering Strategies for Alveolar Bone Regeneration Using Silk-Based 3D-Printed Composite Scaffolds

A Thesis submitted by

Ayman A. Banjar

Presented to the Faculty of Tufts University School of Dental Medicine in Partial Fulfillment of the Requirements for the Degree of Doctor of Science in Dentistry

August 2025

Principal Investigator

David L. Kaplan

Dedication

To my mother, whose love and guidance resonate in my heart and continue to light my path, even in her absence..

To my father, who supported me through life and whose memory will always inspire me..

This accomplishment reflects your love and faith, forever engraved in my life..

Thank you for everything..

© 2025 Ayman A. Banjar

Thesis Committee

Thesis Advisor

David L. Kaplan

Professor

Department of Biomedical Engineering

Tufts University School of Engineering

Committee Members

Vincent Fitzpatrick

Research Assistant Professor

Department of Biomedical Engineering

Tufts University School of Engineering

Guzin Uzel

Assistant Professor and Director of Research Education

Department of Periodontology

Tufts University School of Dental Medicine

Nadeem Y. Karimbux

Professor and Dean

Department of Periodontology

Tufts University School of Dental Medicine

Acknowledgment

I would like to express my gratitude to my advisor, David Kaplan, for welcoming me into his lab and giving me the opportunity to pursue my doctoral research in a high-level learning environment that was entirely new to me. His continuous support, guidance, and constructive feedback were invaluable throughout this journey. I am thankful for his mentorship and for his trust.

My sincere thanks to Vincent Fitzpatrick for his mentorship and for serving on my thesis committee. From the beginning of my time in the lab, he provided me with all the training and guidance that helped me develop the skills needed to carry out my research. His continued support, even remotely, was greatly appreciated. I would like to thank Dr. Guzin Uzel and Dean Nadeem Karimbux for serving on my thesis committee. Dr. Uzel, in her role as DSc program director, was always supportive and readily available whenever I needed assistance or guidance. I am grateful for her help throughout my study. I also appreciate Dean Karimbux for his time and thoughtful feedback during the review and revision process of my thesis.

I would like to thank the Kaplan Lab staff, Carmen Preda, Laura Place, and Gwen Buchanan. They were always supportive and willing to help with any issues that arose, and provided me with the training and guidance I needed to navigate the lab. I am especially thankful to my colleagues Vathanai Bhunyanaphakul (Benz) and Nilotpal Majumder. Benz and I started this journey together, and I learned a lot from him early on. Nilotpal's support and valuable input helped me push my projects forward. I am also grateful to my lab colleagues, Chunmai Li, Eward Gorden, Charlotte Jacobus, Riley Patten, Glenn Leung, and Merve Türemen. Thank you for your readiness to help, and your overall positive spirit made the day-to-day experience easier.

To my siblings, Amr, Arwa, and Atheer, thank you for always being there for me. Your support and check-ins from afar made tough days easier and reminded me that I'm never alone, even from miles away.

My dearest friends and Boston companions, Eric and Ricardo, your support during my doctoral journey has meant more to me than I can put into words. You were always there to listen when I needed to vent and to lift my spirit when things got tough. You made hard days lighter and the good ones even better. I will always be grateful for everything you have done for me.

To my little dog, Maya, who came into my life during my doctoral studies and made everything better. Thank you for patiently waiting through the long lab days and for always greeting me with pure joy.

Abstract

Successful regeneration of the alveolar ridge requires biomaterials that support both osteogenesis and vascularization. Combining biomaterials with 3D printing technology supports the fabrication of customized scaffolds with controlled architecture tailored to bone repair. This thesis explores two distinct tissue engineering strategies for bone regeneration using silk fibroin (SF)-based 3D printed scaffolds. The first approach involves SF-biphasic calcium phosphate (SF-BCP) scaffolds functionalized with bone morphogenetic protein-2 (BMP-2) and platelet-derived growth factor (PDGF), delivered using a heparinized hyaluronic acid-based hydrogel injected inside the scaffolds. The second strategy employed a cell co-culture-based regeneration approach using SF-bioactive glass (SF-BG) scaffolds designed to support the direct culture of human mesenchymal stem cells (hMSCs) with human umbilical vein endothelial cells (HUVECs) for vascularized bone tissue regeneration. The SF-BCP scaffolds were fabricated using an extrusion-based 3D printing method and characterized for their mechanical, structural, and rheological properties. Functionalization of the scaffolds with BMP-2 significantly enhanced early osteogenic differentiation, while PDGF had a limited effect. In parallel, SF-BG scaffolds were developed to support direct co-culture. The rheological and mechanical properties were suitable for the goals, but the printing process was sensitive to small changes in formulation and thus, less reliable. Co-culture conditions were optimized on tissue culture polystyrene (TCPS) and then translated to the 3D printed scaffolds. The cells successfully adhered to the constructs, proliferated, and maintained increasing levels of metabolic activity over time. The scaffolds supported extracellular matrix deposition, with features varying depending on the ratios of hMSCs and HUVECs in the co-cultures. Altogether, this work demonstrates the potential of SF-based 3D printed scaffolds to support bone regeneration through bioengineering strategies tailored to enhance osteogenic outcomes. The findings of this work offer a foundation for the future design of silk-based scaffolds with potential applications in the regeneration of alveolar and craniofacial bone tissues.

Table of Contents

Thesis Committee ..... **IV**

Thesis Advisor ..... *IV*

Committee Members ..... *IV*

Acknowledgment ..... **V**

Abstract ..... **VII**

List of Tables ..... **X**

List of Supplementary Figures ..... **XVIII**

List of Abbreviations ..... **XX**

Chapter 1: Introduction **1**

1.1. Background on Bone Tissue *2*

1.2. Bone Loss in the Alveolar Ridge *3*

1.3. Clinical Challenges and Current Regenerative Strategies *4*

1.4. Tissue Engineering as an Alternative Approach *8*

1.5. Gap in Knowledge *15*

1.6. Objectives and Thesis Organization *17*

Chapter 2: Growth Factor Functionalized Silk-Based 3D-Printed Scaffolds: A Bioengineered Approach for Alveolar Bone Regeneration. **19**

2.1. Abstract *19*

2.2. Introduction *20*

2.3. Materials and Methods *21*

2.4. Results *31*

2.5. Discussion *52*

2.5.1. Material Development and Structural Properties *52*

2.5.2. Biological Performance and Osteogenic Potential *54*

2.5.3. Growth Factors Delivery: Release Kinetics and Osteogenic Effect *55*

2.6. Future Directions *59*
2.7. Conclusion *60*
2.8. Supplementary Figures *62*

Chapter 3: Silk-Bioactive Glass 63S Scaffolds for hMSC and HUVEC Co-culture in Bone Regeneration **67**

3.1. Abstract *67*
3.2. Introduction *68*
3.3. Materials and Methods *71*
3.4. Results and Discussion *78*
3.4.1. Material characterization: Mechanical Assessment and Printability *78*
3.4.2. Co-culture Determination *83*
3.4.3. Biological performance of SF-BG scaffolds *88*
3.5. Future Directions *100*
3.6. Conclusion *101*
3.7. Supplementary Figures *102*

References **105**

List of Tables

Table 2-1. Bone cement compositions used for mechanical testing. 23

Table 2-2. Compositions of inks used for rheometric analysis. 24

Table 2-3. Printability parameters of the SF-biphasic ceramic bone cement ink containing silk fibroin. Values were measured from scaffolds printed using a 30% infill grid structure. Six sites were analyzed from three independent samples (n = 3)..... 36

Table 3-1. Media compositions..... 74

Table 3-2. Primers used for Real-Time quantitative PCR. 76

List of Figures

Figure 2-1. Set up for compressive mechanical testing of cylindrical samples using an Instron 3366 universal testing machine. **(a)** Custom stainless steel mold components used for fabricating cylindrical specimens for material bulk testing **(b)** Representative dried cylindrical scaffold samples after demolding. **(c)** A sample positioned for uniaxial compression testing under a 1 kN load cell. Scale bar = 6 mm. 23

Figure 2-2. (a) Compressive strength and **(b)** compressive modulus (MPa) of different bone cement material compositions under dry and wet conditions. Bars represent mean ± SD (n = 5). 32

Figure 2-3. Comparison of compressive strength **(left)** and compressive modulus **(right)** of the selected bone cement material to trabecular bone in the human mandible, based on values reported by Misch et al. (1999). The dashed lines mark the upper and lower limits of cortical and trabecular bone mechanical properties. Bars represent mean ± SD. For reference, the cortical bone range is shaded in pink, and the trabecular bone range is shaded in green. 33

Figure 2-4. Rheological characterization of SF-BCP bone cement. **(a)** Flow behavior, **(b)** amplitude sweep, **(c)** frequency sweep, and **(a)** time sweep tests. 34

Figure 2-5. Rheological characterization of bone cement without SF inclusion. (a) Flow behavior, **(b)** amplitude sweep, **(c)** frequency sweep, and **(a)** time sweep tests. 35

Figure 2-6. Microscopic images of printed scaffold filaments and pores: **(a)** scaffold with silk, showing well-defined geometry; **(b)** scaffold without silk, showing irregular and distorted shapes. **(c)** Macroscopic view of the printed grid structure with silk (top) and without silk (bottom). Scale bar = 200 μm. 36

Figure 2-7. Characterization of the SF-BCP bone scaffolds. **(a)** 3D printed cylindrical scaffold. SEM for 3D printed constructs showcasing controlled deposition of filament and macroporosity

(b) exterior perimeter **(c)** top view **(d)** interconnected internal network **(e)** filament size and microporosity **(f)** surface roughness **(g)** BCP particles embedded in the SF matrix. 37
Figure 2-8. A critical-size defect in a mandibular model restored with a 3D printed SF-BCP scaffold 38
Figure 2-9. MTT hMSCs viability exposed to media with scaffold dissolution products (n = 3). 39
Figure 2-10. Brightfield images of hMSCs seeded on SF-BCP scaffolds with hydrogel after days 7 (top row) and 35 (bottom row). Scaffolds were maintained in either GM, OM, or functionalized with BMP-2, PDGF, or both factors in OM. Scale bars = 200 µm. 39
Figure 2-11. Alamar Blue assay (n = 3) showing metabolic activity of hMSCs over 28 days. Conditions include TCPS in GM (TCPS-GM) and OM (TCPS-OM), scaffolds without hydrogel in GM (USGM) and OM (USOM), and scaffolds with hydrogel in GM (HSGM) and OM (HSOM). . 40
Figure 2-12. SEM images of SF-BCP scaffolds supplemented with hydrogel and seeded with hMSCs and cultured for 7 and 35 days in **(a)** growth media and **(b)** osteogenic media, showing cell attachment, scaffold coverage, and extracellular matrix formation at various magnifications. 42
Figure 2-13. Representative SF-BCP scaffolds after 35 days of culture with hMSCs. **(a)** Scaffolds in GM and OM. **(b)** scaffolds cultured in OM and functionalized with BMP-2, PDGF, or both factors. Visible matrix deposition was observed in all osteogenic conditions, with varying degrees of pore bridging and surface coverage. Scale bar = 1 mm. 43
Figure 2-14. Osteoinductivity of scaffolds supplemented with hydrogel. Normalized ALP activity after 21 days of culture with hMSCs in GM (HSGM) and OM (HSOM). Each bar represents the mean ± standard deviation (n = 9). Representative ALP staining on day 21 shows a scaffold in growth medium (bottom left) and another in osteogenic medium (bottom right). Statistical analysis was performed using independent samples t-test ****$p < 0.0001$. Scale bars = 2 mm. 43
Figure 2-15. Immunofluorescent staining of Collagen I (COL-I) expression on SF-BCP scaffolds with hydrogel after 35 days of incubation. Representative images show COL-I (green), nuclei

(blue), and actin (red) staining under different conditions: scaffolds cultured in GM, OM, and functionalized with BMP-2, PDGF, and BMP-2 + PDGF (BP). Scale bar = 100 μm. 44
Figure 2-16. Quantification of COL-I fluorescence intensity normalized to the GM control. Conditions include scaffolds cultured in GM (HSGM), OM (HSOM), and scaffolds functionalized with BMP-2, PDGF, and BMP-2 + PDGF (BP). 44
Figure 2-17. Immunofluorescent staining of Collagen X (COL-X) expression on SF-BCP scaffolds with hydrogel after 35 days of incubation. Representative images show COL-X (green), nuclei (blue), and actin (red) staining under different conditions: scaffolds cultured in GM, OM, and functionalized with BMP-2, PDGF, and BMP-2 + PDGF (BP). Scale bar = 100 μm. 45
Figure 2-18. Quantification of COL-X fluorescence intensity normalized to the GM control. Conditions include scaffolds cultured in GM (HSGM), OM (HSOM), and scaffolds functionalized with BMP-2, PDGF, and BMP-2 + PDGF (BP). 45
Figure 2-19. Osteoconductivity of functionalized scaffolds. (a) Alamar Blue assay (n = 6) showing cell metabolic activity over 21 days **(b)** Normalized ALP activity (n = 9) of the functionalized groups and the HSOM control. Data represent mean ± SD (***p ≤ 0.001). 46
Figure 2-20. Functionalization with BMP-2. SEM images of the functionalized scaffolds after 35 days of culture with hMSCs in osteogenic media showing cell coverage and ECM deposition at different magnifications. 46
Figure 2-21. Functionalization with PDGF. SEM images of the functionalized scaffolds after 35 days of culture with hMSCs in osteogenic media showing cell coverage and ECM deposition at different magnifications. 47
Figure 2-22. Functionalization with combined factors (BMP-2 + PDGF). SEM images of the functionalized scaffolds after 35 days of culture with hMSCs in osteogenic media showing cell coverage and ECM deposition at different magnifications. 48
Figure 2-23. Release kinetics of BMP-2 and PDGF from scaffolds without hydrogel **(a)** BMP-2 and **(b)** PDGF. Conditions: control, growth factors-socked (-S), growth factors-loaded (-L). The

release over time was calculated as a percentage of the initial amount loaded (1 µg of BMP-2, PDGF, or a combination of both growth factors (BP)). Cumulative release over time as a percentage of the total initial amount loaded, with the additional incremental release recorded at each subsequent sampling point. Data represent mean ± SD (n = 3). 50

Figure 2-24. Release kinetics of BMP-2 and PDGF from scaffolds loaded with HA hydrogel. **(a)** BMP-2 and **(b)** PDGF. The growth factor release over time was calculated as a percentage of the initial amount loaded (1 µg of BMP-2, PDGF, or a combination of both growth factors (B/P)). Cumulative release over time as a percentage of the total initial amount loaded, with the additional incremental release recorded at each subsequent sampling point. Samples were analyzed using a commercially available sandwich ELISA kit based on human BMP-2 and PDGF. Data represent mean ± SD (n = 3). 51

Figure 3-1. Mechanical assessment of SF-BGS bone cement bulk properties. **(a)** Prepared cylindrical samples **(b)**, sample positioned in an Instron machine for compression test, **(c)** compressed sample at the end of the compression test. Scale bar = 6 mm. 72

Figure 3-2. Mechanical performance of SF-BG 63S bone cement under compression. (a) compressive strength and **(b)** modulus of cylindrical specimens. Data are presented as mean and ±SD. Asterisks indicate statistically significant difference (****p < 0.0001)..... 78

Figure 3-3. Printability assessment of SF-BG 63S composite ink. (a) Rheological characterization to predict printability includes flow behavior, amplitude sweep, frequency sweep, and time sweep. **(b)** Microscopic images show the pore configuration and extruded filament. **(c)** Top view of a printed SF-BG 63S grid structure. 80

Figure 3-4. 3D printed SF-BG 63S scaffolds with different exterior surface designs**. (a)** Scaffold with a solid exterior (14 x 2.5 mm) and **(b)** scaffold with a porous exterior (11 x 2.5 mm). 81

Figure 3-5. SEM images of 3D printed SF-BG 63S scaffolds. **(a)** Top view of the scaffold showing grid structure. **(b)** Stacked filaments with pore interconnectivity, **(c)** pore. (**d-e)** Filament

microporosity and surface roughness. **(f)** High-magnification image showing BG 63S particles within the SF matrix. 82

Figure 3-6. Alamar Blue assay (n = 3) showing metabolic activity on days (a) 3 and (b) 7 during co-culture optimization in TCPS. Conditions included different mono- and co-cultures with various cell ratios and media compositions. Data are presented as mean values. 83

Figure 3-7. Normalized ALP activity quantification (n = 3) on day 21 in TCPS cultures under different mono- and co-culture conditions with various media compositions. Data were normalized to housekeeping genes and are presented as mean ± SD. 84

Figure 3-8. Gene expression of **(a)** Runx2 and **(b)** OPN on day 7 in TCPS cultures under different mono- and co-culture conditions with various media compositions. Data were normalized to housekeeping genes and are presented as mean ± SD. 87

Figure 3-9. Light microscopy images of hMSCs seeded on SF-BG 63S scaffolds after **(a)** 7 and **(b)** 35 days of culture. Images show samples maintained in growth medium and osteogenic medium. 89

Figure 3-10. Alamar Blue assay (n = 3) showing metabolic activity of hMSCs-seeded SF-BG scaffolds over 35 days. Conditions include tissue culture polystyrene with growth medium (GM-TCPS) and osteogenic medium (OM-TCPS), as well as scaffolds in growth medium (GM-S)... 89

Figure 3-11. SEM images of hMSCs-seeded SF-BG 63S scaffolds on day 35. Conditions include scaffolds in growth medium (left) and osteogenic medium (right)..... 90

Figure 3-12. (a) Alamar Blue assay (n = 3) showing metabolic activity of HUVECs-seeded SF-BG scaffolds over 21 days. Conditions include TCPS with endothelial growth medium (EGM-TCPS) and scaffolds in EGM (EGM-S). **(b)** Light microscopy images of HUVECs seeded on SF-BG 63S scaffolds and cultured in EGM for 21 days. Data presented as mean and ±SD. 90

Figure 3-13. SEM images of HUVECs-seeded SF-BG 63S scaffolds on day 35..... 91

Figure 3-14. Alamar Blue assay (n = 3) showing metabolic activity of co-cultures on SF-BG 63S scaffolds and TCPS over 21 days. Conditions include: **(1)** OM-TCPS – hMSCs cultured in TCPS

in OM, **(2)** 4:1-TCPS – co-culture on TCPS in 1:1 mixed medium, **(3)** 1:1-TCPS – co-culture on TCPS in 1:1 mixed medium, **(4)** OM-S – hMSCs on scaffolds in OM, **(5)** 4:1-S – co-culture on scaffold in 1:1 mixed medium, **(6)** 1:1-S – co-culture on scaffold in 1:1 mixed medium. Data presented as mean and ±SD. 92

Figure 3-15. Gross images of SF-BG 63S scaffolds after 35 days of co-culture with hMSCs and HUVECs at 4:1 (left) and 1:1 (right) cell ratios in mixed OM:EGM media. **(a)** top view of intact scaffolds showing visible ECM coverage over the filaments and pores, more prominent in the 4:1 condition. **(b)** Sectioned scaffolds showing internal ECM structure. Green arrows indicate strand-like structures connecting different fragments of the scaffolds, observed spanning the constructs both externally and internally 93

Figure 3-16. SEM images showing newly formed ECM on SF-BG 63S scaffold co-cultured at a 4:1 cell ratio for 35 days. **(a)** Scaffold morphology and structure, **(b)** and **(c)** filaments extensively covered with new matrix along the surfaces, **(d-f)** pore walls showing ECM coverage and partial occlusion at different regions on the scaffolds. 94

Figure 3-17. SEM images showing filament coverage and cellular interaction on SF-BG 63S scaffold co-cultured at a 4:1 cell ratio for 35 days. **(a-b)** Filament coverage with dense fibrillar ECM **(c)**, higher magnification showing a cell embedded within the ECM with visible extensions; **(d-f)** another filament showing similar matrix coverage with globular surface features and nodules along the ECM. 94

Figure 3-18. SEM images at higher magnification showing dense fibrillar ECM with globular surface features and areas of cell attachments on SF-BG 63S scaffold co-cultured at a 4:1 cell ratio and cultured for 35 days. Images were captured from various regions across the scaffold. 95

Figure 3-19. SEM images of an SF-BG 63S scaffold seeded with hMSCs and HUVECs at a 1:1 ratio and cultured for 35 days. **(a–c)** Macropores with new ECM formation. **(d–e)** Images showing

Surfaces of scaffold filaments and pore walls covered with cellular growth and ECM deposition. **(f)** cells embedded and adhered to the surfaces of a filament. 96

Figure 3-20. SEM images at higher magnification showing various regions across an SF-BG 63S scaffold seeded with hMSCs and HUVECs at a 1:1 ratio and cultured for 35 days. **(a–i)** Images showing the surfaces of scaffold filaments and pore walls covered with newly formed ECM and cells embedded and adhered within the matrix. 97

Figure 3-21. SEM images showing strand-like structures formed on SF-BG 63S scaffolds co-cultured at a 4:1 cell ratio for 35 days. **(a)** Strand-like structure spanning between two scaffold fragments. **(b–d)** Surface topography of strands at different magnifications. **(e–f)** High-magnification images showing cellular morphology and ECM organization across the strand surface. 98

Figure 3-22. SEM images showing strand-like structures formed on SF-BG 63S scaffolds co-cultured at a 1:1 cell ratio for 35 days. **(a)** Strand-like structure extension between two scaffold fragments. **(b)** Surface topography and **(c)** cells embedded within the matrix. **(e–f)** Another strand spans along the external surface of the scaffolds at different magnifications. 98

Figure 3-23. ALP staining of SF-BG 36S scaffolds at day 21 under different culture conditions. From left to right: hMSCs in GM, hMSCs in OM, HUVECs in EGM, co-cultures of hMSCs:HUVECs at 4:1 and 1:1 ratio in a blend of 1:1 OM:EGM. Purple staining reflects ALP activity and early osteogenic differentiation. 99

List of Supplementary Figures

Figure S2-1. SEM images for scaffolds without hydrogel after 7 days of culture with hMSCs in **(a)** GM(left) and OM (right), **(b)** Scaffolds functionalized with the factors (BMP-2, PDGF, or BMP-2 + PDGF) encapsulated within the structure of the printed constructs. 62

Figure S 2-3. Runx2 immunofluorescence staining of hMSCs on TCPS at day 14. Cells were seeded in a 24-well plate containing scaffolds, and some cells adhered to the bottom surface of the well plate. This experiment was performed to optimize the immunofluorescence protocol and confirm the presence of Runx2 before staining the scaffolds. **Green**: Runx2 expression; **Blue:** nuclei. Scale bar = 100 μm. 63

Figure S 2-4. Osteopontin (OPN) immunofluorescence staining of hMSCs on TCPS at day 21. Cells were seeded in a 24-well plate containing scaffolds, and some cells adhered to the bottom surface of the well plate. This experiment was performed to optimize the immunofluorescence protocol and confirm the presence of OPN before staining the scaffolds. **Green**: OPN expression; **Blue:** nuclei. Scale bar = 100 μm. 64

Figure S 2-5. COL-X immunofluorescence staining of hMSCs on TCPS at day 28. Cells were seeded in a 24-well plate containing scaffolds, and some cells adhered to the bottom surface of the well plate. This experiment was performed to optimize the immunofluorescence protocol and confirm the presence of COL-X before staining the scaffolds. **Green**: OPN expression; **Blue:** nuclei; **Red:** Actin. Scale bar = 100 μm. 65

Figure S 2-6. Von Kossa staining of calcium phosphate mineral deposition on tissue culture plates. Representative images show hMSC cultures under various conditions after 21 days. Scaffolds were removed prior to staining, and mineralized matrix deposited on the well bottoms was visualized. Cells maintained in growth media (GM) showed no mineralization, while osteogenic media (OM) induced moderate calcium deposition. BMP-2 supplementation resulted

in extensive mineralization, PDGF alone led to moderate mineral deposition, whereas the combination of BMP-2 and PDGF produced notable mineralization. Scale bar = 200 μm. 66
Figure S 3-1. Alamar Blue assay (n = 3) showing metabolic activity on days **(a)** 3 and **(b)** 7 during co-culture optimization in TCPS. Conditions included different mono- and co-cultures with various cell ratios and media compositions, without osteogenic differentiation. Data are presented as mean values. (Shown for reference only). 102
Figure S 3-2. Alamar Blue assay (n = 3) from an independent experiment assessing the metabolic activity of hMSCs and HUVECs co-culture on SF-BG 63S scaffolds and TCPS over 21 days. Conditions include: **(1)** GM-TCPS – hMSCs cultured in TCPS in GM, **(2)** OM-TCPS – hMSCs cultured in TCPS in OM, **(3)** 4:1-TCPS – co-culture on TCPS in 1:1 mixed medium, **(4)** 1:1-TCPS – co-culture on TCPS in 1:1 mixed medium, **(5)** GM-S – hMSCs on scaffolds in GM, **(6)** OM-S – hMSCs on scaffolds in OM, **(7)** 4:1-S – co-culture on scaffold in 1:1 mixed medium, **(8)** 1:1-S – co-culture on scaffold in 1:1 mixed medium. Data presented as mean and ± SD. 103
Figure S 3-3. Normalized ALP activity for SF-BG 63S scaffolds under various seeding conditions on day 21. Conditions included TCPS controls with hMSCs in GM and OM, HUVECs in EGM; co-culture on TCPS at 4:1 and 1:1 cell ratio in 1:1 mixed media; hMSCs monoculture on scaffolds in GM (GM-S), and OM (OM-S), HUVECs in EGM (EGM-S); co-culture on scaffolds at 4:1 (4:1-S) and 1:1 (1:1-S0 in 1:1 mixed media. Data presented as mean and ± SD. Due to compromised testing conditions, the results are presented for reference only 104

List of Abbreviations

45S5	The original bioactive glass developed by Larry Hench (known as Bioglass®)
63S	A sodium-free formula of bioactive glass
α-TCP	Alpha-Tricalcium Phosphate
β-TCP	Beta-Tricalcium Phosphate
a.u.	Arbitrary unit
ADO	Alveolar Destruction Osteogenesis
ALP	Alkaline Phosphatase
AM	Additive Manufacturing
B/P	Combined BMP-2 and PDGF Conditions
BCIP/NBT	5-bromo-4-chloro-3-indolyl phosphate/nitro blue tetrazolium
BCP	Biphasic Calcium Phosphate
BG	Bioactive Glass
BMP-2	Bone Morphogenetic Protein-2
BMPs	Bone Morphogenetic Proteins
B. mori	Bombyx mori silkworm
BSA	Bovine Serum Albumin
BSP	Bone Sialoprotein
CaP	Calcium Phosphate
COL-I	Collagen Type I
COL-X	Collagen Type X
CT	Computed Tomography
DICOM	Digital Imaging and Communications in Medicine
diH2O	Deionized Water
DIW	Direct Ink Writing
DMSO	Dimethyl Sulfoxide
ECM	Extracellular Matrix
EGM	Endothelia growth medium
ELISA	Enzyme-Linked Immunosorbent Assay
Extralink®	A thiol-reactive crosslinker, polyethylene glycol diacrylate
FDM	Fused Deposition Modeling
G'	Storage Modulus

G”	Loss Modulus
GAPDH	Glyceraldehyde 3-phosphate dehydrogenase
GBR	Guided Bone Regeneration
Gelin™-S	A thiol-modified gelatin
GM	Growth Medium
HA	Hyaluronic Acid
HAp	Hydroxyapatite
HCA	Hydroxycarbonate Apatite
hiNSCs	Human Induced Neural Stem Cells
HMDS	Hexamethyldisilazane
hMSCs	Human Mesenchymal Stem Cells
HSGM	Hydrogel-Scaffold in Growth Medium
HSOM	Hydrogel-Scaffold in Osteogenic Medium
HUVEC	Human Umbilical Vein Endothelial Cell
HyStem®-HP	A thiol-modified Hyaluronan
ImageJ	Open-source software focused on biological image analysis
LEV	Linear Viscoelastic
LiBr	Lithium Bromide
MRI	Magnetic Resonance Imaging
MSCs	Mesenchymal Stem Cells
MTT	3-(4,5-dimethylthiazol-2-yl)-2,5-diphenyltetrazolium bromide
NGF	Nerve Growth Factor
OCN	Osteocalcin
OM	Osteogenic Medium
OPN	Osteopontin
PBS	Phosphate-Buffered Saline
PDGF	Platelet-Derived Growth Factor
PDL(s)	Periodontal Ligament(s)
PEG	Polyethylene Glycol
PLA	Polylactic Acid
rh-PDGF	Recombinant Human Platelet-Derived Growth Factor
rhBMP-2	Recombinant Human Bone Morphogenetic Protein-2
Runx2	Runt-related Transcription Factor 2
SEM	Scanning Electron Microscopy

SF	Silk Fibroin
SMAD(1/5/8)	Intracellular effectors for BMP-2 protein transcription
SMAD4	Intracellular effectors for BMP-2 protein transcription
STL	Stereolithography File Format
TCP	Tricalcium Phosphate
TCPS	Tissue Culture Polystyrene
TGF-b	Transforming Growth Factor Beta
USGM	Unloaded Scaffold in Growth Medium
USOM	Unloaded Scaffold in Osteogenic Medium

Chapter 1: Introduction

Regenerating the alveolar bone remains a significant clinical challenge in dentistry. The alveolar ridge is highly susceptible to resorption due to infections or chronic inflammation of the tooth-supporting tissues, as seen in periodontitis.[1, 2] Approximately 47% of adults in the U.S. suffer from periodontal disease, with prevalence rising to 70% in individuals aged 65 and older.[3-5] Periodontitis is the leading cause of tooth loss, contributing to edentulism rates as high as 20% in older adults.[3] The absence of mechanical stimulation following tooth loss further accelerates bone resorption.[6] If left untreated, these conditions lead to significant bone loss, limiting restorative options and complicating clinical management.[6, 7] There is a growing need for strategies that integrate biology and biomaterials to design bone scaffolds that guide bone regeneration. A comprehensive understanding of bone biology, combined with innovation in biomaterials and growth factors delivery strategies, is necessary to develop targeted solutions for alveolar bone regeneration that overcome the limitations of current bone grafting techniques and offer predictable clinical outcomes.[8-10]

Advancements in 3D printing and biomaterials have enabled the design of patient-specific scaffolds with precise control over geometry and architecture that aligns with both mechanical and biological requirements.[9, 11] This thesis explores tissue engineering strategies for alveolar bone regeneration by utilizing silk-based composite scaffolds fabricated via 3D printing. Two distinct approaches were investigated: (1) functionalization of silk-biphasic calcium phosphate scaffolds with hyaluronic acid-based hydrogel for localized delivery of growth factor and morphogen, and (2) co-culture of human mesenchymal stem cells (hMSCs) and endothelial cells on silk-bioactive glass scaffolds to enhance osteogenesis through cell-to-cell interaction. These in vitro studies aimed to optimize materials for fabricating scaffolds and evaluating their mechanical and biological performance, with the long-term goal of advancing bioengineered solutions for the reconstruction of critical-size defects in the alveolar ridge.

1.1. Background on Bone Tissue

Bone is a specialized connective tissue that provides the body with structural support, enables its movement, protects its vital organs, and stores minerals and hematopoietic cells. It is composed of approximately 30% organic phase and 70% inorganic mineral phase.[12] The organic component includes both cellular and extracellular matrix (ECM). Cells comprise about 2% and include osteoblasts, osteocytes, and osteoclasts. The remaining organic matrix is predominantly composed of type I collagen (COL-I) and serves as the primary structural protein.[12] In addition to collagen, the matrix contains non-collagenous proteins such as osteocalcin, osteonectin, bone sialoprotein, and fibronectin. The inorganic mineral phase mainly consists of a nanocrystalline calcium phosphate structure called hydroxyapatite (HAp), dispersed within the collagen network.[12, 13] Bone tissue is classified into two main types: cortical bone and trabecular bone.[14] Cortical bone forms the dense outer layer that provides strength and support, and is covered by the perigonium, which is a fibrous connective tissue rich in osteoprogenitor cells and blood supply.[14, 15] In contrast, trabecular bone is a porous inner structure filled with bone marrow and contributes to the lightweight of bone, and plays a crucial role in bone turnover by providing the necessary cells for bone remodeling and regeneration.[15, 16]

This tissue is dynamic in nature and undergoes continuous remodeling to adapt its structure to growth, mechanical stress and to repair microdamage. In this process, bone tissue is renewed through a balanced cycle of resorption and formation, coordinated by the activity of osteoblasts, osteoclasts, and osteocytes.[13] The highly vascularized nature of bone and the presence of abundant osteoprogenitor cells within its structure allow it to repair injures and heal itself. When fractured, a blood clot forms at the damaged site, and various inflammatory mediators are released in the area to recruit cells involved in the repair process.[17] Depending on the stability and the location of the damage, the repair may proceed through either the formation of a temporary cartilage tissue or direct bone formation.[15] However, in cases of extensive bone loss,

the regenerative capacity becomes limited and exceeds the natural capacity of bone to heal spontaneously. These critical-size defects (CSDs) may require additional therapeutic intervention to achieve complete healing.[18, 19]

1.2. Bone Loss in the Alveolar Ridge

1.2.1. Anatomy and Clinical Significance

The oral cavity is a complex and dynamic environment where teeth and their supporting periodontal tissues work together to maintain functions like mastication and speech. These supporting tissues include the alveolar bone (or ridge), periodontal ligaments (PDLs), cementum, and gingiva.[20, 21]

The alveolar bone consists of the alveolar process, which forms the body of the ridge, and the alveolar bone proper (also known as bundle bone), which houses the tooth sockets.[22] The alveolar process forms the body of the ridge and is made up of cortical bone surrounding a cancellous core filled with bone marrow.[16, 22] In contrast, the alveolar bone proper is a perforated cortical bone plate that lines the tooth socket and provides vascular and neural supply, as well as access for MSCs, which are essential for bone remodeling and regeneration.[15] The alveolar bone develops in conjunction with tooth eruption and continuously remodels in response to mechanical stimuli. Teeth are connected to bone through the PDLs, and together they form the tooth attachment apparatus, which adapts dynamically to functional demands. However, when teeth are lost, these structures are no longer mechanically stimulated, and the alveolar bone begins to resorb and undergo morphological changes.[16, 22, 23]

1.2.2. Consequences of Tooth Loss

Bone loss in the alveolar ridge can result from trauma or diseases like periodontitis or periapical lesions. These conditions can compromise the supporting bone structure, ultimately leading to

tooth loss.[24, 25] Following tooth loss, the alveolar ridge undergoes progressive resorption and atrophy due to the absence of mechanical stimulation from teeth and periodontal ligaments. This remodeling process reduces both the height and width of the ridge, complicating future restorative procedures and affecting oral function and aesthetics.[26-28]

Alveolar ridge atrophy is a well-documented and predictable phenomenon.[26, 29] One explanation for these patterns is the bundle bone theory, which proposes that the bundle bone relies on the presence of teeth and PDLs for its maintenance.[30] Following tooth extraction, bundle bone loses its functional role and is resorbed by the body as part of a normal physiological process. As the buccal bone plate is naturally thin and primarily composed of bundle bone, it becomes especially susceptible to rapid and significant resorption following tooth extraction.[23, 31] Animal studies have shown that initial dimensional changes become evident within 2 to 3 months after extraction, with resorption more pronounced on the buccal aspect.[30, 32] In humans, clinical studies have reported that the most significant dimensional changes occur within the first year after extraction, with horizontal bone loss ranging from 30% to 60% and vertical bone loss around 10% to 20%.[27] The severity and pattern of resorption can also vary depending on anatomical location. In the mandible, posterior edentulous areas resorb at a rate four times greater than anterior regions. In the maxilla, the horizontal width reduction is more pronounced than the vertical height loss, especially in the posterior regions. All of these changes can result in defects of varying sizes, shapes, and severities, which pose challenges in restoring lost bone tissues.[33-35]

1.3. Clinical Challenges and Current Regenerative Strategies

Restoring the lost alveolar bone presents several clinical challenges that impact the success and predictability of restorative rehabilitation. Inadequate bone volume can prevent dental implant placement and limit other restorative options.[36, 37] Moreover, progressive bone resorption can bring the residual alveolar ridge into closer proximity with critical anatomical structures such as

the maxillary sinus or the inferior alveolar canal. This can increase the risk of surgical rehabilitation procedures.[35, 37]

Bone regeneration is generally confined to the anatomical boundaries of the alveolar ridge and does not extend beyond the dimensions of the original defect without intervention.[38] Therefore, augmentation procedures aim to restore bone volume and increase the density and dimension of existing bone. However, the success of these procedures depends greatly on the shape and size of the defect, as well as the availability of bony walls that provide mechanical support and vascular supply. [39, 40]

Common alveolar bone augmentation techniques include autogenous bone block grafting and guided bone regeneration (GBR).[40, 41] The block graft procedure utilizes autogenous bone harvested from intraoral or extraoral sites. These types of grafts are inherently osteogenic and integrates rapidly as they contain viable cells and growth factors essential for bone regeneration.[42] A major drawback of this grafting method is the associated donor site morbidity. It entails invasive surgical procedures for harvesting bone blocks, which carry potential risk and increase patient discomfort.[42] GBR is a widely utilized surgical technique for augmenting bone in deficient sites. The technique utilizes a barrier membrane to isolate the surgical site from the surrounding soft tissue.[6, 43] This creates a secluded environment that allows osteogenic cells to repopulate the defect and initiate new bone formation.[18] Both resorbable and non-resorbable membranes can be used in conjunction with bone grafting material.[44] The role of the bone grafting material is to maintain the space under the membrane to facilitate bone formation and replacement with native bone over time.[40, 45] GBR is considered safe and predictable, with clinical studies showing implant success rates ranging from 61.5% to 100% in GBR-treated sites.[36] Long-term follow-up studies have shown implant survival rates between 91.9% and 92.6% when implants are placed simultaneously with GBR.[46]

The GBR technique offers advantages over autografts by avoiding donor site morbidity and reducing surgical time and patient discomfort.[47] However, GBR is technique-sensitive, and

success depends on proper case selection, careful surgical management, stable membrane fixation, adequate vascularization, and tension-free soft tissue closure. Limitations include the risk of membrane exposure, soft tissue dehiscence, and the need for surgical reentry when non-resorbable membranes are used.[44, 48, 49]

1.3.1. Bone Grafts in Dentistry

In conjunction with surgical techniques, bone grafting material is widely used in alveolar bone regeneration. Bone is considered the second most transplanted tissue, with over two million procedures performed annually in the United States.[50] Ideal bone grafting material should combine biological and mechanical properties. Biologically, it must be biocompatible to avoid triggering an immune response or toxic reaction. It should also be osteoconductive, providing a scaffold for bone cell attachment and migration; osteoinductive, stimulating cells to differentiate into osteoblasts; and osteogenic, providing bone-forming cells.[24, 51] Mechanically, the material should provide adequate strength and stiffness to withstand functional load and should gradually degrade to allow natural bone to replace it over time.[52, 53] No single material meets these criteria, and clinicians must choose the most appropriate graft based on the specific clinical scenario.[24]

Autografts are considered the gold standard in bone grafting due to their osteogenic, osteoinductive, and osteoconductive properties. They are sourced directly from patients, eliminating the risk of immune rejection or disease transmission. Despite their effectiveness, autografts require an additional surgical procedure to collect bone, with a limited amount to harvest, and there is a risk of donor site morbidity.[25, 52] Allografts are bone grafts obtained from genetically non-identical individuals of the same species. They are extensively processed to reduce immunogenicity and eliminate the risk of disease transmission. Allografts are primarily osteoconductive, with limited osteoinductive potential depending on the preparation method. Although allografts eliminate the need for a second surgical site, they lack living cells and have limited osteogenic potential. Their tendency to resorb rapidly and lower mechanical strength

makes them more suitable for non-load-bearing applications or for use in combination with other graft materials.[52-54] Xenografts are graft materials sourced from a different species, most commonly bovine bone. They are processed to remove the organic components and leave behind a mineral matrix. That acts as an osteoconductive scaffold for bone formation. A major limitation is their slow resorption rate, with up to 31% of the material potentially remaining at the grafting site.[52, 54]

Synthetic materials were developed to address some of the limitations associated with biological grafts and can be engineered to mimic the natural structure of bone. They are manufactured under controlled conditions to fine-tune properties such as biocompatibility, bioactivity, degradation rate, and mechanical strength. However, they are mainly osteoconductive, with some materials exhibiting limited osteoinductive potential.[24, 25] Calcium phosphate (CaP) bioceramics are among the most widely used synthetic bone graft materials due to their similar chemical composition to natural bone minerals. They are naturally biocompatible, bioactive, and osteoconductive, making them suitable for bone applications by supporting cell attachment, proliferation, and differentiation.[51, 55] Despite the advantages of synthetic CaP, these ceramics are brittle in nature with low mechanical strength, which limits their application to non-load-bearing sites. Also, their resorption rate can be unpredictable and may compromise volume stability in large defects.[24]

The most commonly used forms of CaP include HAp, tricalcium phosphate (TCP), and a combination of both known as biphasic calcium phosphate (BCP).[52, 56, 57] HAp [$Ca_{10}(PO_4)_6(OH)_2$] is the main inorganic component of bone and teeth, contributing to their structural rigidity and mechanical strength. It is widely used in biomedical applications for its excellent biocompatibility and osteoconductivity.[58] However, synthetic HAp is highly crystalline and lacks trace minerals found in natural bone, making it chemically stable and slow to degrade in vivo.[59] It may remain at the graft site for years, which limits its use as a filler material. TCP exists in two forms: alpha-tricalcium phosphate (α-TCP) and beta-tricalcium phosphate (β-TCP). The beta form of TCP is

stable at physiological temperature, which makes it suitable for use in bone applications. Compared to HAp, β-TCP has a low CaP ratio, which contributes to its faster degradation and resorption in vivo.[25] The material has a porous interconnected structure that can facilitate cell infiltration and support vascularization. BCP was developed by combining HAp and β-TCP to balance structural stability and material resorbability. The inclusion of β-TCP enables gradual resorption, while the presence of HAp slows degradation, allowing the material to support bone regeneration while being replaced by natural tissue.[56, 60] The ratio between the two phases can be adjusted to tailor the resorption profile for specific clinical needs.[61] BCP is available in various formats, such as particles or a moldable putty that can be used in dental and orthopedic applications.

1.4. Tissue Engineering as an Alternative Approach

Despite advances in surgical techniques and bone grafting materials for traditional regenerative methods, they often fall short in CSDs or in replicating the complex structural and biological environment required for bone regeneration. Therefore, new research is increasingly shifting from conventional bone graft strategies towards stem cell-based therapy and tissue engineering as a comprehensive alternative solution for regenerating lost tissue in the oral cavity.[62, 63] In the field of tissue bioengineering, the strategy combines the principles of biology, engineering, and material science to create a functional biological replacement for damaged tissues by integrating multiple key components, including biomaterials, cells, and bioactive molecules.[21, 48, 64] Biomaterials serve as a scaffold with a three-dimensional matrix designed to mimic the native ECM and support stem cell attachment, proliferation, and differentiation. Commonly used materials include natural polymers such as silk and collagen, as well as synthetic polymers and bioceramics, all of which can be tailored to meet the biomechanical and biological requirements of specific anatomical sites.[21] Stem cells act as a natural repair system in the body and have the

potential to differentiate into various cell types. Their interaction with the scaffold material and the local microenvironment initiates a cascade of cellular and molecular events that guide tissue regeneration.[10, 65] MSCs are among the most widely used in bone applications due to their osteogenic potential and ease of isolation from a wide range of tissues, such as bone marrow and adipose tissues.[15, 66] In addition, a variety of bioactive molecules, like growth factors and morphogens, can be incorporated to enhance the regenerative process and accelerate healing.[67]

1.4.1. Scaffold Design and Ideal Requirements

The biocompatibility of materials used to fabricate scaffolds is a fundamental design requirement. The chemical composition of materials can directly influence cellular response and determine the type of cells that infiltrate the scaffold. Materials should be cytocompatible, non-toxic, elicit minimal or no immune response, and their degradation products must not cause adverse effects locally or systemically.[68, 69]

Matching the mechanical properties of the scaffolds to the native bone is important for providing temporary support to bear the initial physiological loads and resist deformation while providing a stable network for cell infiltration and tissue ingrowth. An ideal scaffold should also degrade gradually at a rate synchronized with the newly formed tissue. Maintaining that balance between mechanical strength and degradation rate is important to prevent early mechanical failure and sustained support during the regeneration process.[69]

In addition, the scaffolds should exhibit an interconnected macroporous structure to support cell infiltration, nutrient flow, and the removal of waste products. Macropore size and configuration have been shown to influence cellular behavior.[70] Studies reported that the ideal pore size for a bone scaffold that promotes osteogenesis and vascularization ranges between 300 and 800 μm.[71] A smaller pore size below 100 μm has been shown to prevent cell infiltration and limit MSCs differentiation.[72] In addition, topographic features like micropores and surface

roughness were found to play a role in guiding cell behavior and promoting osteoblast adhesion and migration by modulating protein adsorption and surface energy.[71, 73]

1.4.2. Scaffold Fabrication with Additive Manufacturing

Additive manufacturing (AM), or 3D printing, is a powerful and promising tool in bone tissue engineering.[74, 75] It allows for precise layer-by-layer fabrication of scaffolds with controlled geometry, porosity, and spatial material distribution.[76] These features are difficult to achieve with conventional methods such as particle leaching or freeze drying.[77] One major advantage of AM lies in its ability to produce customizable scaffolds that match the specific anatomical needs of individual patients.[9] The process starts by obtaining patient-specific data from CT or MRI scans. Those images are stored as Digital Imaging and Communications in Medicine (DICOM) files, which can be segmented and reconstructed into 3D models using computer-aided design (CAD) software. Based on these data, scaffolds can be designed in the CAD software to match the dimensions and the geometry of alveolar bone defects. Afterward, the designed scaffold is exported as standard tessellation language (STL) files, which are then processed into geometric code (G-code) by slicing software. This G-code serves as a set of instructions that guides the AM process.[9]

Direct ink writing (DIW) is an extrusion-based AM technique in which a viscous or paste-like material is extruded through a nozzle under controlled pressure to form a continuous filament. This filament is deposited layer by layer to build a 3D structure that can maintain its shape without collapsing or spreading.[78, 79] A wide range of biomaterials, like polymers, ceramics, and composite formulations, can be processed and engineered for DIW.[80] The selected biomaterial must exhibit shear-thinning behavior, where viscosity decreases under shear strain to allow for smooth extrusion, and viscoelastic behavior to maintain shape fidelity and structural stability during and after extrusion.[79, 81]

1.4.3. Silk as a Biomaterial for Scaffold 3D Printing

Silk fibroin (SF) extracted from Bombyx mori (B. Mori) silkworm cocoons has been explored as a biomaterial in 3D printing scaffolds for bone tissue engineering due to its favorable rheological properties.[82, 83] The material exhibits shear-thinning and viscoelastic behavior, which makes it suitable for extrusion-based 3D printing.[84] In addition, SF is favored for its mechanical strength, biocompatibility, minimal immunogenicity, and tunable biodegradability, with no toxic byproducts.[85-87]

These properties stem from the unique hierarchical structure of silk. The B. mori silk fibers are composed of two main proteins: a structural fibroin core encased by sericin coating. For most tissue engineering applications, the outer sericin layer is removed by boiling the raw silk fibers in an alkali solution, leaving behind the SF. This fibroin core is composed of repetitive amino acid sequences that self-assemble in β-sheet crystalline domains interspaced with amorphous regions. After boiling, the β-sheet structure of SF is dissolved in an ionic solution, producing an aqueous SF solution that can be utilized in a wide range of biomedical applications. Furthermore, the self-assembly property of the β-sheet crystallites eliminates the need for additional chemical or photochemical crosslinking, which simplifies the fabrication process of biomedical devices. This structure provides the material with high tensile strength, toughness, and elasticity, making it particularly suitable for bone applications.[85-87]

SF has been extensively explored in fabricating scaffolds for bone regeneration. However, in its pure form, silk has limited osteoconductive and osteoinductive properties. Thus, the material is often combined with bioceramics, such as HAp, to create composites with an enhanced polymeric matrix and a chemical composition similar to that of bone.[88, 89] This hybrid approach aims to improve properties such as mechanical strength, degradability, and bioactivity, and tailor it to meet the specific requirements for bone applications.[90]

SF-HAp composites can be formulated into injectable, paste-like bone cements suitable for printing with DIW. Silk acts as a cohesive matrix that binds the HAp particles, creating an ink

that can be extruded to form filaments.[91-93] These filaments can be stacked to form a 3D scaffold with defined architecture and controlled macro- and microporosity to support bone tissue growth.[91] This type of construct has been tested with various cell types. In vitro studies have shown that MSCs adhered successfully to the scaffolds and exhibited increased metabolic activity, proliferation, and osteogenic differentiation. It also showed compatibility with vascular and neural cell types under growth factor delivery conditions. Human umbilical vein endothelial cells (HUVECs) showed strong attachment, metabolic activity, and chemotactic migration in response to scaffold functionalization with vascular endothelial growth factor (VEGF). Human-induced neural stem cells (hiNSCs) also adhered to the scaffold, extended neurites, and responded to nerve growth factor (NGF) loaded into the scaffolds.[82]

1.4.4. Functionalization with Bioactive Molecules

The regenerative capacity of silk-based scaffolds can be further enhanced by functionalization with bioactive molecules. The incorporation of growth factors and morphogens helps to direct cellular behavior and accelerate regeneration within the scaffold. This approach stems from an evolving understanding of bone biology and how signaling molecules guide cellular activity at the injury site. These signals recruit progenitor and inflammatory cells to initiate and support repair.[94] As a result, scaffold design has shifted from passive structural support to functionalized systems that actively modulate the healing environment by regulating cell proliferation, migration, differentiation, and matrix production. This creates an instructive environment that supports osteogenesis and vascularization in large bone defects and accelerates healing.[95, 96]

The therapeutic efficacy of growth factors is highly dependent on how they are delivered. Uncontrolled or rapid release often leads to diminished regenerative outcome and potential side effects.[67, 95] One common approach is to soak scaffolds in a growth factor solution. However, the initial burst release and rapid attenuation remain a limitation of this method. Physical

encapsulation of growth factors within biodegradable polymer for sustained release is another method, but it still has similar issues to the soaking method, with poor long-term control over release kinetics.[9] Covalent immobilization allows for more stable and localized delivery by chemically binding growth factors to scaffold surfaces.[96] Other strategies mimic the ECM through molecules like heparin, which can reversibly bind growth factors and maintain their stability and retention for controlled release over time.[97]

Factors such as bone morphogenetic proteins (BMPs) and platelet-derived growth factor (PDGF) are widely used in craniofacial applications.[98, 99] Recombinant protein technology has enabled the large-scale production of biologically active forms of these molecules that can be used in regenerative applications, shifting the direction towards a biomimetic approach.[100]

a. Bone Morphogenetic Protein-2

BMPs are part of the transforming growth factor-beta (TGF-β) superfamily that can promote bone formation by directing MSCs toward osteogenic differentiation.[101] In particular, BMP-2 has shown great potential for promoting bone regeneration in craniofacial applications and upregulates the expression of bone-specific markers such as alkaline phosphatase (ALP) and osteocalcin (OCN).[101] The mechanism of action of BMP-2 begins by binding to type I and type II serine/threonine kinase receptors on the cell surface. This activation leads to the phosphorylation of intracellular transduction proteins SMAD1/5/8. These activated SMADs form a complex with SMAD4 and translocate into the nucleus to activate target genes that promote the differentiation of MSCs into osteoblasts or chondroblasts.[94, 100]

Clinical research has established recombinant BMP-2 (rhBMP-2) as an effective growth factor for promoting bone regeneration in the craniofacial region. Currently, it is delivered in absorbable sponge and has shown effective bone regeneration in procedures like alveolar ridge augmentation and spinal fusion.[102] Some clinical reports found comparable outcomes to

traditional methods with the added advantage of avoiding donor site morbidity.[103] The use of rhBMP-2 continues to be explored in combination with other materials to further broaden its clinical utility in bone regeneration.[104, 105]

b. Platelet-Derived Growth Factor

PDGF is a regulatory growth factor involved in wound healing, bone repair, and regeneration. It primarily functions as a mediator for cell migration, proliferation, and survival of mesenchymal progenitor cells, including those with osteogenic potential. It also plays a role in angiogenesis and helps with vascular network formation at sites of bone and tissue repair. This dual function makes it a valuable bioactive molecule for tissue engineering applications.[94, 98] PDGF exists in four isoforms: PDGF-A, -B, -C, and -D. These isoforms can pair up to form five biologically active dimeric forms, including PDGF-AA, -AB, -BB, -CC, and -DD. Each form acts on two PDGF receptors, alpha and beta, found on the cell surface. Those receptors are also dimeric and can form homo- ($\alpha\alpha$, $\beta\beta$) or heterodimers ($\alpha\beta$). PDGF-BB is the most potent isoform that can activate all three PDGF receptors and trigger chemotaxis and mitogenesis of cells of mesenchymal origin, like osteoblasts and chondroblasts.[94, 98]

Recombinant PDGF (rhPDGF) has been extensively studied for bone regeneration in the oral cavity. Several carrier systems have been tested for delivering rhPDGF, including autografts, xenografts, and synthetic materials such as β-TCP.[106] Alveolar bone regeneration using rhPDGF has shown bone formation results comparable to autografts, eliminating the need for harvesting bone from another site. In ridge preservation, histological analysis studies showed that rhPDGF can enhance the formation of new vital bone in extraction sockets. Studies also showed that PDGF, when used alone or with graft materials, is safe and well-tolerated, posing no serious risks to patients.[106, 107]

1.5. Gap in Knowledge

Despite advancements in bone grafting techniques and materials, achieving predictable outcomes in alveolar ridge augmentation remains a clinical challenge, particularly in CSDs. Current regenerative options include biological types of grafts and synthetic bioceramics substitutes. While both types offer distinct advantages, their performance varies significantly depending on factors like composition, manufacturing methods, and clinical handling characteristics. Key features, such as crystallinity, porosity, and surface topography, directly impact how the graft integrates with native bone tissues, maintains volume, and degrades in a synchronized manner with bone formation. These characteristics are not standardized across commercially available products, contributing to unpredictable clinical outcomes. Additionally, most available grafts are not designed to match the specific anatomical geometry of the mechanical demands of the alveolar ridge.

Growth factor-based grafts have emerged as a novel class of grafting materials that integrate tissue engineering principles by utilizing osteoconductive matrices loaded with morphogens and growth factors, such as BMP-2 and PDGF. These types of materials have shown promising outcomes in small alveolar ridge defects. However, current carrier options often lack the spatial and temporal control necessary for growth factor delivery, resulting in an initial burst release followed by rapid attenuation. Additionally, many of these applications are being used off-label, with no standardization in dosing and release kinetics. This can result in low therapeutic effects and increase the risk of side effects, such as ectopic bone formation or inflammation.[108] There is a need for clinically viable delivery systems that can preserve growth factor bioactivity and enable controlled, localized delivery to simulate the healing biology at the site of the defect.

Additionally, while 3D printing has emerged as a powerful tool in bone tissue engineering, its application in alveolar ridge augmentation is still limited. Most scaffold materials described in the literature are generalized for bone regeneration and do not address the specific anatomical,

structural, or mechanical requirements of the alveolar bone. However, advancements in biomaterial science and AM have enabled the fabrication of scaffolds with tunable micro- and macroporosity, mechanical strength, and bioactivity necessary for a successful outcome. Composite materials that combine CaP and bioactive glass (BG) ceramics with synthetic or natural polymers, such as SF, are currently being explored. These innovations can offer a customizable approach for patient-specific and biologically active constructs tailored for alveolar bone regeneration.

Another promising strategy in bone tissue engineering is the co-culturing of hMSCs with HUVECs to promote osteogenesis and vascularization through paracrine signaling and cell-to-cell signaling. While co-culture systems have shown positive effects in various scaffold systems, they have not been evaluated in 3D printed scaffolds composed of SF and BG. What makes BG an attractive material for scaffold fabrication is its ability to interact with body fluids and release ions at the implantation site, stimulating bone formation and supporting angiogenesis. Given the unique combination of bioactivity, printability, and mechanical properties of this type of composite, its potential to support the co-culture of hMSCs and HUVECs and promote early bone formation remains to be investigated.

Together, these limitations point to the need for a tissue engineering strategy that combines customizable osteoconductive scaffolds with controlled growth factor delivery and a biologically supportive environment. Such a system should support new bone formation while also fulfilling the mechanical and handling requirements necessary for clinical use. Additionally, the selected materials must be optimized not only for biological performance but also for compatibility with manufacturing methods. Bridging these gaps can improve clinical outcomes and expand the therapeutic options for managing complex alveolar bone defects.

1.6. Objectives and Thesis Organization

The objective of this thesis is to explore bioengineered strategies for the regeneration of critical-size alveolar bone defects using silk-based 3D printed composite scaffolds. Specifically, the research aims to develop and evaluate silk-based biomaterials that integrate bioactive components and AM fabrication methods to create scaffolds capable of supporting osteogenesis in vitro. By combining SF with various types of bioceramics, this work investigates how composite formulation, scaffold design, and biological functionalization influence the bone regenerative potential of the engineered constructs. The study scope includes material development, printability, and mechanical assessment, as well as in vitro biological evaluation using hMSCs, with or without endothelial cells, to simulate the healing process of bone.

Thesis Organization:

- **Chapter 1:** I introduced the clinical challenges associated with alveolar bone loss and discussed the biological basis of bone regeneration. I also reviewed current generative techniques and the limitations of conventional methods. This chapter establishes the rationale for using bioengineered scaffolds and outlines strategies explored in this thesis.
- **Chapter 2:** In this chapter, I present a bioengineered approach to alveolar bone regeneration using 3D printed SF-BCP composite scaffolds functionalized with BMP-2 and PDGF. A heparinized hyaluronic acid-based hydrogel was incorporated within the scaffold system to enable the controlled delivery of growth factors. This study focuses on scaffold fabrication, the release kinetics of growth factors, and the in vitro evaluation of osteogenic differentiation and extracellular matrix formation when seeded with hMSCs.
- **Chapter 3:** Here, in this chapter, I focus on developing a 3D printable composite made of SF and bioactive glass. The study evaluates the printability, mechanical properties, and biological performance of the scaffolds in a co-culture system using hMSCs and HUVECs.

The primary aim is to assess osteogenic differentiation and explore how scaffold-supported cell-to-cell interactions contribute to early bone formation.

Chapter 2: Growth Factor Functionalized Silk-Based 3D-Printed Scaffolds: A Bioengineered Approach for Alveolar Bone Regeneration.

2.1. Abstract

This in vitro study explores a tissue engineering strategy aimed to develop a potential solution for the regeneration of critical-size bone defects in the alveolar ridge. We developed a bone cement material by combining silk fibroin solution with biphasic ceramic comprised of hydroxyapatite and tricalcium phosphate. Fine-tuning the liquid-to-powder ratio of the bone cement material yielded an optimized ink suitable for 3D printing bone scaffolds. The scaffolds exhibited good mechanical properties, controlled macroporosity (>400 μm), and an interconnected internal network supportive to cell infiltration and conducive to osseointegration. To enhance the osteogenic potential, scaffolds were further supplemented with a hyaluronic acid (HA)-gelatin hydrogel for the controlled delivery BMP-2 and PDGF. In vitro assessments with hMSCs cultured on the scaffolds demonstrated the cytocompatibility of the material. Scanning electron microscopy (SEM) showed evidence of cell infiltration, proliferation, new matrix deposition within the scaffold pores, and mineralization observed after 35 days of cell culture. The scaffolds were osteoinductive, with BMP-2-functionalized scaffolds showing significantly higher alkaline phosphatase (ALP) activity. Additionally, we monitored the release kinetics of BMP-2 and PDGF over time through enzyme-linked immunosorbent assay (ELISA). Both factors maintained their bioactivity and were released by the HA hydrogel in a sustained manner, demonstrating the potential of these scaffolds as a delivery vehicle for growth factor release. While these findings are promising, future studies are recommended to evaluate the efficacy of this tissue engineering approach in bone regeneration using animal models.

2.2. Introduction

Restoring insufficient bone volumes after tooth loss remains a major challenge in regenerative dentistry.[36] While traditional grafting techniques aimed to restore alveolar ridge morphology, advances in recombinant protein technology and biomaterials have enabled the development of bioengineered strategies that leverage the delivery of growth factors and morphogens to stimulate the inherent regenerative capacity of the body for healing.[100, 109] Tissue bioengineering offers a promising solution by integrating stem cells, growth factors, and biomaterials to create scaffolds that promote cell adhesion, proliferation, and differentiation.[9] New graft materials that utilize tissue engineering principles have emerged for alveolar bone regeneration, combining natural or synthetic osteoinductive matrices loaded with factors such as BMP-2 or PDGF to enhance the quality and predictability of bone regeneration.[63, 110, 111] However, the success of such an approach depends not only on the biological potency of the factors themselves, but also on the ability to control their release profile in the local environment.[96] Without appropriate delivery systems, factors can undergo burst release, rapid clearance, or enzymatic degradation, which ultimately can compromise the therapeutic outcome and increase the risk of adverse effects.[9, 67]

Hyaluronic acid (HA)-based hydrogels are frequently utilized for the delivery of growth factors and morphogens in bone tissue regeneration. HA is a naturally occurring glycosaminoglycan involved in wound healing, cell signaling, and angiogenesis. Its high biocompatibility, mild gelation conditions, and ability to form a hydrated matrix make it well suited for delivering growth factors in bone applications.[112-114] HA can be chemically modified to adjust its degradation rate and release kinetics of encapsulated molecules. HA modification with integrin-specific fibronectin fragments improved cell attachments and bone formation when delivering BMP-2. In one study, acrylated HA hydrogel loaded with BMP-2 and human mesenchymal stem cells (hMSCs) was effective in bone formation and vascularization in rat calvarial defects.[115, 116] Additionally, heparin has been explored as a carrier for factors in HA-based hydrogels.[117] The use

of immobilized heparin in HA hydrogels can mimic the heparin sulfate proteoglycans normally found in the ECM attached to the hyaluronan backbone. Heparin forms ionic bonds with proteins and protects them from proteolysis and slows their release in a controlled and sustained manner.[118] For example, photo-crosslinked HA-heparin matrices enabled sustained release of BMP-2 over four weeks and significantly enhanced bone formation in vivo.[119] It was also used for the delivery of PDGF-BB and other growth factors in combination with stem cells, and resulted in improved vascularization and tissue regeneration.[120, 121]

Thus, the aim of this in vitro study was to develop a bioengineered system that integrates 3D printed composite scaffolds with hydrogel-based delivery of BMP-2 and PDGF, as a potential strategy for addressing CSDs in the alveolar ridge. A printable bone cement material composed of SF and BCP was developed and used to fabricate scaffolds using extrusion-based 3D printing. To enable the controlled delivery of growth factors and morphogens, the scaffolds were supplemented with a heparinized hyaluronic acid/gelatin-based hydrogel loaded with BMP-2 and PDGF. This approach was designed to maintain an optimal local concentration of these bioactive molecules and enhance the regenerative potential of the scaffolds. We hypothesized that the combined system would stimulate and support new bone formation in vitro when used with hMSCs.

2.3. Materials and Methods

2.3.1. Silk Preparation. The SF extraction was done by following a previously published protocol.[122] The process began with cutting Bombyx mori silk cocoons and then boiling the cut pieces for 60 minutes in a 0.02 M aqueous Na_2CO_3 solution to remove the sericin outer layer that envelopes the fibroin fibers in silk. Subsequently, the boiled silk was thoroughly rinsed with deionized water (diH_2O) for three cycles and left to dry overnight. The dried SF was then dissolved in a 9.3 M aqueous lithium bromide (LiBr) solution at 60 °C for 3 hours. Afterward, the solution

underwent dialysis against diH_2O with six water changes within 48 hours. The resulting solution was centrifuged at 9000 rpm at 4 °C twice for 20 minutes to remove impurities. The unconcentrated solution was further concentrated in a dialysis tube submerged in a 15% (w/v) aqueous solution of polyethylene glycol (PEG, Mn 20,000, Sigma-Aldrich) for approximately 40 hours, resulting in a final concentration of 25-30%.

2.3.2. Bone Cement: Ink Preparation and 3D Printing. Bone cement was prepared by combining a BCP comprised of equal parts of β-TCP and HAp, with diH_2O and the concentrated SF. The final liquid-to-powder ratio was optimized at 1.3:1 (v/w). The BCP was initially dissolved in the diH_2O, which was achieved by using two connected syringes for mixing. The SF solution was then introduced, which created a paste-like material suitable for filament extrusion in 3D printing. This paste was loaded into a custom-made extrusion 3D printer and then extruded through a 23 Ga 1/2-inch blunt needle (McMaster Carr) to print cylindrical scaffolds. Stepper motors controlled the movements of the 3D printer in the x and y directions and the printhead movement in the z direction. These were operated through an Arduino board running Marlin firmware. The Repetier software managed the printing process. The scaffolds were printed with a controlled macroporosity of 30% infill, measuring 11 mm in diameter and 2.5 mm in height. After printing, the constructs were dried overnight in a 37 °C humid environment and subsequently sterilized using an autoclave.

2.3.3. Mechanical Testing. A uniaxial compression test was performed on cylindrical specimens of the bone cement material using an Instron 3366 machine, following the testing protocol outlined in ASTM method F451 standard specification for acrylic bone cement (**Figure 2-1**). Samples were prepared by injecting the material into metal cylindrical molds measuring 6 mm in diameter and 12 mm in height. These were allowed to dry overnight in a humid environment at 37 °C. Subsequently, the prepared samples were stored at room temperature for seven days. Dry and

wet conditions were tested for different ratios of β-TCP and HAp, with a sample size of n = 5 for each condition (**Table 2-1**). Before the compression test, samples in the "wet" condition were soaked in phosphate-buffered saline (PBS) for 24 hours. The compression test was conducted at a loading rate of 20 mm/min using a 1 kN load cell.

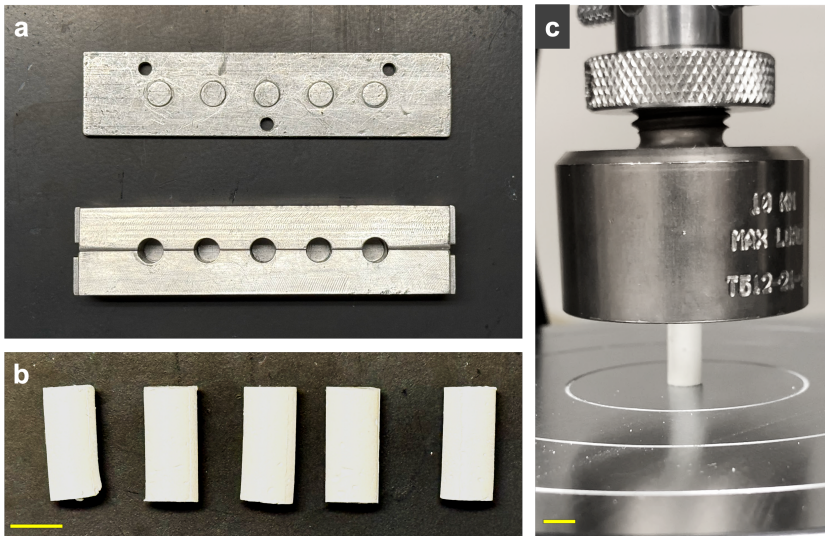

Figure 2-1. Set up for compressive mechanical testing of cylindrical samples using an Instron 3366 universal testing machine. **(a)** Custom stainless steel mold components used for fabricating cylindrical specimens for material bulk testing **(b)** Representative dried cylindrical scaffold samples after demolding. **(c)** A sample positioned for uniaxial compression testing under a 1 kN load cell. Scale bar = 6 mm.

Table 2-1. Bone cement compositions used for mechanical testing.

Formula	~27% SF [mL]	Di Water [mL]	β-TCP [g]	HAp [g]
100% β-TCP	0.3	1.0	1.0	-
90% β-TCP / 10% HAp	0.3	1.0	0.9	0.1
80% β-TCP / 20% HAp	0.3	1.0	0.8	0.2
50% β-TCP / 50% HAp	0.3	1.0	0.5	0.5
20% β-TCP / 80% HAp	0.3	1.0	0.2	0.8
100% HAp	0.3	1.0	-	1.0

2.3.4. Rheological measurements. To simulate the conditions experienced during 3D printing, the rheological properties of the bone cement ink were assessed using a rheometer (TA Instrument, USA) equipped with a parallel plate geometry of 20 mm diameter, with the geometrical gap sat at 500 μm. Testing conditions included SF alone and the bone cement material with and without the inclusion of SF while maintaining the v/w ratio (**Table 2-2**). The flow behavior was evaluated by measuring viscosity as a function of the shear rate, with the shear rate incrementally increasing from 0.1 to 1000 s^{-1}. An amplitude sweep test was conducted at a fixed oscillation frequency of 1 Hz, alongside a frequency sweep test at 1% shear strain. These tests were used to characterize the viscoelastic properties of the material by evaluating the storage modulus (G′) and the loss modulus (G″). Additionally, the temporal structural stability of the material was assessed by monitoring changes in the moduli over time while maintaining a constant 1% strain and 1 Hz oscillation frequency.

Table 2-2. Compositions of inks used for rheometric analysis.

Formula	~27% SF [mL]	Di Water [mL]	β-TCP [g]	HAp [g]
BCP	-	1.3	0.5	0.5
SF-BCP	0.3 mL	1.0	0.5	0.5

2.3.5. Printability. The accuracy of the printed pores was assessed by calculating the printability index and spreading ratio to evaluate how closely the printed pores matched the intended design. Samples were printed using a 23 Ga, 1/2-inch blunt needle (McMaster Carr) with a grid infill set at 30%. Images of the printed samples were captured and analyzed using ImageJ software. The printability index was calculated using the equation $P = L^2 / 16A$, where L represents the pore's perimeter, and A represents the pore area. The spreading ratio was determined as the ratio between the diameter of the extruded filament and the nozzle diameter. A printability index and

spreading ratio of 1 is indicative of high precision, while values greater or lesser than 1 reflect less accurate prints.

2.3.6. Supplementation with hydrogel. The scaffolds were supplemented with an HA and gelatin-based hydrogel (HyStem®-HP Sigma-Aldrich) to provide a hydrated osteoconductive environment and also enable controlled growth factor release. This hydrogel system consists of thiol-modified hyaluronan with conjugated heparin (HyStem®-HP), thiol-modified gelatin (Gelin™-S), and polyethylene glycol diacrylate crosslinker (Extralink®). These components are combined to create a customizable 3D environment for various cell types. The HA/gelatin hydrogel was prepared according to the manufacturer's instructions. Each vial of HyStem®-HP and Gelin™-S was reconstituted with 1 mL degassed water to create a 1x stock solution and then placed on a shaker for 30 minutes to ensure complete dissolution. Subsequently, both stock solutions were carefully mixed by pipetting back and forth to avoid air bubble formation. Finally, 0.5 mL of degassed water was added to the Extralink® vial and was carefully inverted several times to dissolve the contents. For the growth factor functionalized groups, rhBMP-2 (355-BM-050, R&D Systems) and rhPDGF-BB (PHG0046, Thermos Fisher) were reconstituted with 4 mM HCl and 100 mM acetic acid containing 0.1% bovine serum albumin (BSA), respectively. The reconstituted growth factors were added to the 1:1 HyStem®-HP/Gelin™-S mixture prior to crosslinking. To form the hydrogel, Extralink® stock solution was added to the mixture using a pipette, with a final ratio of 1:2:2 (Extralink®:HyStem®-HP:Gelin™-S). Finally, the hydrogel was injected into the scaffolds and allowed to crosslink in a 37°C incubator for 20 minutes. The final concentration of growth factors in the functionalized scaffold groups was 1 µg of BMP-2, PDGF, or their combination (1 µg of each).

2.3.7. Assessment of growth factor release. The release kinetics of the growth factors were evaluated using enzyme-linked immunosorbent assay (ELISA). Testing conditions included: (1)

scaffolds with growth factors added to the ink before printing, (2) scaffolds soaked in growth factor solutions post-printing, (3) scaffolds injected with the HA-based hydrogel loaded with growth factors, (4) unloaded scaffolds (control), and (5) scaffolds injected with unloaded hydrogel (hydrogel control). Each test scaffold received 1 µg of BMP-2, PDGF, or their combination. ELISA was performed at predefined time points to quantify and compare the release profiles of the growth factors from each functionalization strategy. To assess release over time, the constructs were immersed in PBS and incubated at 37 °C. Samples were collected at 1, 3, 6, and 12 hours and 1, 3, 5, and 7 days from three independent samples. At each time point, a 100 µl sample was taken and replaced with fresh PBS. Samples were analyzed using a commercially available sandwich ELISA kit based on human BMP-2 (Human BMP-2 DuoSet ELISA, DY355) and PDGF (PDGF-BB Human ELISA Kit, BMS2071). For BMP-2 ELISA, the Capture Antibody was first diluted to the working concentration and used to coat a 96-well microplate, which was then incubated overnight at room temperature. Following incubation, each well was washed three times with wash buffer to ensure the removal of unbound substances. After washing, 300 µL of reagent diluent was added to each well to block nonspecific binding, and the plate was incubated for one hour at room temperature. For the assay, 100 µL of either the sample or standard was added to each well and incubated for two hours at room temperature. The wells were washed again before adding 100 µL of the diluted detection antibody, followed by a two-hour incubation. Subsequently, 100 µL of streptavidin-HRP was added to each well and incubated for 20 minutes. This was followed by the addition of 100 µL of substrate solution per well, incubated for 20 minutes to develop color. The reaction was stopped by adding 50 µL of stop solution to each well, and the optical density was measured immediately using a spectrophotometer (Varioskan™ LUX multimode microplate reader, Thermo Fisher) set to 450 nm, with corrections made for wavelength imperfections. To determine the concentration of PDGF, samples were pre-diluted to 1:10 with assay buffer. A 96-well plate precoated with antibody to human PDGF-BB was washed first with wash buffer for 2 times. In each sample well, 50 µL of assay buffer was added, followed

by 50 µL of pre-diluted samples. Finally, 50 µL of diluted Biotin-Conjugate was added to all wells, and the plate was incubated for 2 hours at room temperature in an orbital shaker and then washed 6 times. Afterward, 100 µL of streptavidin-HRP conjugate was added and incubated for 20 minutes at room temperature. The wells were then treated with a TMB substrate solution, and the reaction was allowed to develop until a significant color change was noted for about 30 minutes. A stop solution was added, and the optical density of each well was measured using a spectrophotometer set at 450 nm. All samples were assayed in duplicate, and a standard curve was prepared for each growth factor.

2.3.8. In-vitro testing with stem cells. Prior to testing with stem cells, the scaffolds were soaked in a growth medium for at least 72 h before seeding. hMSCs at a passage of less than six were cultured in cell culture flasks. Once they reached over 80% confluence, cells were harvested and seeded onto the scaffolds in a 24-well plate using 1 mL of cell suspension. Cells were seeded at a density of 500×10^3 cells/mL in conditions involving scaffolds with or without hydrogel. For conditions involving tissue culture polystyrene (TCPS), a cell seeding density of 20×10^3 was used. The seeded scaffolds were allowed to set in a growth medium (GM) and placed in a humidified incubator (37°C, 5% CO2). The GM consisted of basal medium (DMEM high glucose GLUTAMAX, Gibco), supplemented with 10% Fetal Bovine Serum (Gibco), 1% antibiotic-antimycotic (Gibco), 1% Non-Essential Amino Acids (Gibco), and 5 ng/mL basic fibroblast growth factor (Gibco). After a 2-day incubation period, the medium was replaced with fresh GM or switched to osteogenic medium (OM) to induce hMSCs osteogenic differentiation in some of the testing conditions. The OM consisted of DMEM high glucose GLUTAMAX (Gibco), 10% Fetal Bovine Serum (Gibco), 1% antibiotic-antimycotic (Gibco), 100 nM dexamethasone (Sigma), 10 mM sodium β-glycerophosphate (Sigma), and 0.05 mM L-ascorbic acid. This medium replacement was performed every 2–3 days throughout the study period.

2.3.9. Metabolism. Cell metabolic activity was assessed with the cell viability reagent Alamar Blue on scaffolds and TCPS seeded with hMSCs during a 35-day incubation period. Metabolic activity was quantified on days 3, 7, 14, 21, 28, and 35. At each interval, media with 10% of Alamar Blue stain was added to samples in 24-well plates (1 mL per well) and incubated for 3 hours. Subsequently, samples were collected in replicates for immediate fluorescence measurement using a microplate reader with excitation at 560 nm and emission at 590 nm.

2.3.10. Cytotoxicity. A 3-(4,5-dimethylthiazol-2-yl)-2,5-diphenyltetrazolium bromide (MTT) assay was performed to evaluate the cytocompatibility of the bone cement material. hMSCs were seeded in a 96-well plate at a density of 5 x 10^3 in GM. Dissolution products were prepared by soaking the scaffolds (n = 3) in GM for 24, 48, and 72h, with media changes every 24h for the 48 and 72-hour time points. On the following day, the GM was replaced with dissolution product media, and the plate was incubated at 37 °C. As a positive control, GM containing 20% v/v dimethyl sulfoxide (DMSO) was added to control wells, while untreated media served as the negative control. After an additional 24h incubation, an MTT assay kit (Abcam) was used to conduct the experiment. By following the manufacturer's instructions, 50 µl of appropriate media was added to each well along with 50 µl of MTT reagent. After 3 hours of incubation at 37 °C, 150 µl of MTT solvent was added to each well. The plate was placed in an orbital shaker for 15 minutes, and the OD was read at 590 nm. Each condition had 3 samples, with each sample measured in triplicate. Based on the ISO 10993-5 standard for biological evaluation of medical devices, the material is considered cytotoxic if the cell viability is below 70% relative to the control.

2.3.11. Osteogenic differentiation. ALP activity and staining served as a marker for bone formation and osteoblastic differentiation in this study. ALP staining for samples in GM and OM after 21 days of incubation was done using a 5-bromo-4-chloro-3-indolyl phosphate/nitro blue tetrazolium (BCIP/NBT) tablet following the manufacturer's instructions (SIGMAFAST™

BCIP®/NBT, Sigma). This system reacts with the ALP enzyme and produces a stable black-purple precipitating substrate to detect ALP activity. An assay to quantify the ALP enzyme activity was conducted on day 21 for samples cultured in either GM or OM with or without functionalization with BMP-2 and PDGF. Initially, cells were lysed using 0.1% Triton X-100 in PBS, followed by sonication for 5 seconds at 20% intensity. Subsequently, ALP activity was assessed using a Colorimetric ALP Assay Kit (Abcam), with absorbance measured at 405 nm using a microplate reader. Furthermore, to account for variations in protein content, ALP activity was normalized to the protein content in the same lysed samples, determined using the Pierce BCA Protein Assay Kit (Thermo Scientific) by following the manufacturer's instructions, with absorbance measured at 562 nm.

2.3.12. Immunofluorescent Staining. The cell culture medium was removed, and scaffolds were washed with PBS. Afterward, cells were fixed with 4% paraformaldehyde for 20 min and then permeabilized with 0.1% triton X-100 in 1X PBS for 10 min, followed by three washes with PBS. Surfaces were blocked with 2% BSA for 1 hour at room temperature. COL-I (MA126771, Thermo Fisher) and Collagen X (COL-X, ab49945, Abcam) were stained using mouse monoclonal antibodies at a 1:150 dilution and incubated overnight at 4 °C. On the next day, the samples were washed 3 times with PBS, and then the secondary antibody goat anti-mouse 1/150 was incubated for 1 hour at room temperature. After additional washes, counterstaining was performed for F-actin (Phalloidin, A22287, Thermofisher) and nuclei (DAPI, Sigma).

2.3.13. Microscopy. Immunofluorescent images were obtained utilizing a confocal microscope Leica TCS FLIM SP8 (Wetzlar, Germany). Fluorescent quantification was performed using ImageJ software. Brightfield images were captured using a Keyence BZ-X700 microscope. Scanning electron microscopy (SEM) was performed to visualize the internal

structure of the scaffolds and the cellular growth inside the pores. Prior to imaging, the constructs were fixed in 4% paraformaldehyde solution for 20 minutes at room temperature. Following fixation, the constructs were dehydrated through a series of ethanol washes (25%, 50%, 75%, 80%, 90%, and 100%), followed by hexamethyldisilazane (HMDS, Sigma). Subsequently, the scaffolds were left to dry overnight. The dried samples were then gold-sputter-coated, and images were captured using a scanning electron microscope at various magnifications.

2.3.14. Statistics. Data were analyzed using SPSS version 25 (IBM Corp). An independent t-test was used for comparisons in conditions with two groups. For comparisons among multiple groups, One-Way ANOVA, Kruskal-Wallis, and Welch's tests were applied as appropriate with their respective post hoc comparison (Tukey's HSD for ANOVA, Dunn's test with the Bonferroni correction for Kruskal-Wallis, and Game-Howell for Welch's). A significance level of $p < 0.01$-0.05 was determined to be statistically significant. The level of significance in the graphs was represented by the number of asterisks, indicating the following levels: *P ≤ 0.05; **P ≤ 0.01; ***P ≤ 0.001; ****P ≤ 0.0001.

2.4. Results

2.4.1. Mechanical Properties. Uniaxial compression testing was performed to evaluate the mechanical properties of the SF-BCP bone cement material. This testing was conducted to assess the bulk material properties of the bone cement, which included SF combined with various BCP formulations. The tested formulations ranged from 100% β-TCP to 100% HAp, with intermediate ratios including 90% β-TCP / 10% HAp, 80% β-TCP / 20% HAp, 50% β-TCP / 50% HAp, and 20% β-TCP / 80% HAp. This analysis aimed to understand how different ratios of β-TCP to HAp influence the mechanical properties of the printed scaffolds. The compressive strength and modulus of various BCP ratios were evaluated under both dry and wet conditions (**Figure 2-2**). In dry conditions, the highest compressive strength was observed in the 20% β-TCP / 80% HAp (7.91 ± 0.87 MPa) and 50% β-TCP / 50% HAp (7.87 ± 1.28 MPa) groups, with no significant difference between them. In wet conditions, the highest compressive strength was found in the 100% HAp group (2.44 ± 0.10 MPa), which was significantly different from the other groups. For compressive modulus, the 50% β-TCP / 50% HAp (488.44 ± 104.34 MPa) and 80% β-TCP / 20% HAp (484.71 ± 94.95 MPa) ratios exhibited the highest values in dry conditions, with no significant difference between them. In wet conditions, the 50% β-TCP / 50% HAp ratio maintained the highest compressive modulus (244.27 ± 26.75 MPa), which was significantly higher than that of the other groups. The observed compressive strength and modulus values for the 50% β-TCP / 50% HAp ink fall within the reported range for trabecular bone in human mandible, making it suitable for dental applications. Based on its balanced and promising mechanical properties, this ink composition was selected for scaffold printing and further biological testing. A comparative bar graph (**Figure 2-3**) was created to relate the mechanical outcomes of this ink preparation to the known range of human mandibular bone properties (Compressive strength: 0.22–10.44 MPa; modulus: 24.9–240.9 MPa), as reported by Misch et al. (1999).

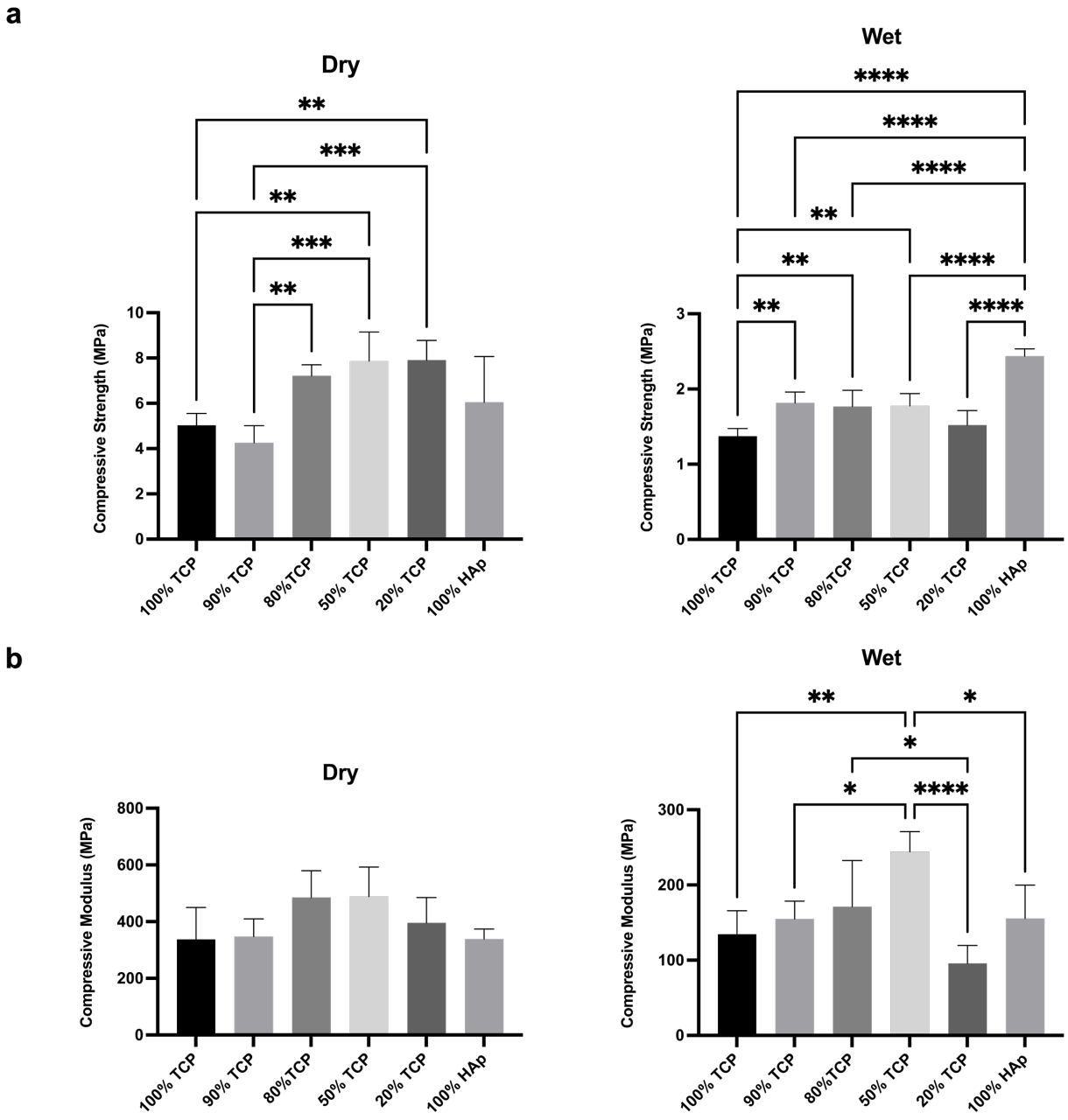

Figure 2-2. (a) Compressive strength and **(b)** compressive modulus (MPa) of different bone cement material compositions under dry and wet conditions. Bars represent mean ± SD (n = 5).

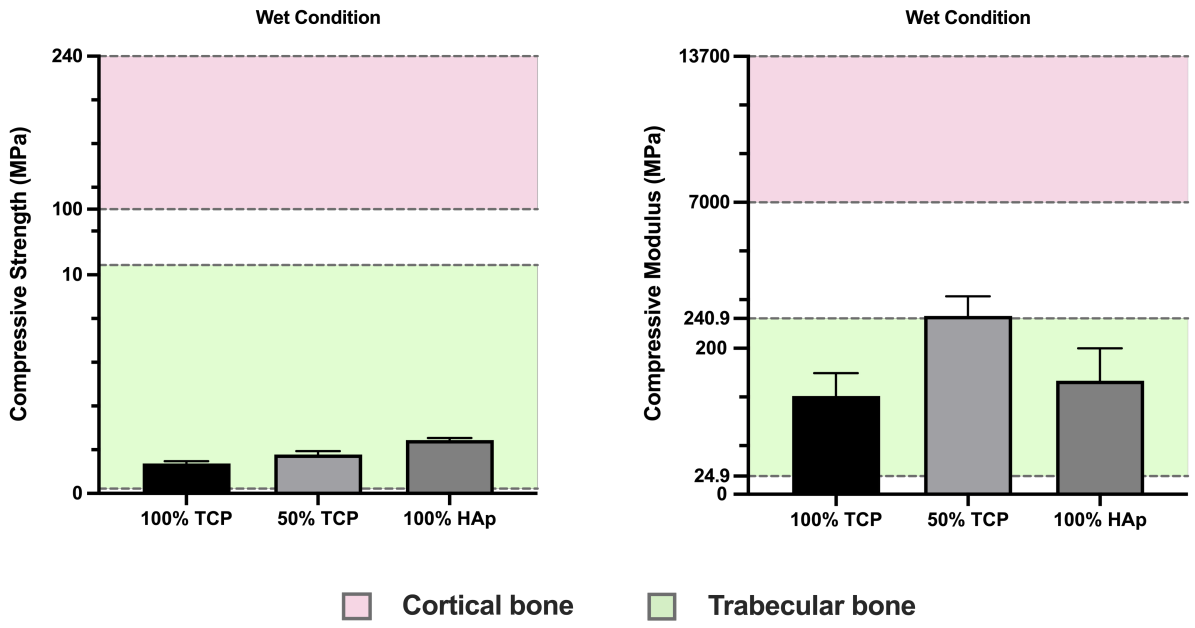

Figure 2-3. Comparison of compressive strength **(left)** and compressive modulus **(right)** of the selected bone cement material to trabecular bone in the human mandible, based on values reported by Misch et al. (1999). The dashed lines mark the upper and lower limits of cortical and trabecular bone mechanical properties. Bars represent mean ± SD. For reference, the cortical bone range is shaded in pink, and the trabecular bone range is shaded in green.

2.4.2. Rheology and Printability of Bone Cement. Rheological characterization was performed to assess the effect of silk on the extrusion behavior of the 503% β-TCP / 50% HAp bone cement ink (**Figure 2-4** and **Figure 2-5**). The addition of silk resulted in high viscosity at a low shear rate and a shear-thinning behavior with complex viscosity decreasing as the shear rate increased. In contrast, omitting silk from the ink led to a fluctuation in the flow curve at higher shear rates, which resulted in unstable shear-thinning behavior. Further, the amplitude sweep analysis showed that the bone cement maintained a viscoelastic behavior within the linear viscoelastic (LVE) region, where G' dominated G", and the material sustained strain levels up to 28.6% before yielding. Without silk, the material exhibited early structural breakdown at 8.25% stain and lacked a clear LVE region. In a frequency sweep test conducted at a 1% shear strain, the bone cement was able to maintain stable G' values higher than G" across a wide range of angular frequencies. The observed spike in both G' and G'' between 80 and 100 rad/s is attributed

to initial structural rearrangements occurring at the beginning of the frequency sweep. Finally, the temporal stability of the material was evaluated using a time sweep test under constant shear. The bone cement material was able to maintain consistent viscoelastic properties over 10 minutes of continuous shear with no structural breakdown.

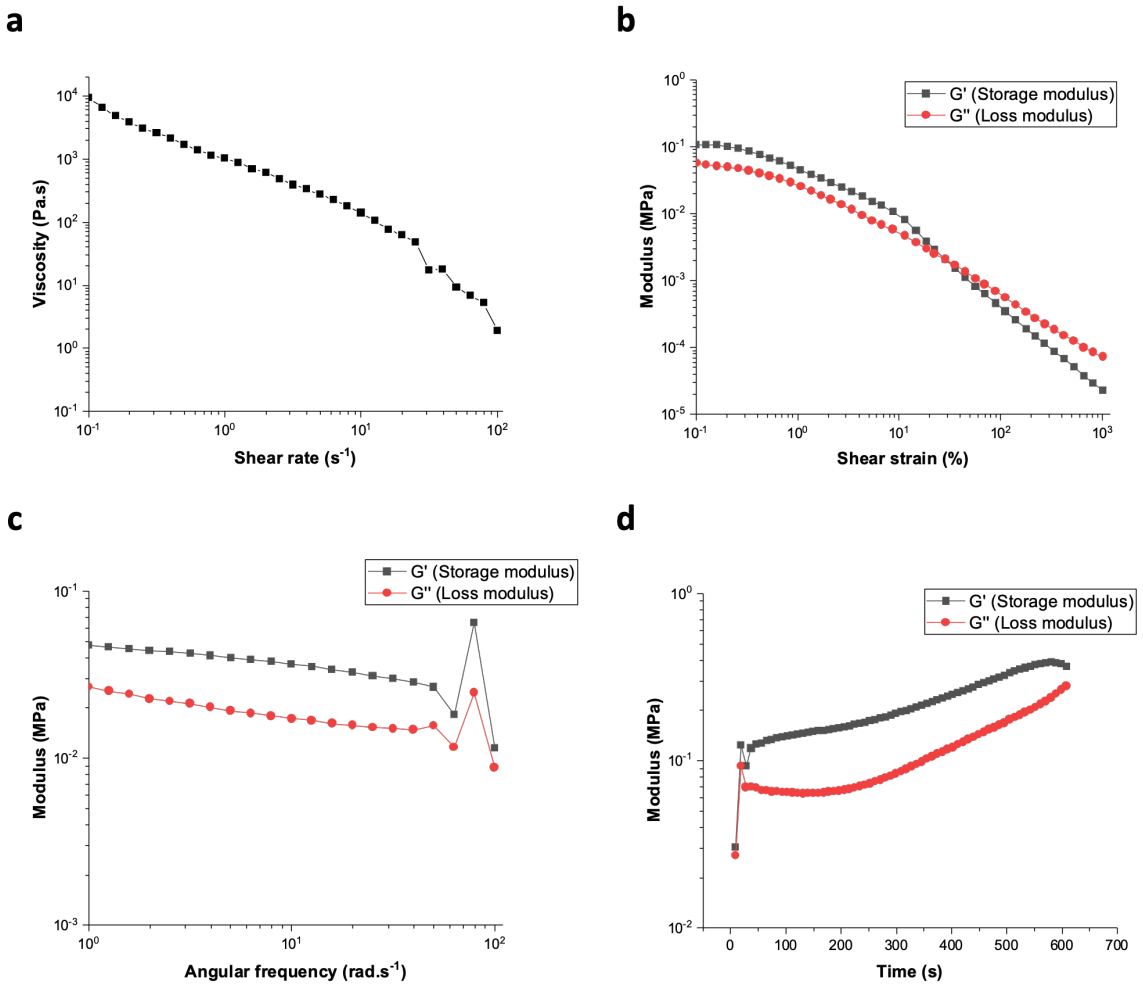

Figure 2-4. Rheological characterization of SF-BCP bone cement. **(a)** Flow behavior, **(b)** amplitude sweep, **(c)** frequency sweep, and **(a)** time sweep tests.

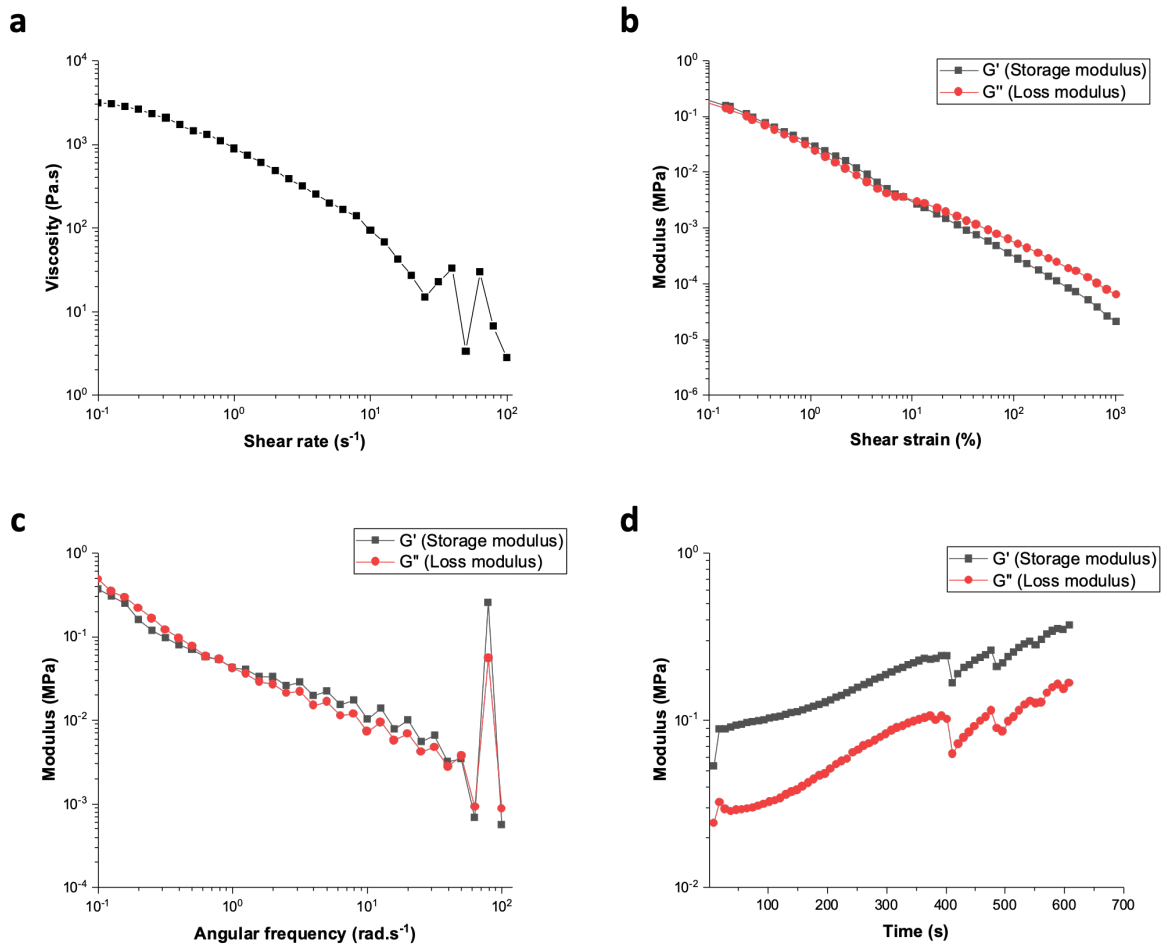

Figure 2-5. Rheological characterization of bone cement without SF inclusion. (a) Flow behavior, **(b)** amplitude sweep, **(c)** frequency sweep, and **(a)** time sweep tests.

The printability of the selected SF-BCP bone cement was evaluated using two key parameters, including printability index and spreading ratio, along with their associated geometric measurements (**Table 2-3**). The optimized ink containing silk exhibited high geometric fidelity with a printability index of 1.04 ± 0.8. The spreading ratio was 1.19 ± 0.2, suggesting that the extruded filament was slightly wider than the nozzle diameter (410 µm) but did not compromise the overall scaffold architecture (**Figure 2-6**a and **Figure 2-6**c, top). In contrast, the ink without silk was difficult to extrude and poorly adhered to the printing surface, which resulted in irregular filament

deposition and poor structure (**Figure 2-6**b and **Figure 2-6**c, bottom). Neither the printability index nor the spreading ratio could be calculated for the formulation without silk.

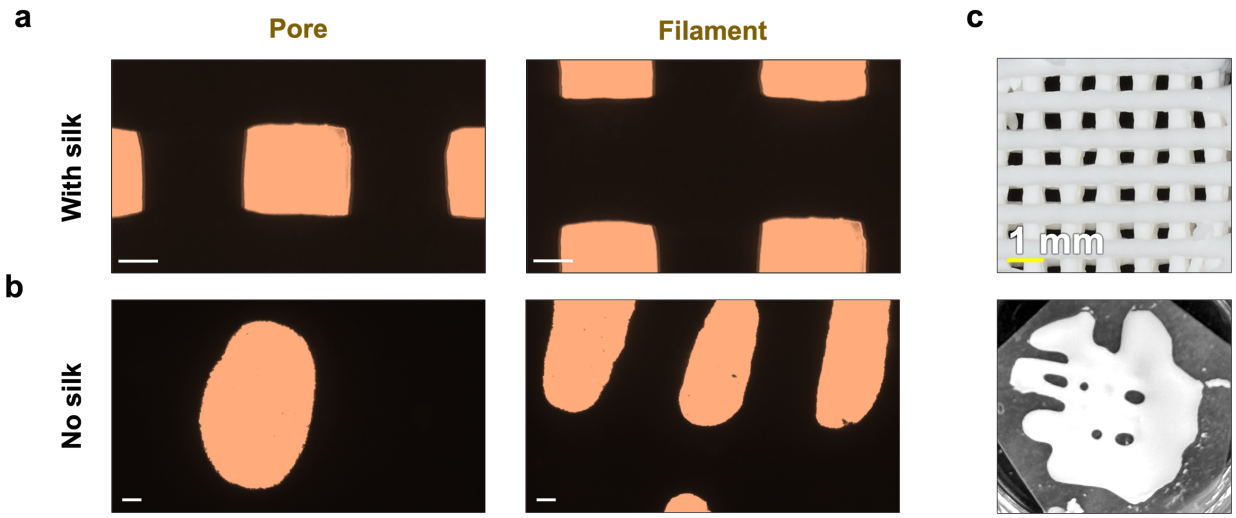

Figure 2-6. Microscopic images of printed scaffold filaments and pores: **(a)** scaffold with silk, showing well-defined geometry; **(b)** scaffold without silk, showing irregular and distorted shapes. **(c)** Macroscopic view of the printed grid structure with silk (top) and without silk (bottom). Scale bar = 200 µm.

Table 2-3. Printability parameters of the SF-biphasic ceramic bone cement ink containing silk fibroin. Values were measured from scaffolds printed using a 30% infill grid structure. Six sites were analyzed from three independent samples (n = 3).

Parameter	Mean ± SD
Printability index	1.04 ±0.8
Spreading ratio	1.19 ±0.2
Pore perimeter	2.22 mm ±0.39
Pore Area	0.31 mm ±0.14
Filament diameter	0.49 mm ±0.07

2.4.3. Characterization of the silk/biphasic ceramic-based bone scaffolds. The selected SF-BCP bone cement successfully extruded through the nozzle of the printer and formed filaments that could stack to form 11 x 2.5 mm cylindrical scaffolds with controlled macroporosity and interconnected pores with a filament diameter of approximately 400 µm (**Figure 2-7**). After printing, the scaffolds were placed in a humid environment to ensure slow setting and prevent cracking, transitioning from paste to solid state while maintaining structural integrity. To illustrate the practical use of the developed bone cement ink, a mandibular model with a critical-size defect measuring 22 mm x 29 mm x 21 mm was printed using a Fused Deposition Modeling (FDM) 3D printer (Prusa) with polylactic acid (PLA) filament. The bone cement was then utilized to 3D print a scaffold that accurately restored the defect (**Figure 2-8**).

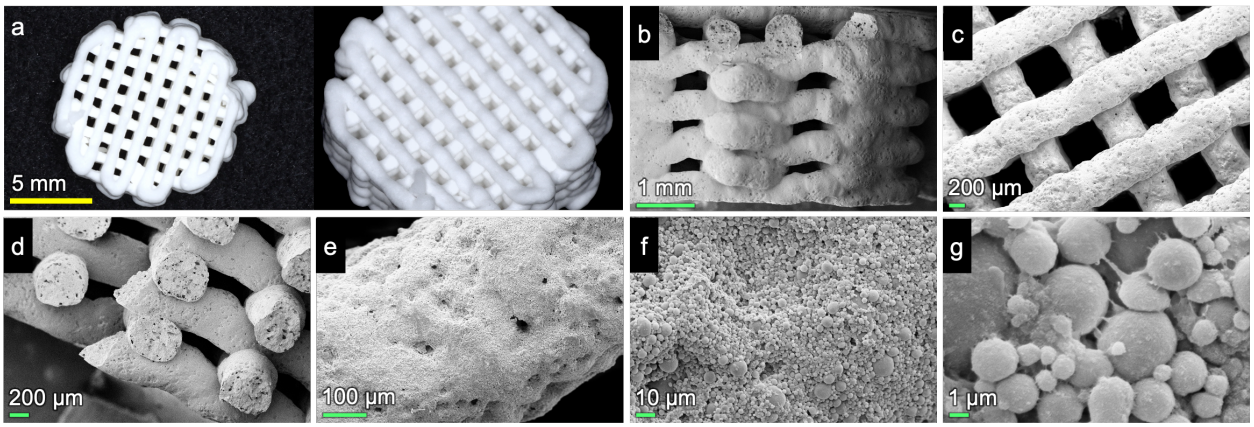

Figure 2-7. Characterization of the SF-BCP bone scaffolds. **(a)** 3D printed cylindrical scaffold. SEM for 3D printed constructs showcasing controlled deposition of filament and macroporosity **(b)** exterior perimeter **(c)** top view **(d)** interconnected internal network **(e)** filament size and microporosity **(f)** surface roughness **(g)** BCP particles embedded in the SF matrix.

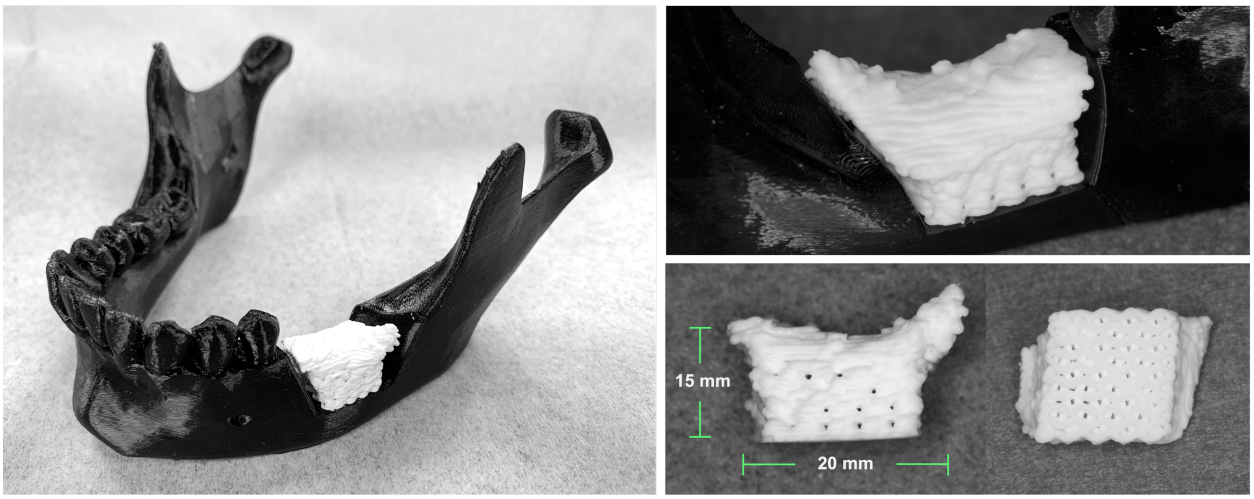

Figure 2-8. A critical-size defect in a mandibular model restored with a 3D printed SF-BCP scaffold.

2.4.4. Cytocompatibility. The cytotoxicity of the bone cement material was first assessed using an MTT assay on hMSCs exposed to dissolution product media. The 24 hours showed a reduction in cell viability below the 70% threshold. This effect is likely due to the accumulation of released calcium and phosphate ions or unreacted components from the bone cement material in the static media.[123-125] However, replenishing the media resulted in significantly higher viability, with the 72-hour media achieving a mean value of 84% (**Figure *2-9***). Based on these results, scaffolds were presoaked in a GM for at least 72 hours with media change prior to seeding to reduce the initial adverse effect on cell viability. Alamar Blue assay further assessed the cell viability for hMSCs seeded onto the printed scaffolds. The cells successfully attached and adhered to the scaffolds and occupied the internal structure (**Figure 2-10**). The Alamar Blue assay was used to monitor metabolic activity on different scaffold groups over day 28. In TCPS conditions, cells maintained consistently high metabolic activity levels throughout the observation period. Among experimental groups, scaffolds supplemented with hydrogel showed higher metabolic activity compared to those without hydrogel. In particular, those with hydrogel in OM (HSOM) showed a steady increase over time, followed by those in GM (HSGM). In contrast, the non-hydrogel groups

(USGM and USOM) exhibited moderate metabolic activity, with those in osteogenic media showing a continuous increase over time (**Figure 2-11**).

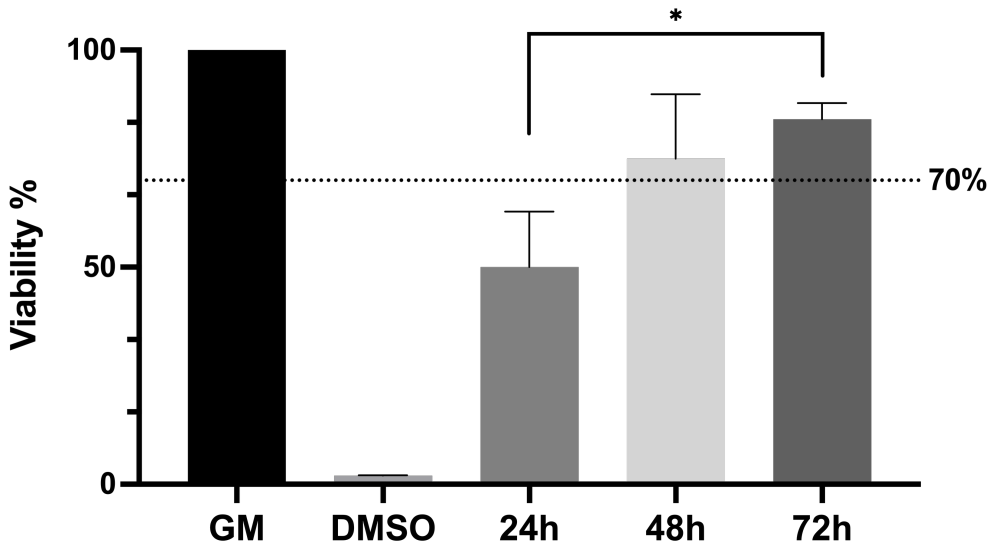

Figure 2-9. MTT hMSCs viability exposed to media with scaffold dissolution products (n = 3).

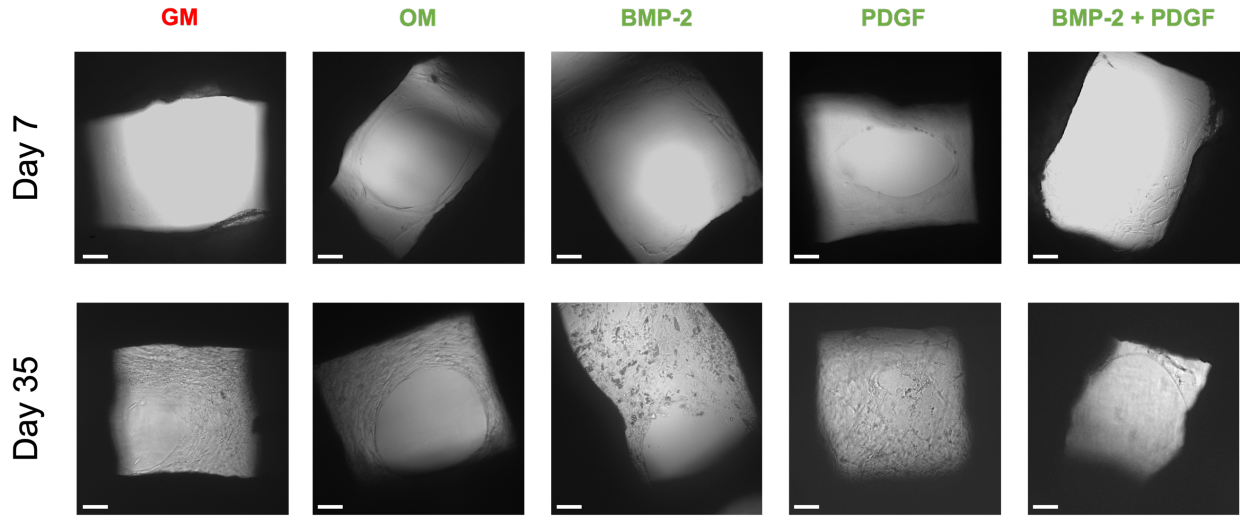

Figure 2-10. Brightfield images of hMSCs seeded on SF-BCP scaffolds with hydrogel after days 7 (top row) and 35 (bottom row). Scaffolds were maintained in either GM, OM, or functionalized with BMP-2, PDGF, or both factors in OM. Scale bars = 200 μm.

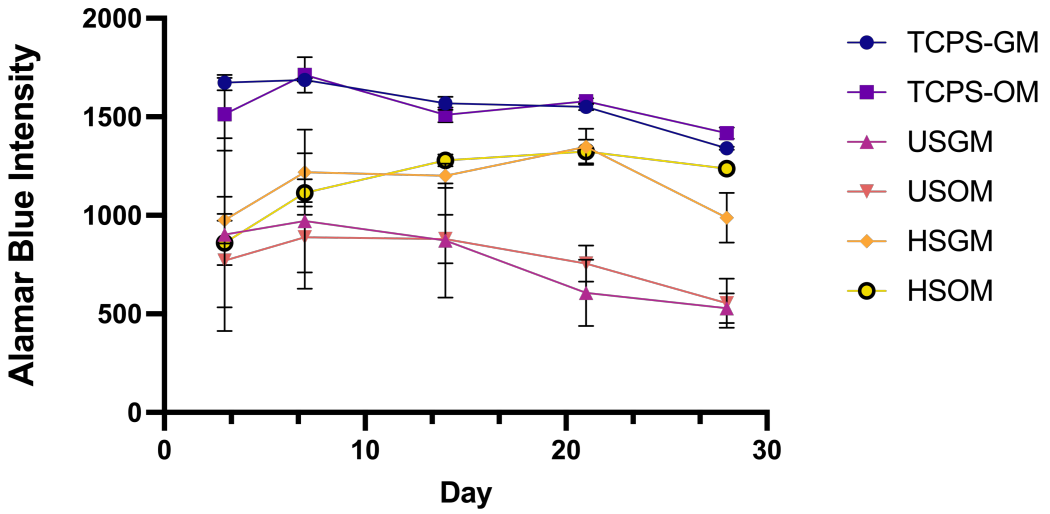

Figure 2-11. Alamar Blue assay (n = 3) showing metabolic activity of hMSCs over 28 days. Conditions include TCPS in GM (TCPS-GM) and OM (TCPS-OM), scaffolds without hydrogel in GM (USGM) and OM (USOM), and scaffolds with hydrogel in GM (HSGM) and OM (HSOM).

2.4.5. Osteogenic Potential. The scaffolds provided a supportive environment for cell colonization and new matrix formation (**Figure 2-12**). On day 7, SEM images showed active cellular attachment and spreading along the scaffold filaments with early ECM formation. By day 35, a progressive tissue development with osteoblasts extensively covering the filaments and the interconnected macropores was increasingly filled with a newly formed matrix and mineralization nodules on the surfaces (**Figure 2-12**b). Notably, the newly formed matrix bridging the pores of scaffolds in OM was evident upon visual inspection (**Figure 2-13**a). ALP enzyme activity assay was used to determine the early stages of osteoblastic differentiation. After the 21-day culture period, scaffolds in OM displayed significantly higher ALP activity than those in GM (**Figure 2-14**). Immunofluorescence staining for COL-I and COL-X was performed on day 35 to assess the nature of the ECM on the seeded scaffolds (**Figure 2-15** and **Figure 2-17**). The expression was positive for scaffolds with hydrogel in OM (HSOM), with fluorescence intensity significantly higher than those in GM (HSGM) (**Figure 2-16** and **Figure 2-18**).

2.4.6. Functionalization. The hydrogel was loaded with BMP-2 and PDGF or a combination of both (BP) to enhance the osteogenic outcome. All functionalized groups showed an increase in metabolic activity by day 7, followed by stable or slightly increased levels. BMP-2 and PDGF groups maintained higher fluorescence intensities throughout the 21-day observation period (**Figure 2-19**a). The ALP activity showed that scaffolds functionalized with BMP-2 had significantly higher ALP activity compared to the HSOM control and other functionalized groups. The PDGF-functionalized scaffolds displayed moderate ALP activity, which was significantly higher than the combined factors (BP). The combined factors resulted in the lowest ALP activity among all groups (**Figure 2-19**b). Despite the variations in ALP activity observed among the different groups, SEM imaging on day 35 consistently showed cellular growth and new ECM covering the filaments and pores, with mineralization nodules evident across all functionalized groups (**Figure 2-20Figure *2-22***). Visual inspection of the functionalized scaffold revealed extensive ECM coverage filling the pores, especially in scaffolds with BMP-2 (**Figure 2-13**b). In addition, all groups maintained in OM showed positive COL-I and COL-X expression with variable degrees along the scaffold filaments and across the macropores (**Figure 2-15** and **Figure 2-17**). Quantitative analysis of fluorescence intensity showed that COL-I expression was significantly higher in the BMP-2 functionalized group compared to those with PDGF and combined factors (BP) conditions, as well as the HSOM control (**Figure 2-16**). For COL-X, Immunofluorescence staining showed a strong signal in the HSOM and BMP-2 groups, while minimal expression was observed in the PDGF and BMP-2 + PDGF groups. Quantitative analysis showed significantly higher normalized fluorescence intensity in the osteogenic media and BMP-2 groups compared to the control HSGM condition (**Figure 2-18**).

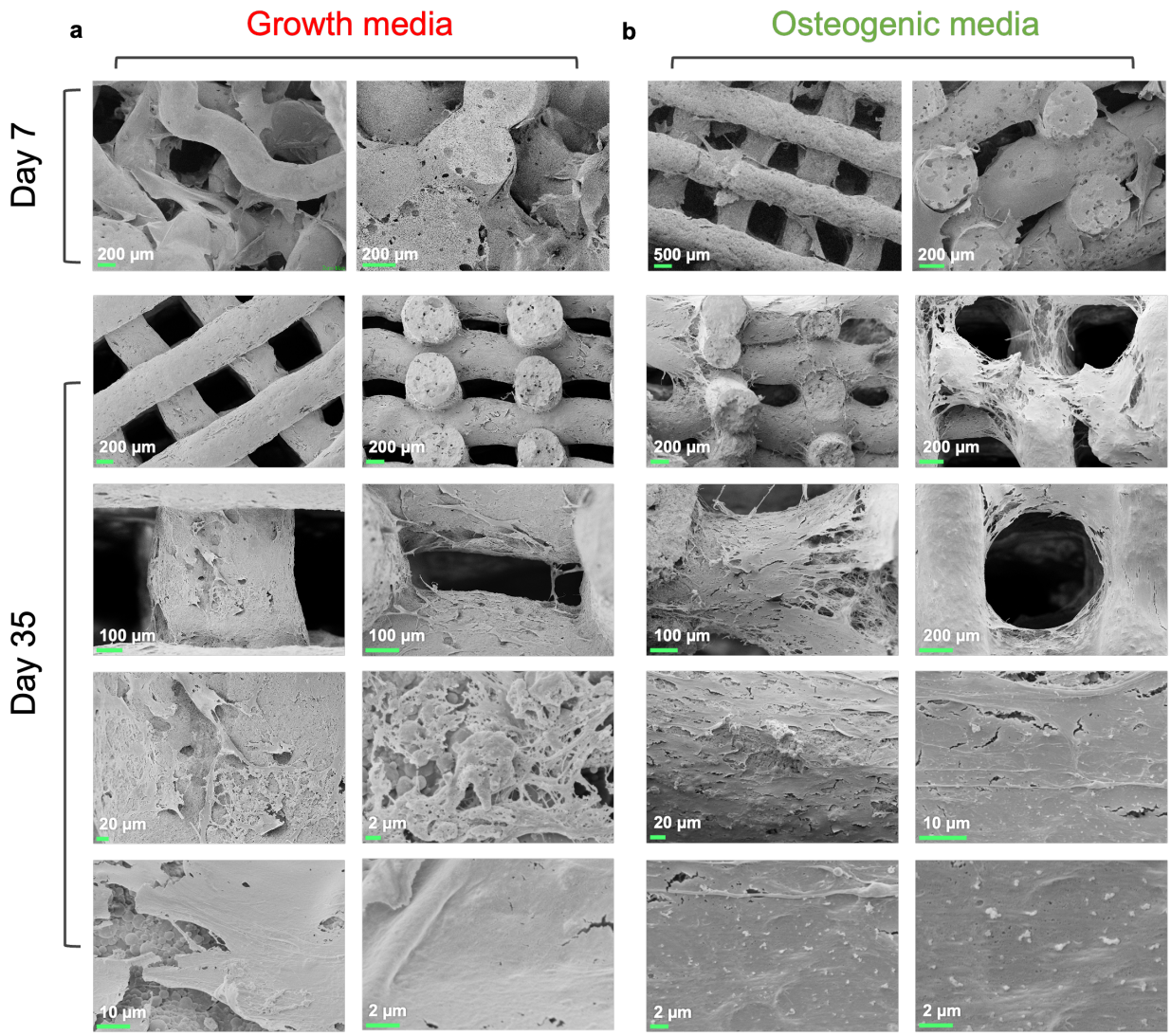

Figure 2-12. SEM images of SF-BCP scaffolds supplemented with hydrogel and seeded with hMSCs and cultured for 7 and 35 days in **(a)** growth media and **(b)** osteogenic media, showing cell attachment, scaffold coverage, and extracellular matrix formation at various magnifications.

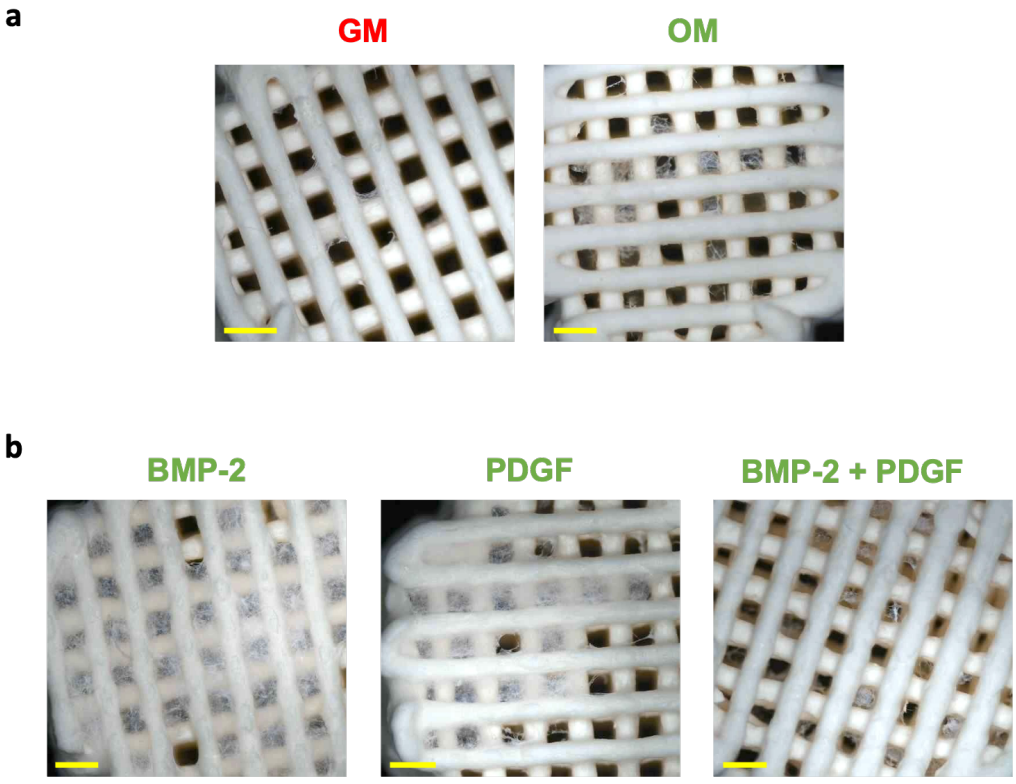

Figure 2-13. Representative SF-BCP scaffolds after 35 days of culture with hMSCs. **(a)** Scaffolds in GM and OM. **(b)** scaffolds cultured in OM and functionalized with BMP-2, PDGF, or both factors. Visible matrix deposition was observed in all osteogenic conditions, with varying degrees of pore bridging and surface coverage. Scale bar = 1 mm.

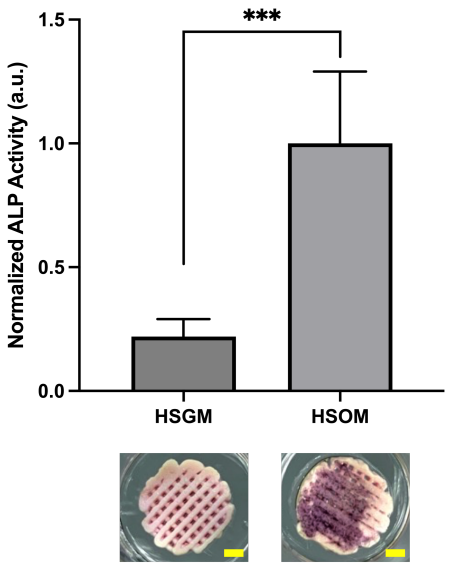

Figure 2-14. Osteoinductivity of scaffolds supplemented with hydrogel. Normalized ALP activity after 21 days of culture with hMSCs in GM (HSGM) and OM (HSOM). Each bar represents the mean ± standard deviation (n = 9). Representative ALP staining on day 21 shows a scaffold in growth medium (bottom left) and another in osteogenic medium (bottom right). Statistical analysis was performed using independent samples t-test ****p < 0.0001. Scale bars = 2 mm.

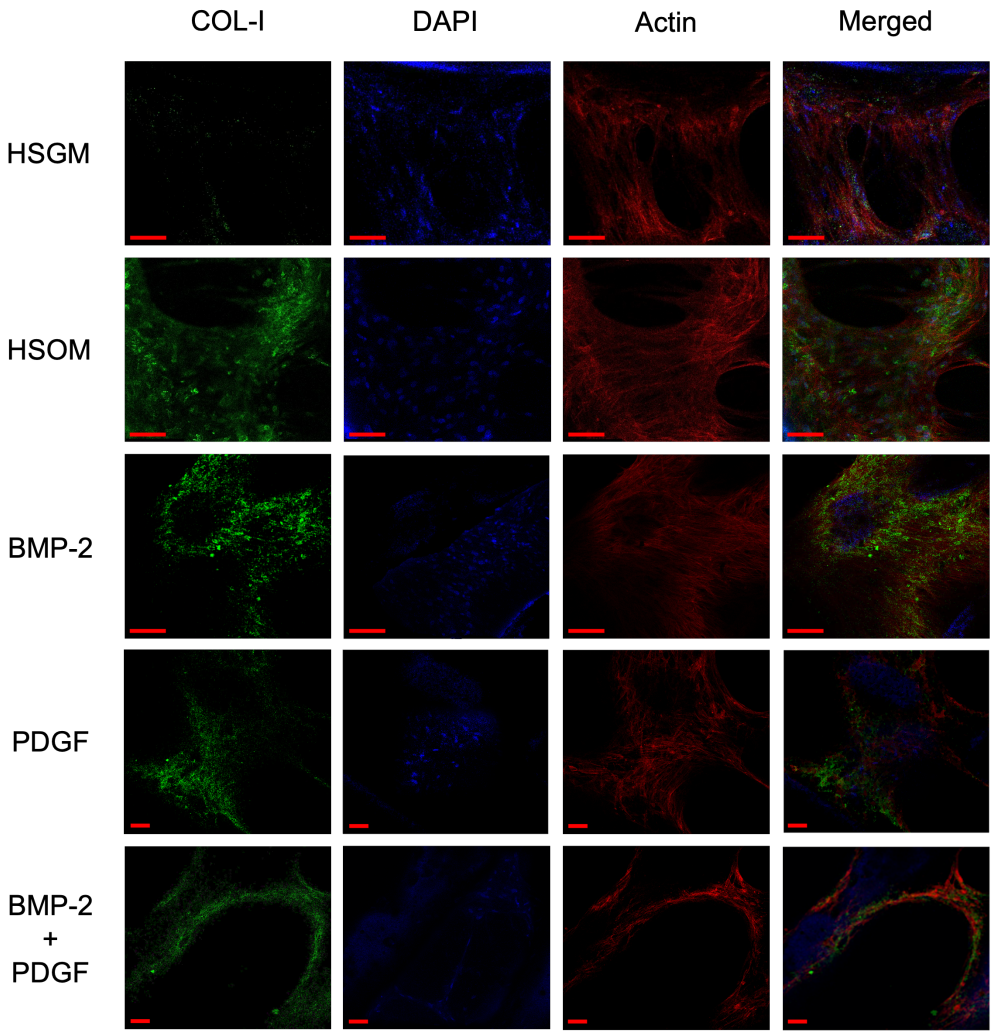

Figure 2-15. Immunofluorescent staining of Collagen I (COL-I) expression on SF-BCP scaffolds with hydrogel after 35 days of incubation. Representative images show COL-I (green), nuclei (blue), and actin (red) staining under different conditions: scaffolds cultured in GM, OM, and functionalized with BMP-2, PDGF, and BMP-2 + PDGF (BP). Scale bar = 100 μm.

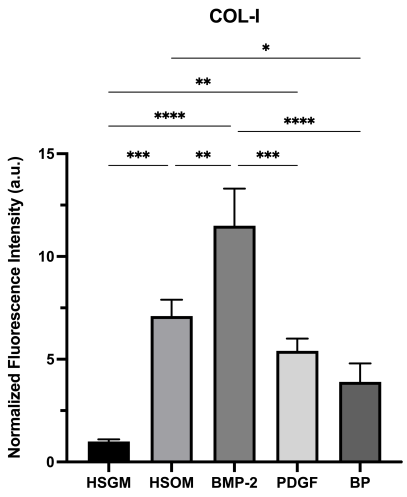

Figure 2-16. Quantification of COL-I fluorescence intensity normalized to the GM control. Conditions include scaffolds cultured in GM (HSGM), OM (HSOM), and scaffolds functionalized with BMP-2, PDGF, and BMP-2 + PDGF (BP).

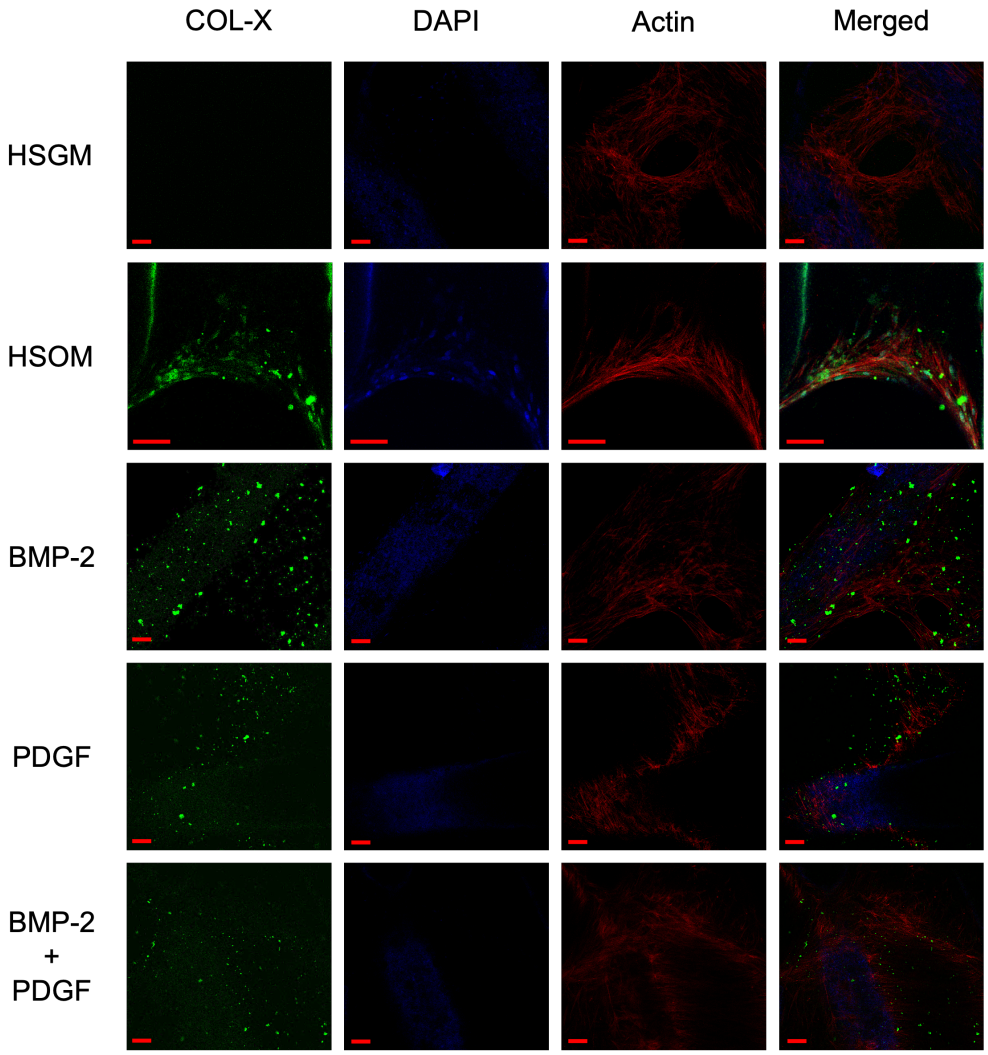

Figure 2-17. Immunofluorescent staining of Collagen X (COL-X) expression on SF-BCP scaffolds with hydrogel after 35 days of incubation. Representative images show COL-X (green), nuclei (blue), and actin (red) staining under different conditions: scaffolds cultured in GM, OM, and functionalized with BMP-2, PDGF, and BMP-2 + PDGF (BP). Scale bar = 100 μm.

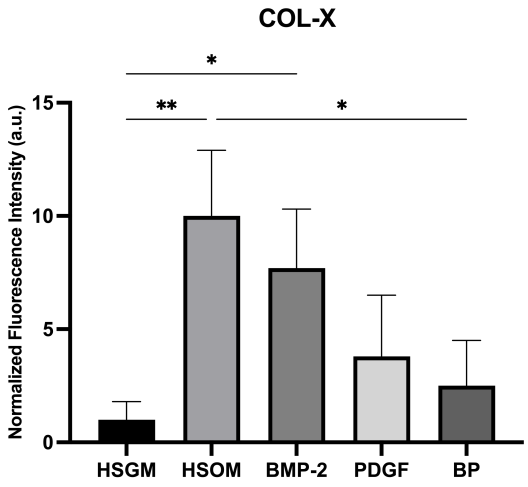

Figure 2-18. Quantification of COL-X fluorescence intensity normalized to the GM control. Conditions include scaffolds cultured in GM (HSGM), OM (HSOM), and scaffolds functionalized with BMP-2, PDGF, and BMP-2 + PDGF (BP).

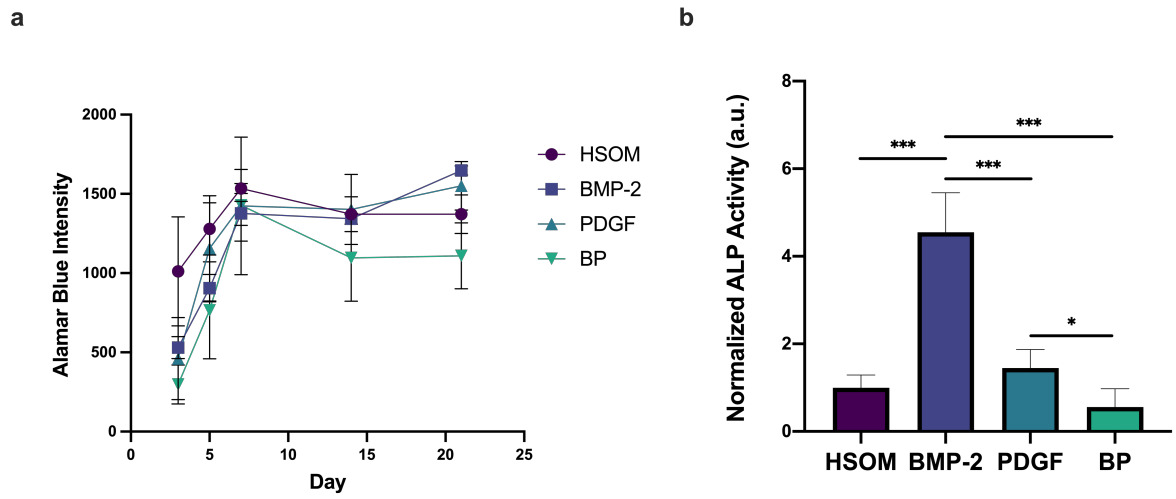

Figure 2-19. Osteoconductivity of functionalized scaffolds. (a) Alamar Blue assay (n = 6) showing cell metabolic activity over 21 days **(b)** Normalized ALP activity (n = 9) of the functionalized groups and the HSOM control. Data represent mean ± SD (***p ≤ 0.001).

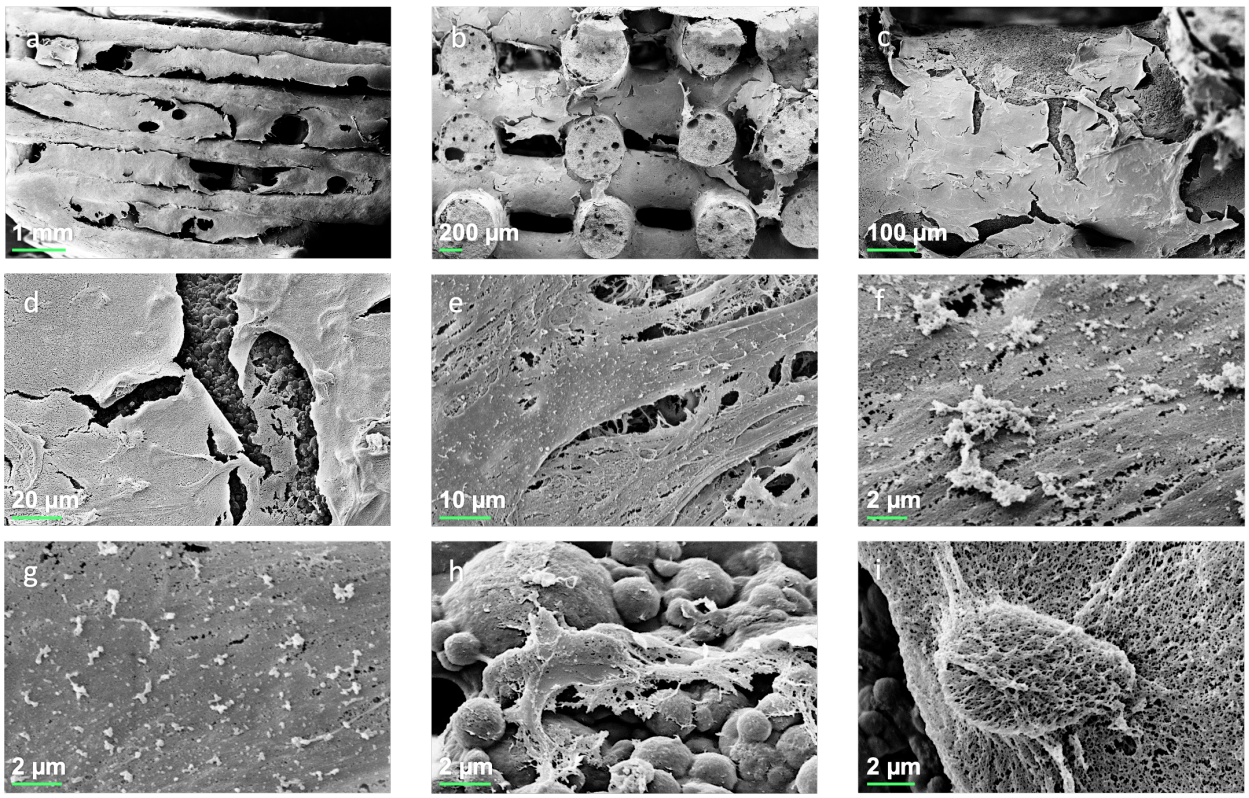

Figure 2-20. Functionalization with BMP-2. SEM images of the functionalized scaffolds after 35 days of culture with hMSCs in osteogenic media showing cell coverage and ECM deposition at different magnifications.

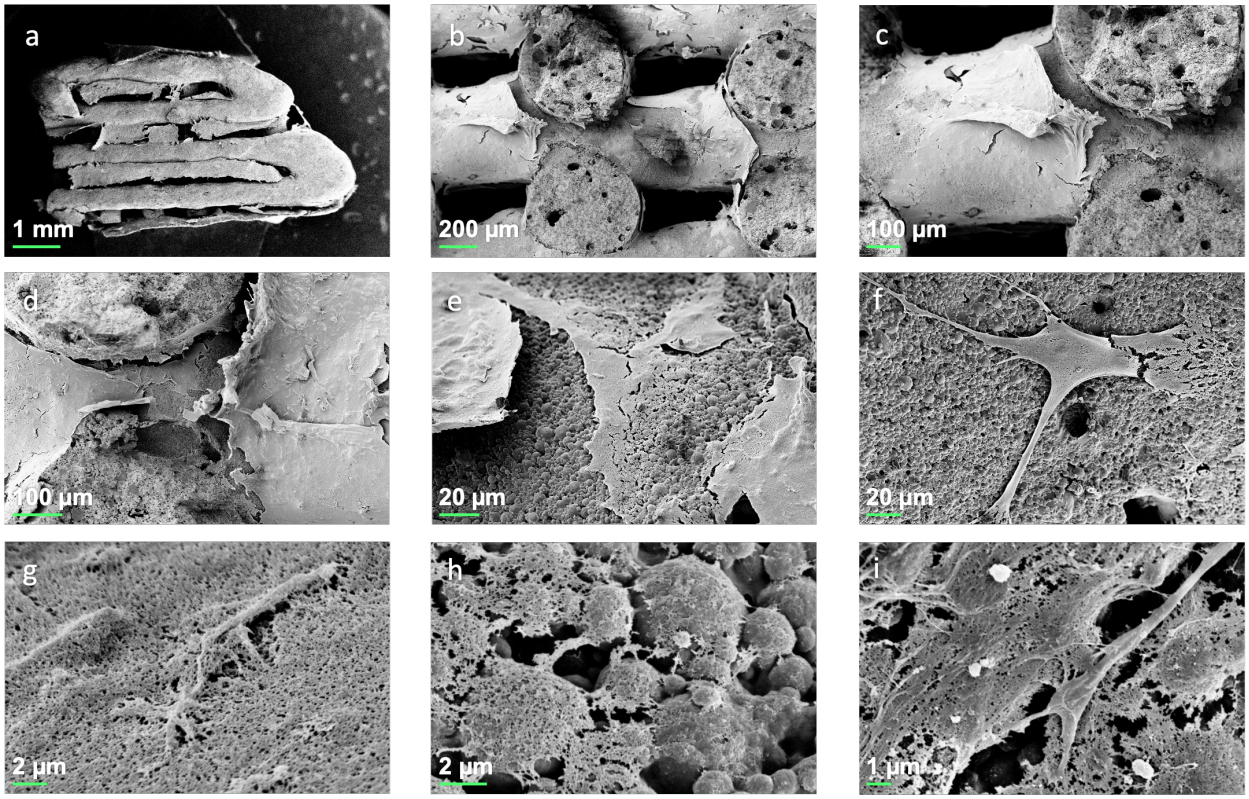

Figure 2-21. Functionalization with PDGF. SEM images of the functionalized scaffolds after 35 days of culture with hMSCs in osteogenic media showing cell coverage and ECM deposition at different magnifications.

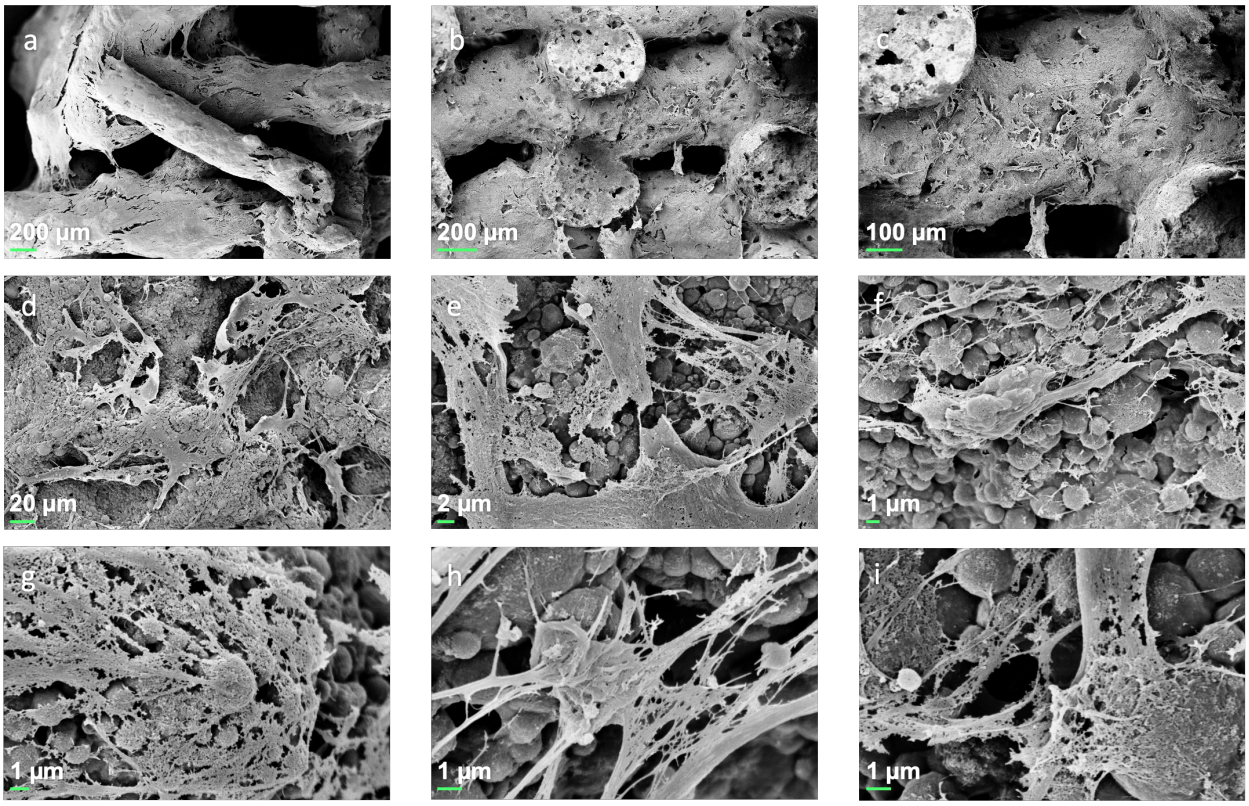

Figure 2-22. Functionalization with combined factors (BMP-2 + PDGF). SEM images of the functionalized scaffolds after 35 days of culture with hMSCs in osteogenic media showing cell coverage and ECM deposition at different magnifications.

2.4.7. Growth factors release profile. ELISA was performed to analyze the release of BMP-2 and PDGF from scaffolds under different loading conditions. The delivery strategies included direct incorporation of growth factors into the scaffold structure, either by premixing them into the bone cement before mixing (-L), or by soaking the printed scaffold in growth factor solutions (-S), as well as encapsulated in an HA hydrogel carrier injected into the constructs. All scaffolds were supplemented with 1 µg of BMP-2, PDGF, or both (BP) and then incubated in PBS at 37 °C. Media samples were collected at different time points. In the non-hydrogel conditions, scaffolds soaked in growth factor solutions showed a burst release within the first hour, followed by a decline. In the PDGF measurement, a second peak release was observed toward the end of the observation period, particularly in the combination group (BP-S). By day 7, the cumulative release reached only 4.3% for BMP-2-S and 4.7% for PDGF-S. In contrast, the scaffolds with growth factors incorporated directly in the bone cement exhibited no release throughout the observation period for both growth factors (**Figure 2-23**). For the hydrogel-based groups, scaffolds were injected with HA hydrogel containing the growth factors. The BMP-2 release study exhibited a peak release after one hour, followed by a lower concentration release in the subsequent time point. Despite that, the release continued consistently until the end of the study, with different percentages for both BMP-2 alone and in combination with PDGF (BP). The cumulative release of BMP-2 alone on day 7 was 19.40% of the initial dose, and with PDGF, it rose to 24.15%. (**Figure 2-24**a). In the case of PDGF, all samples, including single and combined factors, showed a similar release pattern. The release peak was at 1 hour and on day 7 of sample collection (168 hours). A sustained release pattern was observed between these time points, indicating a continuous and controlled delivery of PDGF. The cumulative release of PDGF alone on the last sample collection time point was 31.72%, and with BMP-2, it reached 32.56% over the entire duration (**Figure 2-24**b).

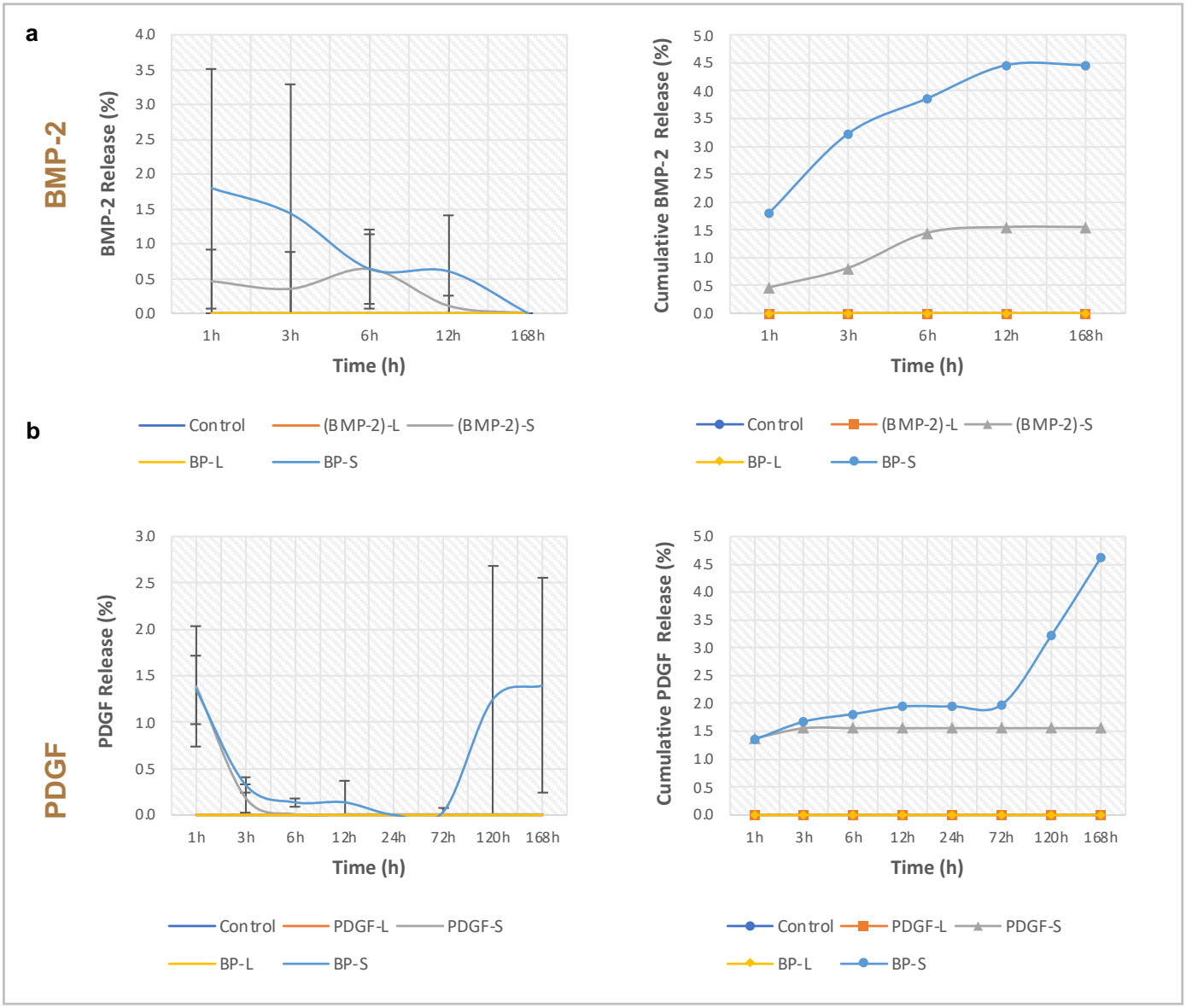

Figure 2-23. Release kinetics of BMP-2 and PDGF from scaffolds without hydrogel **(a)** BMP-2 and **(b)** PDGF. Conditions: control, growth factors-socked (-S), growth factors-loaded (-L). The release over time was calculated as a percentage of the initial amount loaded (1 µg of BMP-2, PDGF, or a combination of both growth factors (BP)). Cumulative release over time as a percentage of the total initial amount loaded, with the additional incremental release recorded at each subsequent sampling point. Data represent mean ± SD (n = 3).

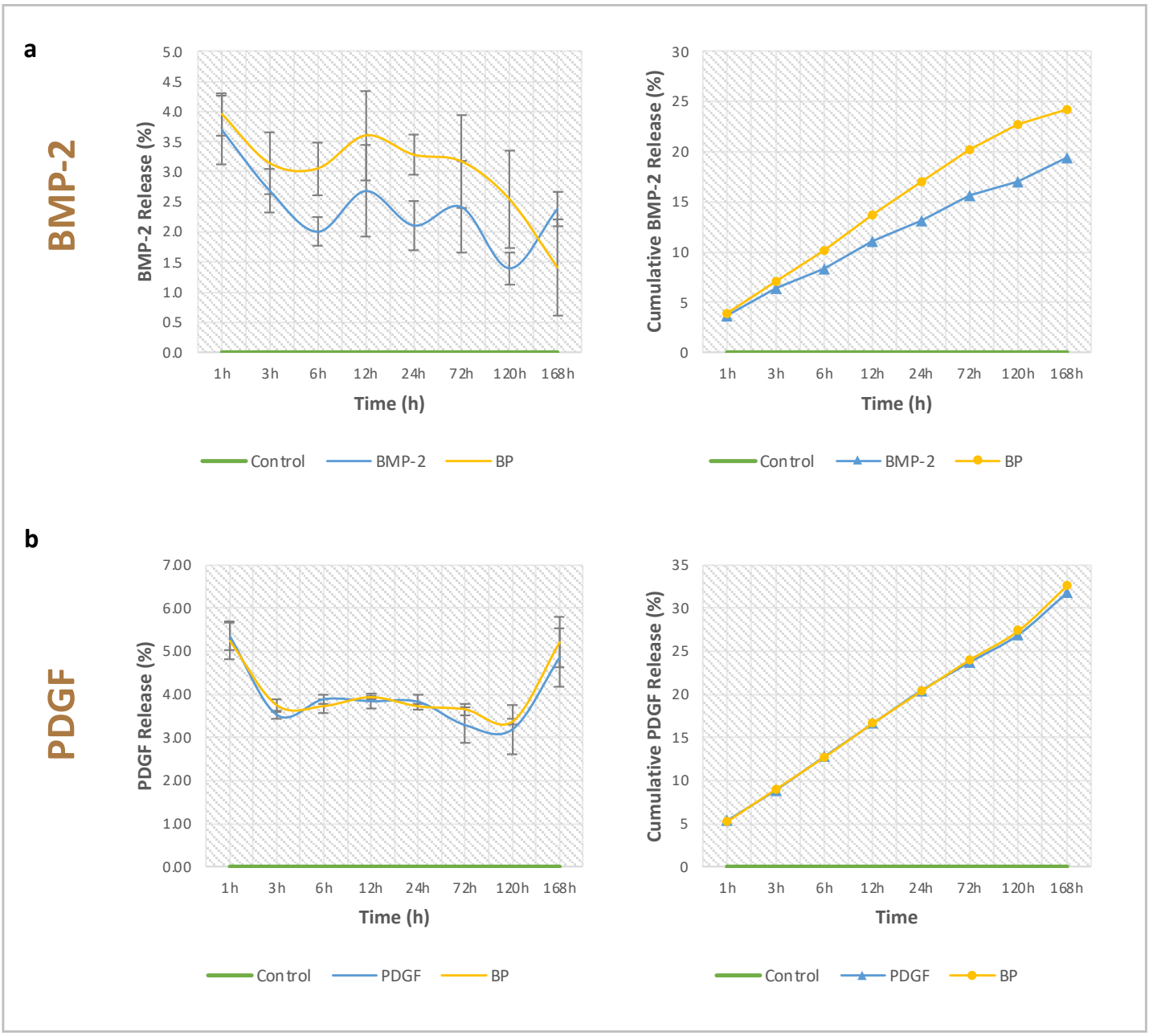

Figure 2-24. Release kinetics of BMP-2 and PDGF from scaffolds loaded with HA hydrogel. **(a)** BMP-2 and **(b)** PDGF. The growth factor release over time was calculated as a percentage of the initial amount loaded (1 µg of BMP-2, PDGF, or a combination of both growth factors (B/P)). Cumulative release over time as a percentage of the total initial amount loaded, with the additional incremental release recorded at each subsequent sampling point. Samples were analyzed using a commercially available sandwich ELISA kit based on human BMP-2 and PDGF. Data represent mean ± SD (n = 3).

2.5. Discussion

The alveolar bone is part of the periodontal tissues that provide essential support to teeth. It consists of two cortical plates that envelop a central trabecular bone core. This configuration provides the strength and resilience necessary to accommodate the mechanical demands of various dental functions.[16] After tooth loss, the alveolar bone can undergo significant resorption and structural changes, often leading to insufficient bone volume for dental implant placement.[6, 26, 27, 126] Achieving optimal prosthetic outcomes in such cases becomes challenging and requires bone augmentation procedures to restore the lost volume. However, current augmentation techniques often fail to address CSDs due to limitations in grafting materials, vascularization, integration with the surrounding tissues, and structural stability.[6, 9, 126] This in vitro study aimed to explore a bioengineered approach for alveolar bone regeneration. The objective was to develop a bone cement material suitable for 3D printing scaffolds that combine structural stability with biocompatibility and osteoconductivity. These scaffolds were further functionalized with a hyaluronic acid/gelatin hydrogel loaded with BMP-2 and PDGF to enhance osteogenesis. The outcomes of the study confirmed the initial hypothesis and confirmed that the SF-BCP composite scaffolds supported hMSCs' adhesion, proliferation, and osteogenic differentiation, with the BMP-2 functionalized group showing the most osteoinductive effect. This combined strategy offers a potential solution for restoring complex alveolar bone defects through localized growth factor delivery and supportive scaffolds.

2.5.1. Material Development and Structural Properties

Matching the mechanical properties of bone implants to the native bone at the implantation site ensures proper load transfer and early osseointegration. This can minimize stresses at the bone-scaffold interface, prevent bone resorption, and ensure scaffold stability.[83] Previous studies have shown that combining silk with HAp creates a material that can be tuned to match the chemical

composition and mechanical properties closer to those of native bone.[82, 88, 93] In this study, the Ink composition containing 27% SF and equal parts of TCP and HAp demonstrated the most favorable mechanical properties, with a compressive strength of 1.78 ± 0.16 MPa. This value falls within the range reported for trabecular bone in the oral cavity (0.22 to 10.44 MPa), making it suitable for oral applications, particularly for alveolar ridge augmentation.[127, 128] 3D printing has revolutionized the field of tissue engineering and regenerative medicine by allowing for a customizable approach tailored to individual needs.[75, 129-131] Successful printing requires a material with optimal rheological properties. Materials with a shear-thinning behavior have a lower viscosity under shear, reducing the risk of clogging the nozzle during printing and ensuring continuous filament extrusion. Furthermore, a viscoelastic behavior ensures that the printed structure solidifies and retains its intended shape after deposition.[81, 132, 133] The tested bone cement material demonstrated good printing parameters. Rheological analysis showed that the bone cement ink exhibited a stable viscoelastic behavior necessary for extrusion and shape fidelity after printing. Within the viscoelastic region, G' dominated G'', and as the shear increased, the material began to flow at the crossover point between the moduli. The incorporation of silk in CaP-based inks has been shown to improve the ductility of the material, which helps to reduce under-extrusion and prevents the collapse of the printed structure.[81, 82] The presence of silk in the ink used in this study effectively bound the TCP and HAp particles. It resulted in a printable material with a stable structure and shear-thinning behavior that allowed smooth extrusion of filaments while maintaining structural integrity after deposition. The printability index exhibited a value close to 1, which indicated high print accuracy. However, the spreading ratio slightly higher than 1 indicated an extruded filament diameter wider than the nozzle used but without any significant effect on the integrity of the print or the osteogenic properties of the scaffolds. The precise control over shape allowed the extruded filaments to stack and form a macroporous structure with interconnected pore sizes >300 μm. This configuration has been shown to promote osteogenesis by meeting the requirements for bone cell migration, vascularization, and

oxygenation.[72] In addition, a complex scaffold structure restoring an alveolar defect in a mandibular model was successfully printed. The material continuously flowed through the nozzle, and overhanging parts were printed without any additional support. This is particularly important for printing complex structures like the alveolar bone, which requires an extended window for material extrusion and consistent printing. This confirmed the suitability of the material for the intended clinical application.

2.5.2. Biological Performance and Osteogenic Potential

Silk-based scaffolds have shown great promise in bone tissue engineering because of their biocompatibility, adjustable degradability, and remarkable mechanical properties derived from their β-sheet structure. This unique structure provides mechanical stability and is believed to support mineralization and calcium phosphate formation.[83, 84] Furthermore, the incorporation of CaP-based materials in SF scaffolds enhances their osteoconductive properties and mechanical strength by mimicking the inorganic component of natural bone. The release of calcium and phosphate ions from the composite material creates a bioactive environment that supports new bone tissue formation.[83, 134] In this study, the 3D printed scaffolds supported hMSC adhesion, proliferation, and differentiation, with metabolic activity steadily increasing throughout the incubation period. The addition of an HA-based hydrogel improved scaffold performance by creating a hydrated environment that facilitated early cellular colonization and matrix deposition. The incorporation of HA-based hydrogel has been widely reported to enhance scaffold performance by mimicking the natural ECM, supporting cell adhesion, proliferation, and early matrix formation.[135] In addition, HA hydrogels are known for creating a microenvironment that promotes osteogenic differentiation.[136, 137] They also facilitate nutrient diffusion and can be chemically modified for tunable degradation and mechanical reinforcement.[135] Studies found that the incorporation of HA-based hydrogels in scaffolds for bone regeneration can enhance osteogenesis both in vitro and in vivo, making it an ideal strategy for bone application and

enhanced biological performance.[11, 136] Indeed, a bone-like tissue was evident covering the scaffold filaments and infiltrating the interconnected macropores, with cells differentiated in those incubated in an osteogenic medium. The newly formed matrix showed COL-I and COL-X expression with mineralized nodules visible on the surface and deep within the scaffolds. Furthermore, the scaffold showed significantly higher osteoinductivity with high ALP activity in those cultured in an osteogenic medium. These findings suggest that the combination of scaffolds and hydrogel fosters an environment favorable to osteogenesis, with the potential of this approach to support bone formation beyond the limits of bone defects.

2.5.3. Growth Factors Delivery: Release Kinetics and Osteogenic Effect

The functionalization of SF-biphasic scaffolds with BMP-2 and PDGF aimed to create osteoinductive constructs by employing a biomimetic strategy that enables a localized and spatiotemporal controlled growth factor release. BMP-2 and PDGF are the only recombinant growth factors approved by the FDA for specific craniofacial applications.[94] Both have been extensively studied for their roles in bone regeneration and are used in dentistry for periodontal defect repair, alveolar bone regeneration, and implant site development. Clinically, the commercially available recombinant BMP-2 and PDGF are delivered in an adsorbable collagen sponge and β-TCP matrix as carriers, respectively.[94] These carrier systems have shown clinical efficacy in small defects but limited outcomes in larger defects. Despite that, the currently available materials still have shortcomings.[102, 104] A major issue with BMP-2 is the need for supraphysiological doses that exceed natural levels (typically 30–150μg/mL, with some clinical applications reaching 1,500 μg/mL) to achieve osteogenic effects.[138, 139] This is mainly due to the limited capacity of currently available carriers to control the release kinetics, resulting in rapid degradation of the morphogen. Such high doses can lead to complications like ectopic bone formation and inflammation.[108, 140] It has also been reported that higher BMP-2 concentrations (150-600 μm/mL in the rat model) may result in void spaces filled with fatty marrow tissue rather

than normal trabecular bone.[138] In case of PDGF, the application is generally considered safe for clinical applications with no significant adverse effects. However, the available carrier for PDGF often requires additional grafting material for additional support, and the clinical effectiveness is dose-dependent, with not enough evidence to define ideal therapeutic concentrations.[107, 141, 142]

The success of growth factor-based therapies in bone regeneration largely depends on the carrier system used for their delivery. An ideal carrier should maintain the bioactivity of the loaded molecules, offer controlled local release, support cell infiltration, and facilitate tissue integration.[143, 144] Various materials have been tested as a carrier system, such as CaP-based scaffolds, natural polymers like collagen sponges, silk, hyaluronic acid, and chitosan, as well as synthetic polymers.[145, 146] Although these materials provide structural support and influence the release kinetics of bioactive molecules, achieving an optimal balance among mechanical stability, degradation rate, spatiotemporal control, sustained release, and bioactivity remains a challenge in bioengineering.[145, 147]

In the present study, a controlled growth factor delivery system was integrated into 3D printed scaffolds. The initial delivery strategies, which relied on direct incorporation of BMP-2 and PDGF into the ink or post-print soaking into growth factor solution, were ineffective. Indeed, the ELISA analysis revealed undetectable or insignificant levels of released growth factors (**Figure 2-23**). This is likely due to growth factor degradation during material processing or irreversible binding within the scaffold structure. These outcomes are consistent with known limitations of physical entrapment strategies, which are often associated with poor retention, uncontrolled release of bioactive molecules, or entrapment within the carrier structure.[9] To address this, a different strategy was employed by incorporating an HA-gelatin-based hydrogel (HyStem-HP) as a carrier for BMP-2 and PDGF. This delivery system was designed to protect growth factors from degradation and control their release in a sustained manner. The high affinity of BMP-2 and PDGF for the heparin integrated into the hydrogel helped preserve their bioactivity. The hydrogel created an ECM-like environment that allowed for the gradual release and sustained availability of growth

factors. The ELISA results of the release study confirmed the effectiveness of heparin in maintaining the bioactivity of the growth factors and achieving sustained release over time. The controlled release mechanism ensured a prolonged bioavailability of osteogenic molecules. Beyond that, the hydrogel system could also offer a practical clinical method for bone regeneration. Its injectable nature enables site-specific delivery and efficient incorporation into scaffolds with complex geometry. Its sustained-release properties may eliminate the need for repeated growth factor administration. Furthermore, with this method, scaffolds can be sterilized before the addition of growth factors, which helps prevent the loss of bioactivity that could occur if the growth factors were directly mixed into the bone cement ink prior to printing. Instead, they are incorporated into the hydrogel and then can be injected into the scaffolds right before implantation. This approach offers a practical advantage for clinical handling and helps maintain the stability and shelf life of the loaded factors.

The functionalization of the scaffolds with BMP-2 and PDGF through the hydrogel system further enhanced their osteoinductive properties by promoting cell recruitment, supporting osteogenic differentiation, new matrix deposition, and mineralization. The osteoinductive effect of BMP-2 was confirmed by the significantly increased levels of ALP activity observed in BMP-2-functionalized scaffolds, in contrast to those functionalized with PDGF or combined factors. This trend was also evident in the immunofluorescence staining, where functionalization with BMP-2 resulted in a high expression of COL-I compared to other conditions. These findings suggest that a relatively lower BMP-2 dose (1 μg) delivered in a controlled manner was sufficient to enhance early osteogenic differentiation and contribute to new matrix development without the need for high concentrations. While BMP-2 plays a well-established role in promoting osteogenic cell differentiation, PDGF primarily functions as a mitogenic and chemotactic factor. The contribution of PDGF to bone regeneration in this scaffold design was limited to increased levels of cell proliferation and had only a minimal effect on directly increasing ALP activity (**Figure 2-19**). Higher COL-X expression was observed in the osteogenic media and BMP-2 groups compared to the

PDGF and combination groups. Given the role of collagen X in mineralization by regulating matrix vesicle distribution, these findings may suggest an advanced matrix maturation. The differences in COL-X expression among the testing conditions most likely reflect a variation in the extent or timing of maturation rather than the absence of mineralization in the PDGF or combined factors groups.

The lack of an enhanced osteoinductive effect in the co-functionalized groups suggests that PDGF-BB may have interfered with BMP-2-mediated osteogenic differentiation. Although PDGF-BB is essential during the early phase of bone healing due to its role in promoting stem cell recruitment, proliferation, and migration by activating its cell surface receptor PDGFRβ, its continued signaling may hinder BMP-2-driven osteogenic differentiation. BMP-2 plays an important role in osteogenic differentiation by activating the Smad1/5/8 signaling pathway, which upregulates key transcription factors like Runx2 and osterix, essential for MSCs' commitment to differentiate into bone-forming cells and their maturation and function.[98, 148, 149] The activation of PDGFRβ on the MSC surface by PDGF-BB inhibits the canonical BMP-2/Smad1/5/8 signaling pathway by downstream activation of ERK1/2 MAPK and PI3K/AKT pathways, which in turn suppresses the transcription of Runx2 and osterix. As a result, the MSCs remain in a proliferative state rather than progressing toward osteogenic commitment.[148, 149] In a study by Tokunaga et al, they reported that the depletion of PDGFRβ in a mouse model resulted in decreased cell proliferation and migration and enhanced osteogenic differentiation as evidenced by increased ALP activity, and upregulated expression of Runx2, OCN, and osterix. On the contrary, in the presence of PDGFRβ, stimulation with PDGF-BB led to reduced osteogenic gene expression and ALP activity.[150] Their findings align with those observed in our results, where the simultaneous delivery of PDGF and BMP-2 did not enhance early osteogenic differentiation, suggesting that PDGF-BB may have disrupted the action of the co-delivered BMP-2. However, this regulatory interaction was not tested in this study as it falls beyond the scope of this investigation. Our data emphasize the importance of the spaciotemporal control in growth factor delivery. PDGF-BB is

most important during the initial wound healing phase to stimulate cell migration and proliferation, and BMP-2 is more effective in the subsequent phase of healing to induce osteogenic differentiation. In this study, both factors were co-delivered through a hydrogel system injected inside the scaffolds, potentially contributing to the reduced osteogenic outcome and highlighting the need for a different strategy for effective temporal release.

2.6. Future Directions

Given the promising results presented in this study, several avenues can be explored to further enhance the regenerative performance of the functionalized SF-BCP scaffolds for future clinical applications. Understanding the late-stage osteogenic differentiation can give insight into the nature of the newly formed matrix. Although COL-1 was assessed as a marker of ECM formation, additional assessment of late-stage osteoblastic differentiation markers could further validate the maturation of the osteoblastic phenotype and matrix mineralization. Traditional histological staining methods for Calcium, such as Von Kossa, were not feasible due to the CaP content of the scaffolds. Alternatively, ELISA quantification and immunofluorescent staining of late-differentiation markers such as OPN and OCN could be employed. OPN is involved in bone remodeling and plays a role in osteoblastic cell-matrix interactions during mineralization. At the same time, OCN is considered a marker of mature osteoblasts and is directly associated with bone matrix maturation and calcium ion binding.

The simultaneous delivery of BMP-2 and PDGF in the hydrogel system used in this study did not enhance osteogenic differentiation, suggesting a possible interference between the signaling pathways induced by both factors. To address this, a dual-release strategy allowing temporospatial controlled release may offer better osteogenic outcomes. For instance, PDGF could be released early from the hydrogel matrix to support cell recruitment and angiogenesis, while BMP-2 could be encapsulated in microspheres or nanoparticles embedded in the same

hydrogel for delayed release. The timing and sequence of release would depend on the degradation behavior of the hydrogel and the encapsulated carrier, which can be tuned to match the different phases of bone healing for a biomimetic approach. Additionally, future studies should focus on dose optimization for the delivery strategy explored in this study, as the biological effects of growth factors are dose-dependent, and any imbalanced concentrations may lead to undesirable side effects.

Moving forward, an in vivo study will be the next step in validating the findings observed in this study. A critical-size calvarial defect in mice or mandibular defects in rabbits offer a well-established model for evaluating scaffold performance in supporting bone formation under physiological conditions. This model can offer a comprehensive analysis of scaffold integration with surrounding tissues, supporting angiogenesis, host response, degradation, and functional bone regeneration. These outcomes will help determine whether the osteogenic and bioactive effects observed in vitro translate to improved bone regeneration outcomes in vivo.

2.7. Conclusion

This study presented a bioengineered approach that offers a promising solution for bone regeneration in non-load-bearing areas affected by critical-size defects and limited bone volume. The combination of SF and BCP produced a bone cement material with favorable mechanical properties and good 3D printability parameters that enabled the fabrication of scaffolds with a macroporous structure and interconnected internal network conducive to osteogenesis. The integration of a hydrogel system inside the scaffolds for localized growth factor delivery created a bioactive environment that improved the biological performance of the scaffold and supported stem cell adhesion, proliferation, and osteogenic differentiation, along with new matrix deposition and mineralization. Notably, functionalization with BMP-2 delivered alone through the hydrogel system significantly enhanced early osteogenic differentiation and new matrix formation,

suggesting an effective method for accelerated bone regeneration. However, when delivered simultaneously with PDGF, it resulted in reduced osteogenic outcome. Overall, this work emphasizes that clinically relevant approaches require careful design and integration of biomaterials, growth factors, and technologies like 3D printing to address the biological and anatomical demands of bone regeneration in dental and maxillofacial surgery. It can also hold a potential adaptation to broader applications in craniofacial and orthopedic bone regeneration.

2.8. Supplementary Figures

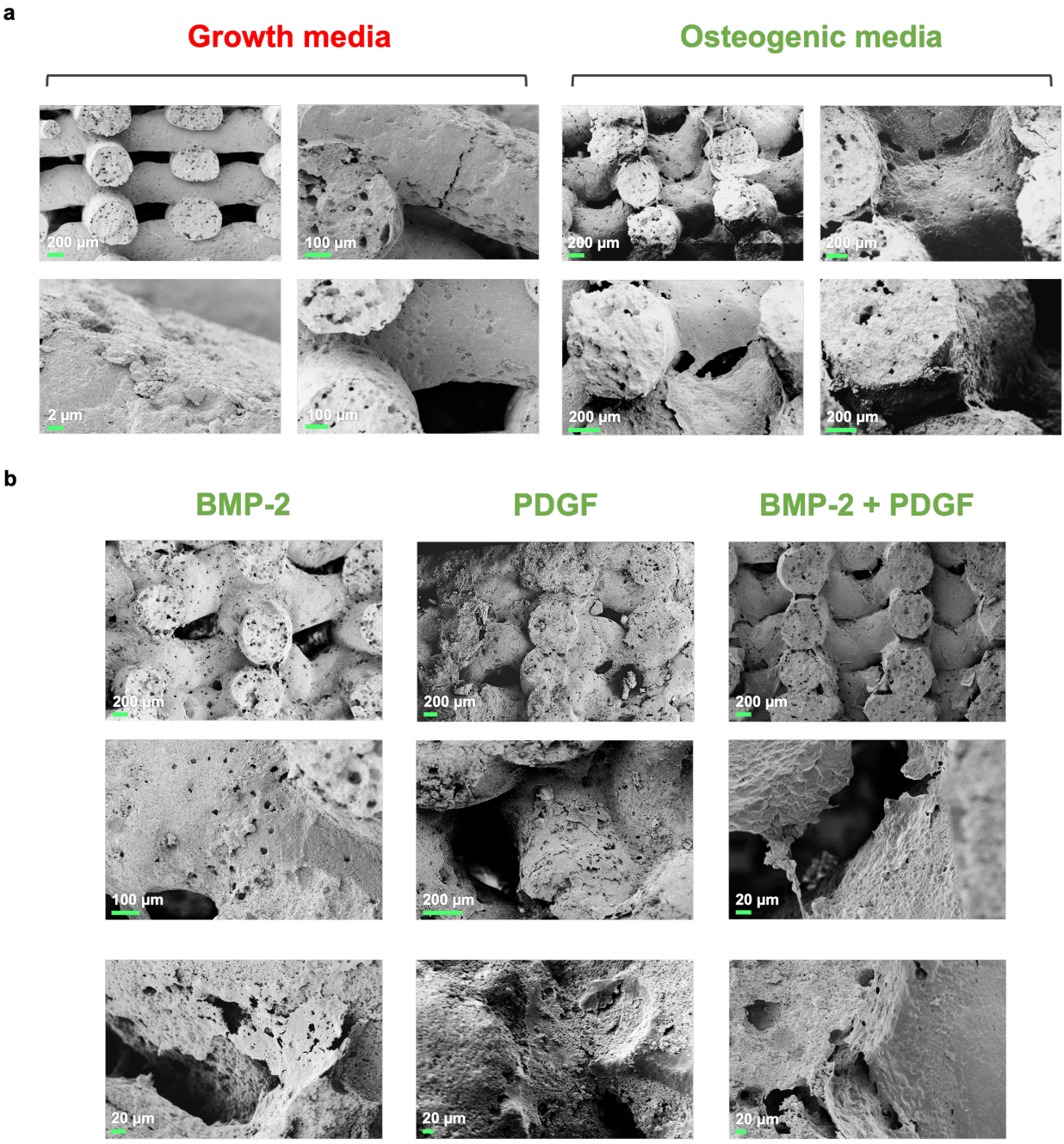

Figure S2-1. SEM images for scaffolds without hydrogel after 7 days of culture with hMSCs in **(a)** GM(left) and OM (right), **(b)** Scaffolds functionalized with the factors (BMP-2, PDGF, or BMP-2 + PDGF) encapsulated within the structure of the printed constructs.

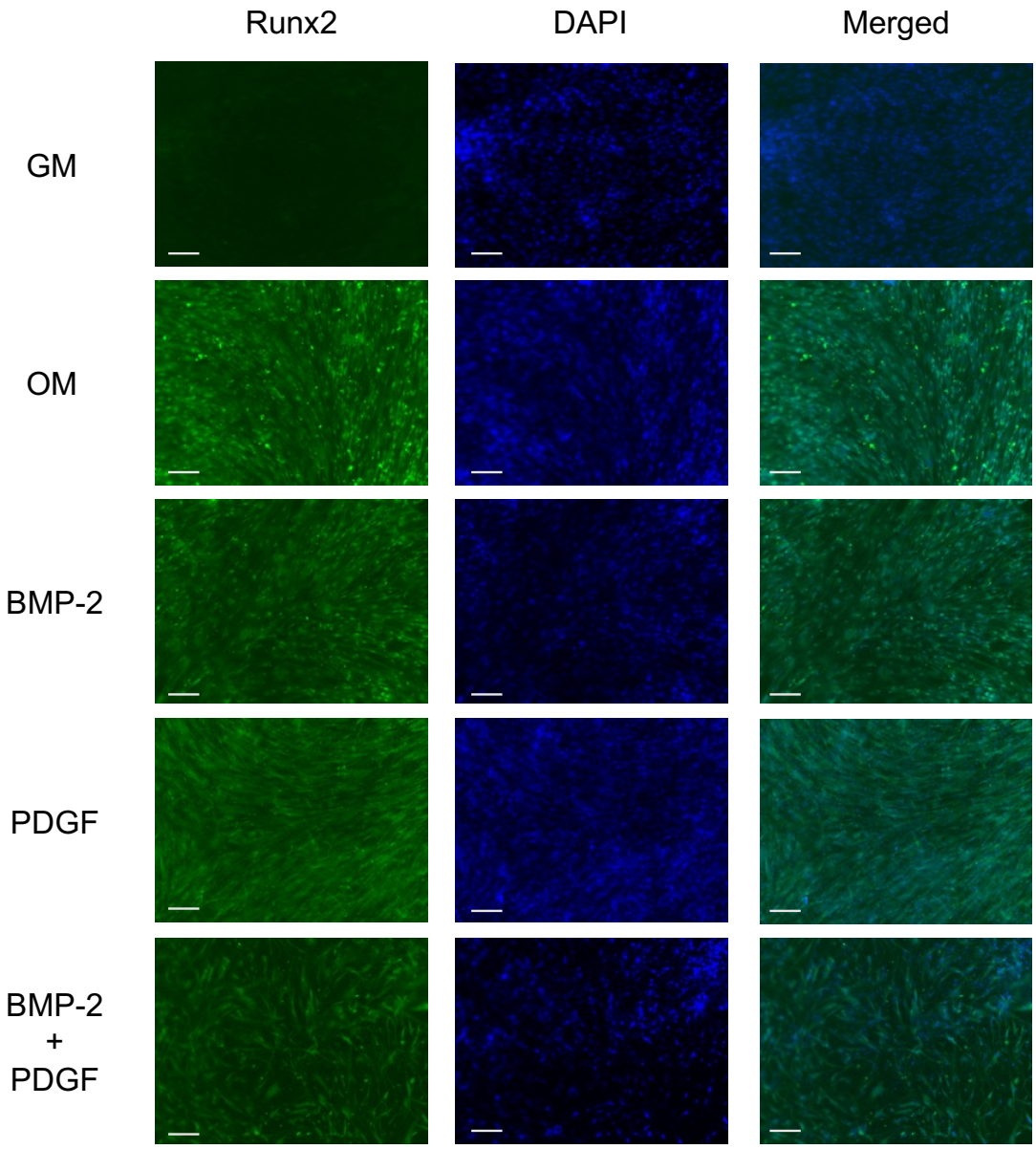

Figure S 2-2. Runx2 immunofluorescence staining of hMSCs on TCPS at day 14. Cells were seeded in a 24-well plate containing scaffolds, and some cells adhered to the bottom surface of the well plate. This experiment was performed to optimize the immunofluorescence protocol and confirm the presence of Runx2 before staining the scaffolds. **Green**: Runx2 expression; **Blue:** nuclei. Scale bar = 100 µm.

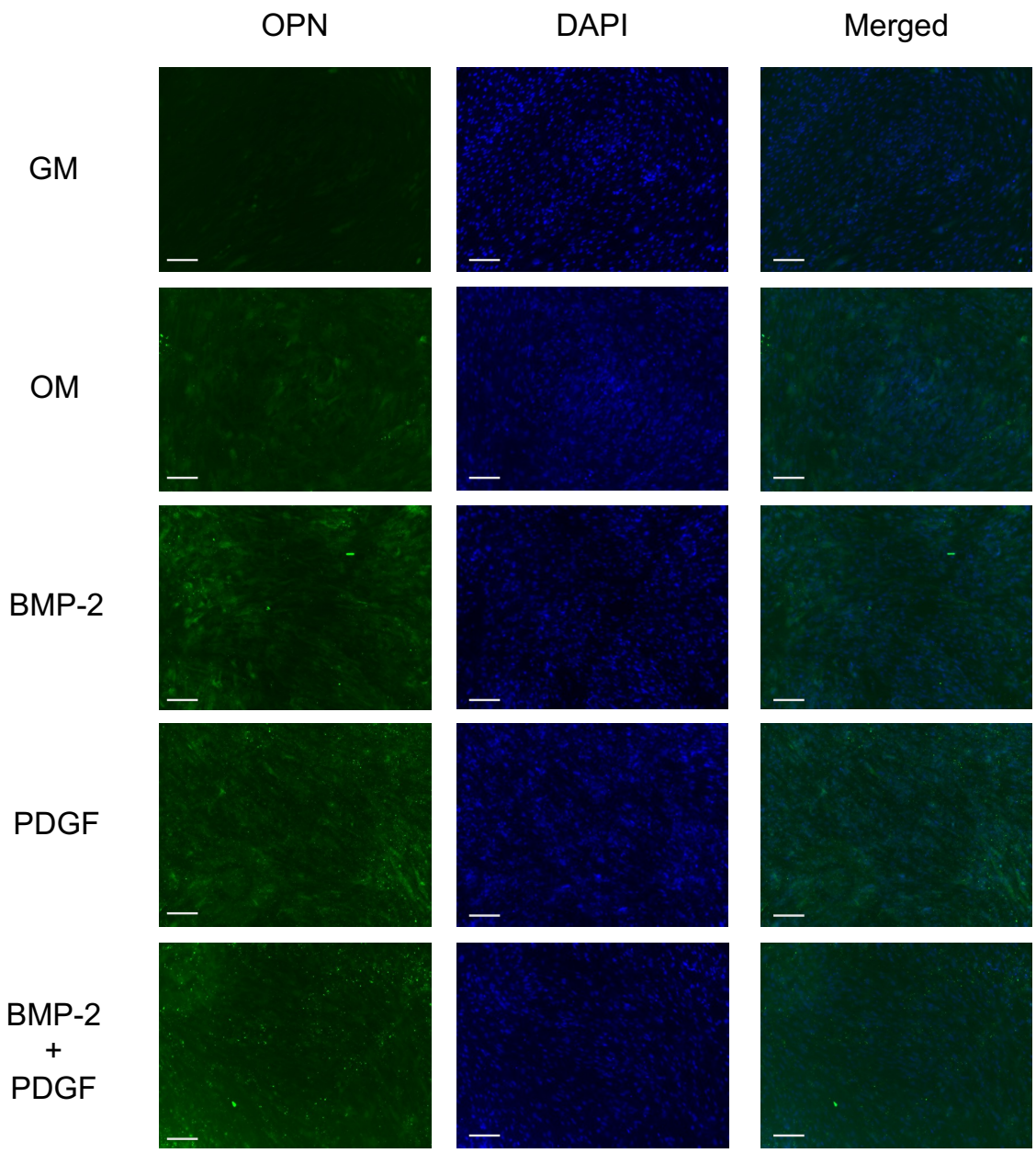

Figure S 2-3. Osteopontin (OPN) immunofluorescence staining of hMSCs on TCPS at day 21. Cells were seeded in a 24-well plate containing scaffolds, and some cells adhered to the bottom surface of the well plate. This experiment was performed to optimize the immunofluorescence protocol and confirm the presence of OPN before staining the scaffolds. **Green**: OPN expression; **Blue:** nuclei. Scale bar = 100 μm.

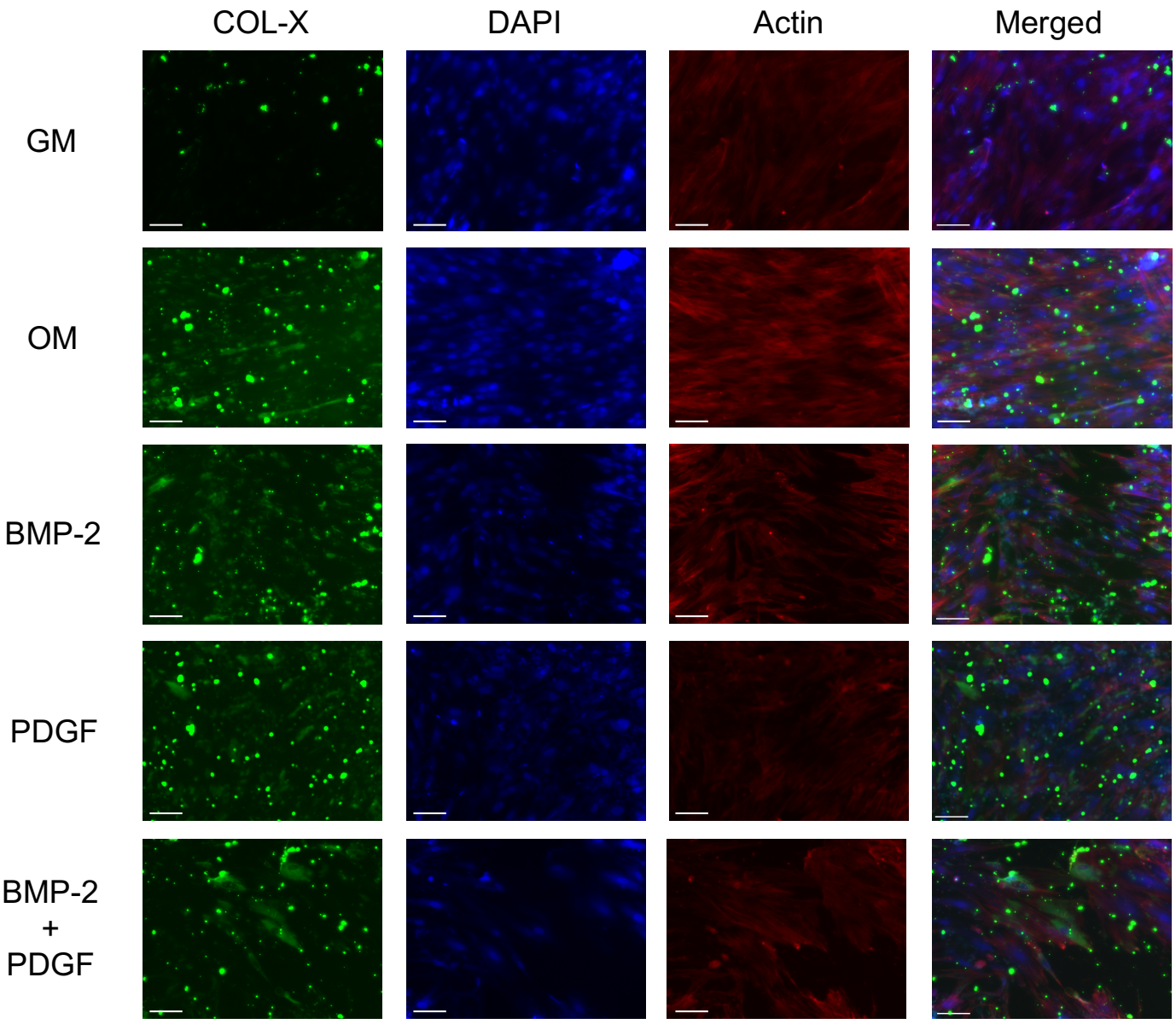

Figure S 2-4. COL-X immunofluorescence staining of hMSCs on TCPS at day 28. Cells were seeded in a 24-well plate containing scaffolds, and some cells adhered to the bottom surface of the well plate. This experiment was performed to optimize the immunofluorescence protocol and confirm the presence of COL-X before staining the scaffolds. **Green**: OPN expression; **Blue:** nuclei; **Red:** Actin. Scale bar = 100 μm.

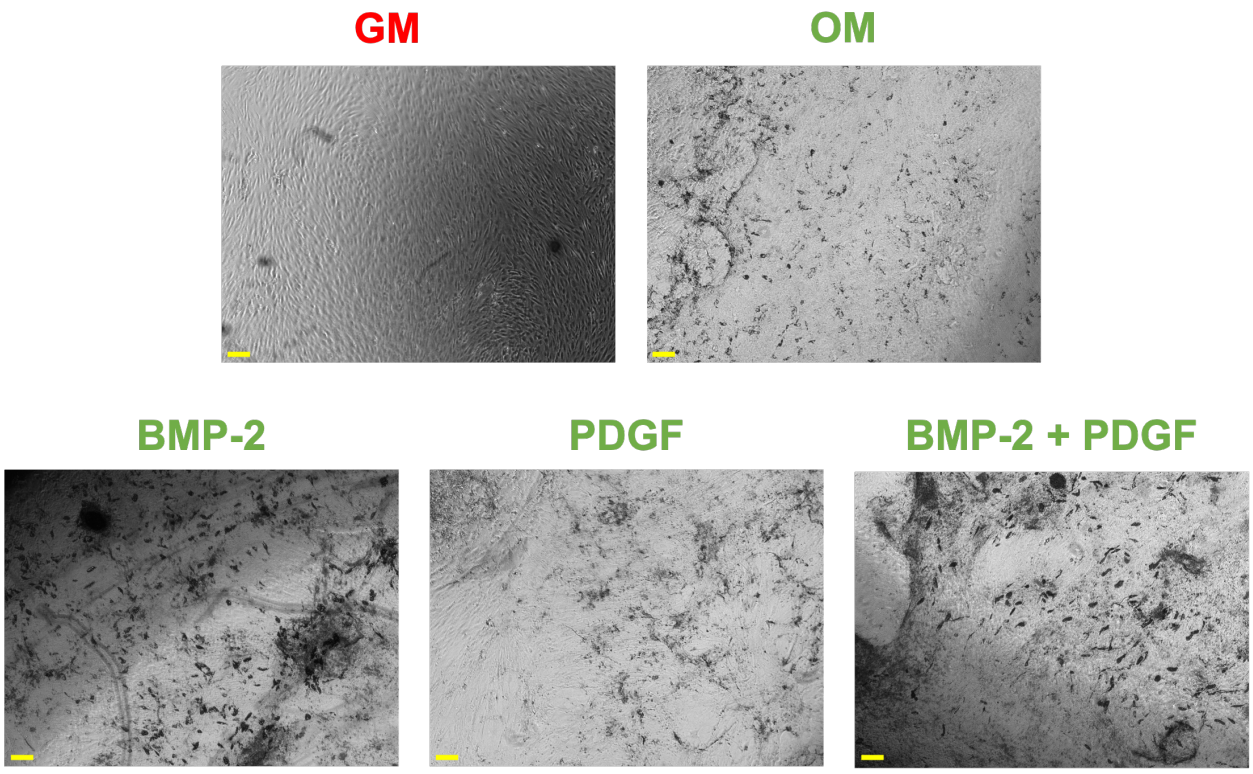

Figure S 2-5. Von Kossa staining of calcium phosphate mineral deposition on tissue culture plates. Representative images show hMSC cultures under various conditions after 21 days. Scaffolds were removed prior to staining, and mineralized matrix deposited on the well bottoms was visualized. Cells maintained in growth media (GM) showed no mineralization, while osteogenic media (OM) induced moderate calcium deposition. BMP-2 supplementation resulted in extensive mineralization, PDGF alone led to moderate mineral deposition, whereas the combination of BMP-2 and PDGF produced notable mineralization. Scale bar = 200 μm.

Chapter 3: Silk-Bioactive Glass 63S Scaffolds for hMSC and HUVEC Co-culture in Bone Regeneration

3.1. Abstract

Objectives: Develop a 3D printable bone cement composed of SF and BG for fabricating scaffolds that support direct co-culture of hMSCs and HUVECs for vascularized bone regeneration.

Methods: A composite ink, SF and BG 63S, was optimized for extrusion-based 3D printing. Material characterization included rheological, printability, and compressive strength assessment. Co-culture conditions were optimized on TCPS by evaluating metabolic activity, early osteogenic differentiation, and gene expression across different cell ratios and media compositions. Selected ratios (4:1 and 1:1 hMSCs:HUVECs ratios in a blend of 1:1 osteogenic and endothelial media) were applied to SF-BG scaffolds, and their biological performance was assessed by Alamar Blue assay, ALP staining, and SEM analysis.

Results: The ink exhibited shear thinning and viscoelastic behavior but required precise formulation for consistent printability. SF improved the mechanical strength of BG 63S. Selected co-culture conditions supported cell viability and early osteogenic response. On scaffolds, co-cultured cells successfully adhered, proliferated, and deposited ECM with morphology influenced by cell ratios. ALP staining revealed faint activity suggestive of early osteogenic differentiation; however, interpretation was limited by suboptimal experimental conditions.

Conclusion: Despite printability challenges, the material was able to form scaffolds that supported the co-culture of hMSCs and HUVECs and showed a potential bioactive platform for in vitro vascularized bone regeneration.

3.2. Introduction

Achieving successful bone regeneration requires materials that combine mechanical stability with biological capacity to stimulate bone tissue formation. Bioactive glass was among the first synthetic materials to bond directly with bone and stimulate osteogenic response.[151] It was developed by Larry Hench in 1969 with the goal of creating a material that is not rejected by the body and can integrate with bone tissue without inducing fibrous encapsulation after implantation.[152] Bioactive glass is a silicate-based material composed primarily of SiO_2, CaO, Na_2O, and P_2O_5, with varying ratios of these network-forming and network-modifying ions depending on the formulation.[151, 153]

The original and most studied composition is called 45S5 Bioglass®, which contains 45 wt% SiO_2, 24.5 wt% Na_2O, 24.5 wt% CaO, and 6 wt% P_2O_5.[152] Upon exposure to physiological fluids, the material undergoes controlled surface degradation and ionic exchange, releasing calcium, phosphate, and silicate ions. These ions initiate the formation of a silica-rich gel, followed by the deposition of CaP that crystallizes into a hydroxycarbonate apatite (HCA) layer. This layer is chemically and structurally similar to bone mineral and can promote early direct bonding between the material and the collagen fibrils in the surrounding bone tissue. The result is a stable interface at the graft-bone junction that cannot be separated without fracturing the bone.[151, 152, 154] Despite its excellent bioactive properties, 45S5 bioglass® still has several limitations. The amorphous glass network results in a brittle material with poor fracture resistance and low bending strength, making it unsuitable for use in load-bearing applications.[154, 155] It also lacks inherent porosity and is prone to particle aggregation that can hinder cell infiltration and tissue integration.[155] Additionally, the initial burst release of sodium and calcium ions can increase local pH levels and potentially cause a cytotoxic effect, thereby delaying the formation of the HCA layer.[151] Nevertheless, the material has shown clinical effectiveness in non-load-bearing clinical applications. It has been commercialized under the name PerioGlas®, which is a particulate graft

with particle sizes ranging from 90 to 710 μm, and is used for regenerating bone in periodontal and alveolar defects.[154, 155]

Many formulations have been developed over the years by incorporating or substituting different ions to improve the biological and mechanical performance and overcome the limitations of 45S5.[154] Bioactive glass 63S is one formulation of bioactive glass composed of 63 wt% SiO_2, 31 wt% CaO, and 6 wt% P_2O_5.[156] The high silica levels create a more stable network that improves the mechanical properties and slows the degradation rate in a controlled manner compared to the original formulation.[157] In addition, the absence of sodium in the composition improves the biocompatibility of the material by minimizing the pH rise often associated with 45S5 when exposed to body fluids.[157] The 63S formulation has been shown to have osteoconductive and osteostimulative properties. In vitro studies have shown that 63S nanoparticles can support the proliferation of unrestricted somatic stem and their early osteogenic differentiation, as indicated by increased ALP activity.[157] However, like most bioactive glasses, 63S remains a brittle material with poor fracture resistance. Incorporating the material into composite scaffolds with polymers like polycaprolactone (PCL) can improve the mechanical properties and the biocompatibility of the composite.[158] This type of scaffold has been shown to support osteogenic differentiation and mineralization; however, its mechanical strength is still lower than that of cortical bone, which limits its application in load-bearing areas.

Silk is a natural polymer widely used in bone applications due to its biocompatibility and favorable mechanical properties.[85] Unlike synthetic polymers, silk can be processed in aqueous conditions without the need for organic solvents, reducing the risk of cytotoxic effects during the fabrication process.[122] However, in its pure form, SF offers limited osteogenic potential.[88] Thus, the material is often combined with other materials such as bioactive glass to create a bioactive composite that better supports bone regeneration and early integration with the surrounding bone tissue.[70] Freeze-drying is a common method for fabricating scaffolds using this type of composite.[70, 159] One disadvantage of this method is that it often results in irregular pore structure

and limited control over pore size and interconnectivity.[77, 83] In contrast, 3D printing offers the ability to precisely control scaffold geometry and fabricate patient-specific constructs designed with interconnected porosity optimized to support cell infiltration and vascularization.[82, 83] However, bioactive glass can be difficult to print with due to its inherent brittleness, poor mechanical strength, and tendency to aggregate, which can disrupt the homogeneity of the ink. These properties make it challenging to formulate a stable filament for extrusion that can maintain structural integrity during and after printing. Recent work has shown that incorporating small amounts into SF-gelatin-based inks can improve bioactivity without compromising printability and cytocompatibility.[83] In this context, SF can serve as an effective binder for bioactive glass and create a stable ink network suitable for extrusion-based 3D printing.[83]

Bone is a complex, multi-tissue organ composed of a mineralized matrix, a vascular network, innervation, and marrow components. Effective regeneration, therefore, requires coordinated activity of multiple cells of osteogenic and endothelial lineage.[129, 160] In tissue engineering, growth factors are commonly used to provide biological cues for cells and to promote regeneration; however, their high cost and potential side effects can hinder their widespread clinical use.[161] Co-culture is a cell-based strategy that involves culturing different types of cells to replicate the complex interplay of signaling pathways involved in tissue regeneration.[161] In the context of bone, co-culturing MSCs with human umbilical vein endothelial cells (HUVECs) has been shown to promote both osteogenesis and angiogenesis.[129, 161] These processes are closely interconnected, as vascularization plays an important role in supplying oxygen, nutrients, and regulatory molecules that support bone formation and remodeling. HUVECs have the ability to produce BMPs, stimulate osteoblastic activity, and secrete vascular endothelial growth factor (VEGF).[162] This, in turn, promotes endothelial cell proliferation, migration, and neovascularization, which facilitates the recruitment of osteoprogenitor cells to the site of the defect. Together, these interactions create a regenerative microenvironment through paracrine signaling that can be an alternative to the direct application of exogenous growth factors.[161-163]

This study aimed to develop a 3D printable bone cement material made of SF and 63S bioactive glass for printing scaffolds designed to support bone regeneration. The first objective was to fine-tune the material for extrusion-based 3D printing and evaluate its printability and mechanical performance. The second objective was to establish and optimize a direct co-culture system of hMSCs and HUVECs for seeding onto the printed scaffolds, with the goal of mimicking the cellular interactions involved in native bone healing. The co-culture model was designed to assess the ability of the scaffold to support osteogenic differentiation and promote early bone formation in vitro. We hypothesized that SF-BG 63S scaffolds with direct co-culture of hMSCs and HUVECs would enhance osteogenic outcomes compared to monoculture with hMSCs in vitro.

3.3. Materials and Methods

3.3.1. Scaffold Fabrication and Characterization.

3.3.1.1. Fabrication of silk-BG scaffolds. The SF-BG bone cement composite was developed by combining a concentrated silk solution with BG 63S to obtain a paste-like consistency suitable for extrusion in 3D printing. First, silk was processed as previously described.[122] The final solution concentration was ~21%. To prepare the printing ink, BG 63S powder (915076, Sigma) was first dissolved in diH_2O, followed by the incorporation of the concentrated SF solution. Two connected 5 mL syringes were used to mix the components together. The final liquid-to-powder ratio was optimized at 0.8:1 (v/w). The final material was loaded into a syringe with 22 Ga 1/2-inch blunt needle (McMaster Carr) and then placed into a homemade extrusion-based 3D printer. Cylindrical scaffolds measuring 11 mm in diameter and 2.5 mm in height were printed with 30% infill. The printed scaffolds were allowed to dry in a humid environment in a 37 °C incubator overnight.

3.3.1.2. Mechanical testing. Uniaxial compression testing was performed on SF-BG cylindrical specimens using an Instron 3366 machine by following the testing protocol outlined in ASTM method F451 Standard for acrylic bone cement. Samples were prepared by injecting the material into a metal mold (6 mm diameter and 12 mm height) and allowed to dry overnight in a humidified environment at 37 °C. After 24h, specimens were demolded and stored at room temperature for 7 days prior to testing. Control samples were prepared without the inclusion of silk, while maintaining the same liquid-to-powder ratio (v/w). Mechanical testing was conducted under both dry and wet conditions. For the wet condition, specimens were pre-soaked in PBS for 24h. Compression testing was performed using a 1 kN load cell at a crosshead speed of 20 mm/min.

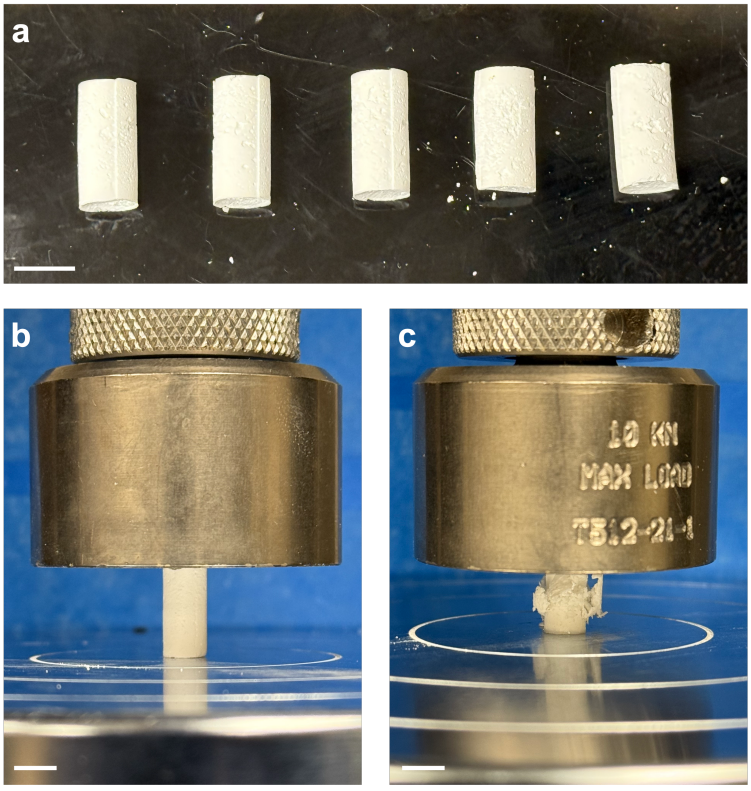

Figure 3-1. Mechanical assessment of SF-BGS bone cement bulk properties. **(a)** Prepared cylindrical samples **(b)**, sample positioned in an Instron machine for compression test, **(c)** compressed sample at the end of the compression test. Scale bar = 6 mm.

3.3.1.3. Rheological measurements and printability. The rheological properties of the SF-BG bone cement ink were assessed using a rheometer (TA Instrument, USA) with a 20 mm parallel plate setup and 500 µm measurement gap. Samples tested included the BG-based cement with and without silk, maintaining the same liquid-to-powder ratio (v/w). Viscosity was measured as a function of shear rate that increases from 0.1 to 1000 s^{-1}. Viscoelastic behavior was characterized by an amplitude sweep test at 1 Hz frequency and a frequency sweep test at 1% strain. Temporal stability was assessed by monitoring G' and G" over time under constant 1% strain and 1 Hz frequency. The printability of the SF-BG bone cement was evaluated by calculating the printability index and spreading ratio to assess the ability of the ink to form filaments and pores. Grid structure was printed using 22 Ga 1/2-inch blunt needle with a 30% infill. Microscopic pictures were taken using a Keyence BZ-X700 microscope, and the images obtained were analyzed using ImageJ software (Fiji). The printability index (P) was calculated as $P = L^2 / 16A$, where L represents the pore perimeter, and A is the pore area. The spreading ratio was defined as the filament diameter divided by the nozzle diameter. Values closer to 1 for both indices indicate a higher printing accuracy.

3.3.2. Co-Culture Optimization Study on TCPS.

3.3.2.1. Experimental Design. To determine the optimal cell ratio and media composition for the co-culture of hMSCs and HUVECs, a preliminary optimization study was conducted on TCPS. The evaluation was based on metabolic activity assessed by the Alamar Blue assay and the ALP activity assay. Accordingly, hMSCs and HUVECs were seeded at five different ratios (1:0, 4:1, 1:1, 1:4, 0:1). Two media conditions were initially tested: 4:1 and 1:1 blends of hMSC GM and HUVEC endothelial growth medium (EGM) (See **Table 3-1** for media compositions). After two days of incubation, selected groups were switched to either 4:1 or 1:1 blends of OM and EGM, while others remained in their original GM: EGM conditions. The media was changed every 2–3 days throughout the study period. Cells were cultured in a humidified incubator at 37 °C with 5%

CO_2 before seeding. Passages 3-6 were used for all experiments. Once they reached 90% confluence, the cells were detached using 0.25% trypsin-EDTA solution.

Table 3-1. Media compositions.

Medium	Base Medium	Supplements	Final Concentration
Growth Medium	DMEM high glucose + GLUTAMAX (Gibco)	Fetal bovine serum (Gibco)	10%
		Antibiotic–Antimycotic (Gibco)	1%
		Non-essential amino acids (Gibco)	1%
		Basic fibroblast growth factor (Gibco)	5 ng/mL
Osteogenic Medium	DMEM high glucose + GLUTAMAX (Gibco)	Fetal bovine serum (Gibco)	10%
		Ascorbic acid	50 µg/mL
		β-Glycerophosphate (Sigma)	10 mM
		Dexamethasone (Sigma)	100 nM
		Antibiotic–Antimycotic (Gibco)	1%
Endothelial Growth Medium	Vascular cell basal medium (ATCC)	Fetal bovine serum (ATCC)	2%
		rhVEGF (ATCC)	5 ng/mL
		rhEGF (ATCC)	5 ng/mL
		rhFGF basic (ATCC)	5 ng/mL
		rhIGF-1 (ATCC)	15 ng/mL
		L-glutamine (ATCC)	10 mM
		Heparin sulfate (ATCC)	0.75 U/mL
		Hydrocortisone (ATCC)	1 µg/mL
		Ascorbic acid (ATCC)	50 µg/mL
		Antibiotic–Antimycotic (Gibco)	1%

3.3.2.2. Metabolic Activity Assessment. An Alamar Blue assay was used to assess the metabolic activity on days 3 and 7. At each time point, a working solution consisting of 10% (v/v) Alamar Blue reagent in the corresponding culture medium was prepared and added to each sample in 24-well plates (1 mL per well). Cells were incubated for 3 hours at 37 °C, and fluorescence was measured immediately using a microplate reader at 560 nm excitation and 590 nm emission. All measurements were performed in replicates.

3.3.2.3. ALP activity Quantification. Osteogenic differentiation was assessed after 21 days of culture using a colorimetric ALP Assay Kit (Abcam). Cells were lysed with 0.1% Triton X-100 in PBS and then sonicated for 5 seconds. Analysis was carried out using a colorimetric ALP assay (Abcam) at 405 nm. A standard curve was used to calculate enzyme activity, and ALP values were normalized to total protein content measured using the Pierce BCA protein assay kit (Thermo Fisher) at 562 nm.

3.3.2.4. Osteogenic Gene Expression. Gene expression analysis was performed on day 7 to evaluate osteogenic differentiation by quantifying the expression of Runx2 and OPN. Total RNA was extracted using the RNeasy Mini Kit (QIAGEN) and treated with DNase (TURBO DNA-free Kit, Invitrogen) to remove genomic DNA contamination. RNA concentration and purity were measured using a NanoDrop™ spectrophotometer (Thermo Scientific). cDNA was synthesized from 600 ng of total RNA using the Transcriptor First Strand CDNA Synthesis Kit (Roche) in a 20 µL reaction. Quantitative PCR was conducted using a CFX96 Real-Time PCR system (Bio-Rad) and SYBR Green I Master Mix (Roche). The cycling protocol included denaturation at 95 °C and 50 cycles of amplification with annealing at 60 °C. Relative gene expression was normalized to the housekeeping gene GAPDH and calculated using the $\Delta\Delta$Ct method. Primary sequences are listed in **Table 3-2**.

Table 3-2. Primers used for Real-Time quantitative PCR.

Primer	Sequence	Tm (°C)
GAPDH	F - ACCCAGAAGACTGTGGATGG R - CAGTGAGCTTCCCGTTCAG	60
Runx2	F - ATGCTTCATTCGCCTCAC R - ACTGCTTGCAGCCTTAAAT	60
OPN	F- ATGAGAGCCCTCACACTCCTCG R- GTCAGCCAACTCGTCACAGTCC	60
BSP	F- ATGGCCTGTGCTTTCTCAATG R- GGATAAAAGTAGGCATGCTTG	60

3.3.3. Biological Evaluation of SF-BG Scaffolds

3.3.3.1. Cell Seeding. Scaffolds were seeded with either hMSCs, HUVECs, or a co-culture of both, using a selected ratio of 4:1 and 1:1. All co-culture conditions were maintained in a 1:1 blend of the two media types. A total of 400 × 10^3 cells were seeded for each well with scaffolds. For TCPS control, the seeding density was 10 x 10^5. Cells were applied directly to the scaffold surface and then incubated in a 37 °C incubator with 5% CO_2.

3.3.3.2. Metabolic activity. Cell proliferation on the 3D scaffolds was assessed using the Alamar Blue assay, as previously described. Conditions included monocultures on scaffolds with either hMSCs or HUVECs, as well as the selected co-culture conditions.

3.3.3.3. Osteogenic differentiation. To assess early osteogenic differentiation**,** ALP staining and an activity assay were performed after 21 days of culture. Staining was carried out using SIGMAFAST BCIP/NBT tablets (Sigma), which produce a black-purple precipitate in the presence of ALP. Quantification assessment of ALP activity in the seeded scaffold was carried out as previously described in the optimization study.

3.3.3.4. Microscopy. To visualize the interior of SF-BG scaffolds and cell growth, SEM analysis was carried out. Samples were fixed with 4% paraformaldehyde for 20 minutes, then dehydrated through a series of ethanol washes, followed by a final wash with HDMS (Sigma). After dying overnight, the scaffolds were gold-sputter-coated and imaged using a Zeiss EVO10 SEM.

3.3.4. Statistical analysis. Data analysis was performed using SPSS version 25 (IBM Corp). One-way ANOVA, two-way ANOVA, and Welch's tests were applied based on data distribution and variance homogeneity. For post hoc comparisons, the Tukey HSD test was used. Statistical significance was set at $p < 0.05$, with significance levels indicated on graphs by the number of asterisks, as follows: *P ≤ 0.05; **P ≤ 0.01; ***P ≤ 0.001; ****P ≤ 0.0001.

3.4. Results and Discussion

3.4.1. Material characterization: Mechanical Assessment and Printability

Compressive testing revealed that the inclusion of silk can improve the mechanical performance of the BG 63S. In dry conditions, the SF-BG samples exhibited a compressive strength of 2 ± 0.53 MPa and a modulus of 38.70 ± 11.20 MPa. In wet conditions, the compressive strength decreased to 0.23 ± 0.03 MPa, and the modulus dropped to 6.40 ± 0.09 MPa (**Figure 3-2**), which is in the lower range of the reported values for trabecular bone.[127] These results confirm the reinforcing effect of SF in the composite matrix ($p < 000.1$). Despite the drop in mechanical properties under wet conditions, the values remained sufficient for non-load-bearing bone applications.

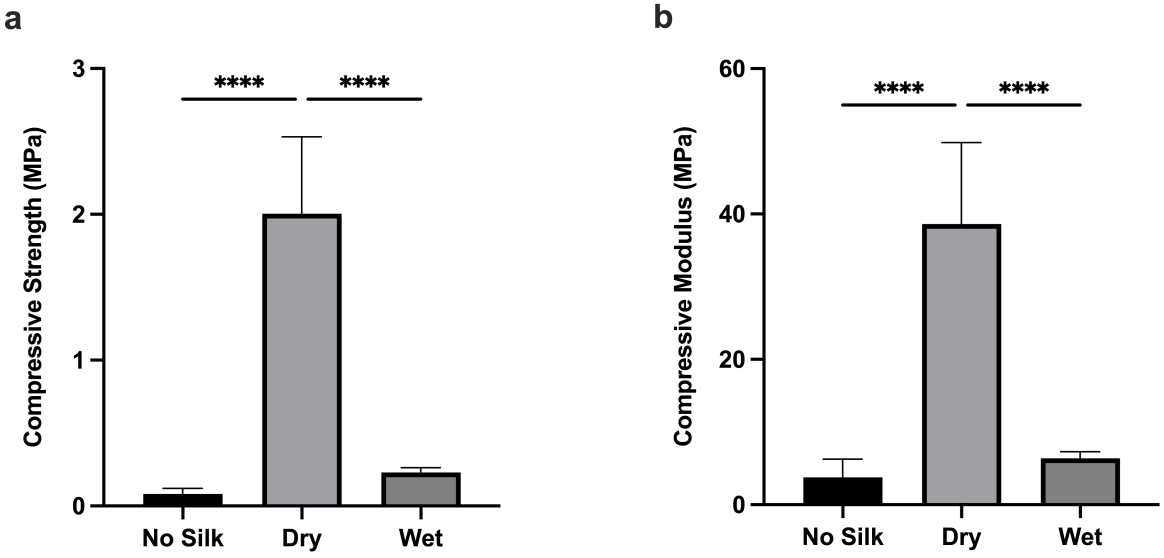

Figure 3-2. Mechanical performance of SF-BG 63S bone cement under compression. (a) compressive strength and **(b)** modulus of cylindrical specimens. Data are presented as mean and ±SD. Asterisks indicate statistically significant difference (****$p < 0.0001$).

Rheological analysis was conducted to understand the printability behavior of the developed SF-BG 63S ink and its ability to maintain shape fidelity after extrusion. The flow behavior of the ink showed a gradual decrease in viscosity with increasing shear rate (**Figure 3-3**a1). This shear-thinning behavior is essential for extrusion-based printing, as it allows the ink to flow smoothly through the nozzle. The amplitude sweep test aimed to evaluate the structural stability of the ink under increasing strain. The storage modulus G' remained higher than the loss modulus G" up to around 3% strain before crossing over at the yield point (**Figure 3-3**a2). This early structural breakdown suggests that while the ink can maintain its structural stability under low strain, it begins to deform under moderate shear, resulting in the loss of its structural network. Such behavior may impact printability, as maintaining the shape of filaments during extrusion depends on the ability of the ink to withstand shear forces without premature breakdown.[79, 81] This may pose challenges during printing, as higher shear forces may disrupt the homogeneity of the material and can potentially lead to phase separation and unreliable printing. Nevertheless, the material exhibited a viscoelastic region before yielding, which is a fundamental property necessary for extrusion-based printing. However, the behavior was not exactly linear, with an initial slight increase in both moduli, followed by a decline towards the yield point.

In frequency sweep analysis, the material maintained a viscoelastic behavior under 1% strain, with G' dominating G" across the tested frequency range. The minor fluctuation observed at high frequency is attributed to structural rearrangement at the beginning of the test. The instability observed toward the end of the test was likely a result of sample drying, which affected the accuracy of the measurements at the end of the test (**Figure 3-3**a3). However, the material exhibited acceptable behavior essential for structural stability during a dynamic process like 3D printing. In addition, the temporal stability of the ink was assessed under constant strain and frequency over time. Throughout the 10-minute testing duration, the G' maintained consistently higher than G", retaining a viscoelastic behavior over time (**Figure 3-3**a4). This stability is

important for 3D printing, as it indicates that the ink can maintain its structural integrity through a prolonged printing period without significant collapse.

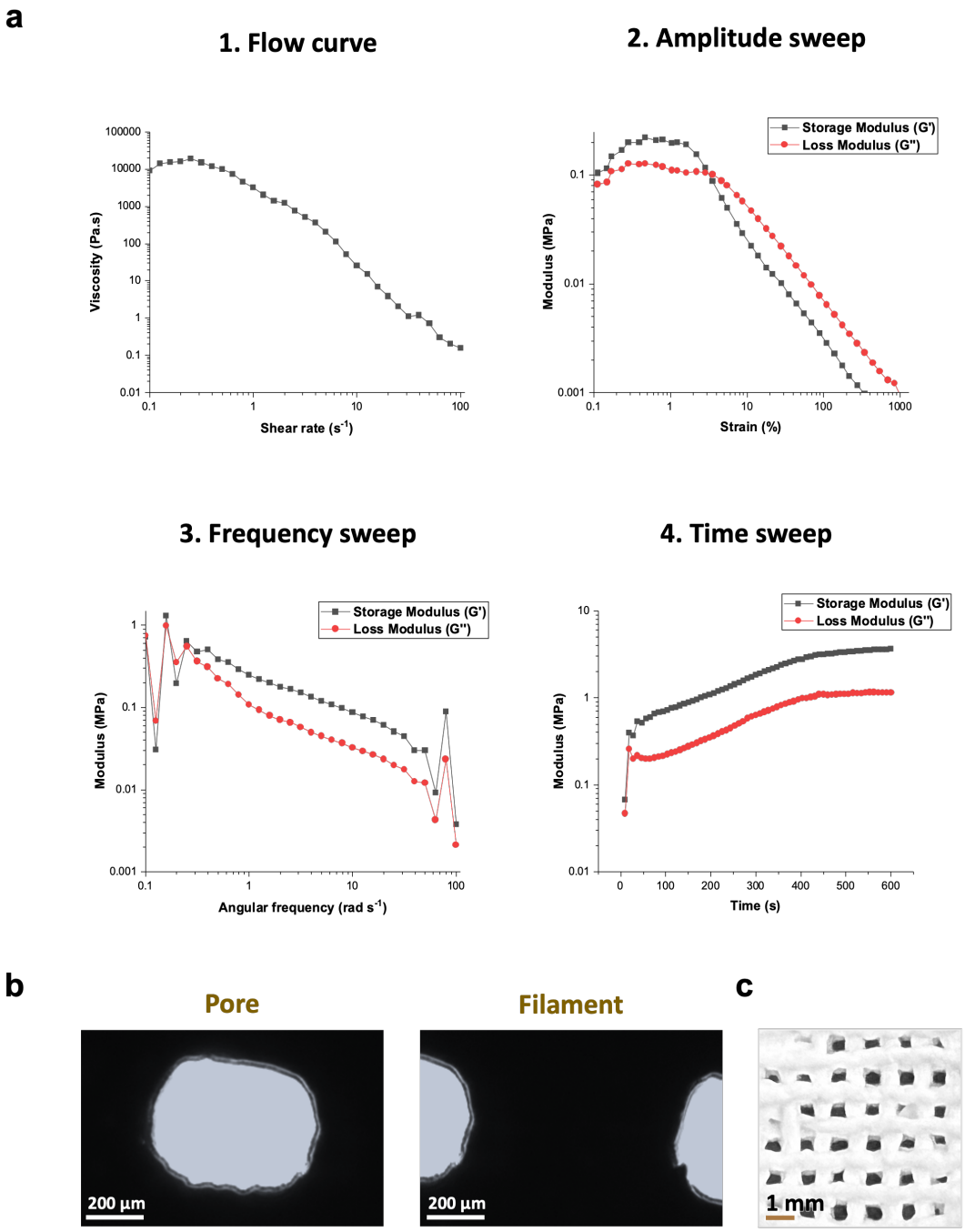

Figure 3-3. Printability assessment of SF-BG 63S composite ink. (a) Rheological characterization to predict printability includes flow behavior, amplitude sweep, frequency sweep, and time sweep. **(b)** Microscopic images show the pore configuration and extruded filament. **(c)** Top view of a printed SF-BG 63S grid structure.

Finally, quantitative analysis of printability revealed a printability index of 1.82 ± 0.11 and a spreading ratio of 1.11 ± 0.13. While values closer to 1 indicate higher printing accuracy, the observed results still reflected acceptable printing accuracy. The printed constructs maintained their porosity throughout the structure of the scaffolds, but exhibited a more rounded configuration rather than square geometry. Most importantly, these deviations did not negatively affect the osteogenic features of the scaffolds required for bone regeneration (**Figure 3-3**b,c).

The SF-BG 63S bone cement was used to print scaffolds using an extrusion-based 3D printer. The material was able to extrude through the nozzle and produce filaments that can be stacked and form cylindrical scaffolds with an interconnected macroporous structure. Two designs were printed: one with 14 mm diameter x 2.5 mm height and a solid outer shell, and another with 11 mm diameter x 2.5 mm height and a porous outer shell, both with 30% grid fill (**Error! Reference source not found.**). Extruded filaments had diameters greater than 400 μm, and pores formed an irregular square morphology with sizes exceeding 500 μm. At higher magnification, the surface of the filaments exhibited microroughness along their surface (**Figure 3-5**). This design supports osteogenesis by fulfilling the requirements necessary for cell adhesion, infiltration, and capillary invasion.[72]

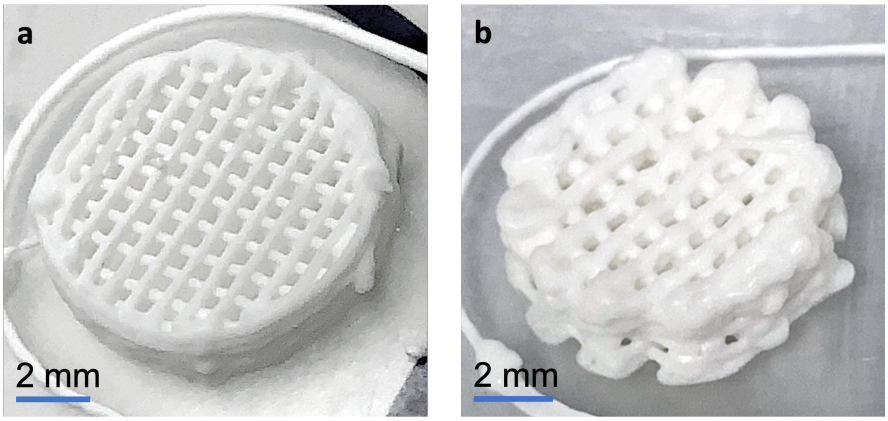

Figure 3-4. 3D printed SF-BG 63S scaffolds with different exterior surface designs**. (a)** Scaffold with a solid exterior (14 x 2.5 mm) and **(b)** scaffold with a porous exterior (11 x 2.5 mm).

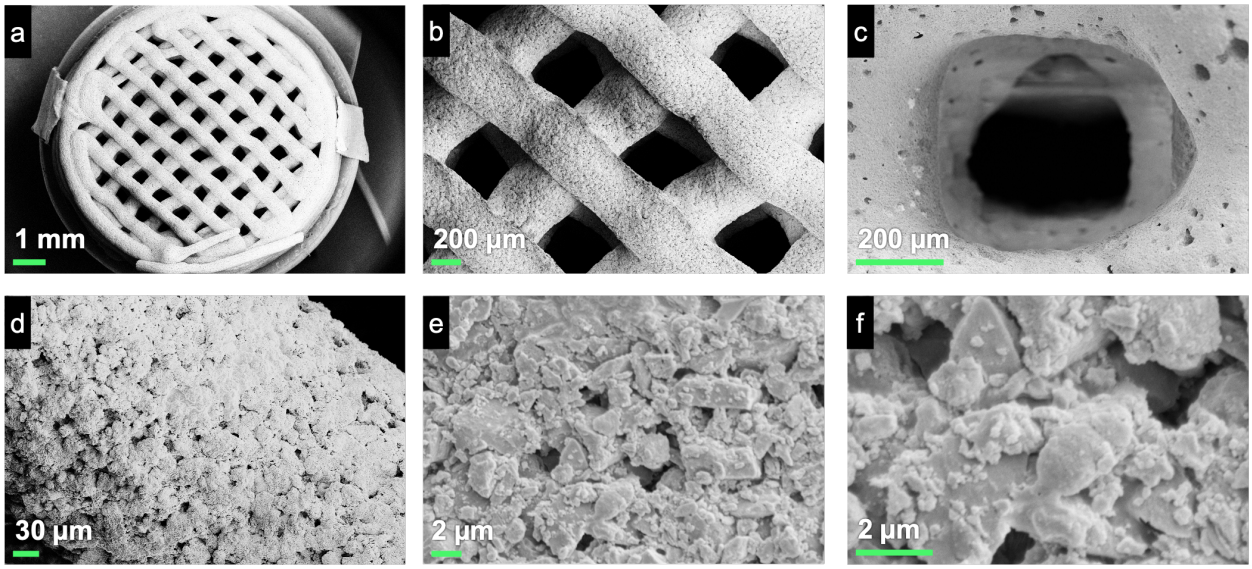

Figure 3-5. SEM images of 3D printed SF-BG 63S scaffolds. **(a)** Top view of the scaffold showing grid structure. **(b)** Stacked filaments with pore interconnectivity, **(c)** pore. (**d-e)** Filament microporosity and surface roughness. **(f)** High-magnification image showing BG 63S particles within the SF matrix.

However, the printing process was sensitive and inconsistent. Small variations in the liquid-to-solid ratio had a notable impact on the consistency and printing behavior of the ink, which required highly precise control over mixing. Several challenges were encountered during the preparation of the ink. The BG particles were difficult to incorporate uniformly, and the limited DiH_2O volume required the early incorporation of SF solution to achieve proper mixing. Moreover, even minor increases in liquid content caused the ink to lose its structure and become more fluid, making it unable to form filaments that can be stacked to form a structure.

3.4.2. Co-culture Determination

The optimization study aimed to determine the most effective co-culture conditions for hMSCs and HUVECs for osteogenesis on TCPS, with the ultimate goal of applying these conditions to the developed SF-BG 63S scaffolds. Five different cell ratios (1:0, 4:1, 1:1, 4:1, 0:1) were evaluated under various media compositions, including GM, OM, and EGM controls, as well as two OM:EGM compositions (4:1 and 1:1). An Alamar blue assay was performed at days 3 and 7 to assess cell proliferation, followed by ALP activity on day 21 and gene expression of Runx2, and OPN on day 7 to assess osteogenic differentiation. GM and EGM groups were included as test controls and not used for co-culture selection, while OM served as the baseline comparison.

Alamar Blue results demonstrated an increasing trend in cell proliferation across all groups from day 3 to day 7. Among the co-culture conditions, the 1:4 hMSC:HUVEC ratio cultured in OM:EGM (1:1) media exhibited the highest fluorescence intensity at both time points. This was followed by the 1:1 and 4:1 ratios in the same media condition, which also showed elevated proliferation levels compared to hMSC (1:0) and HUVEC (0:1) monoculture controls (**Figure 3-6**).

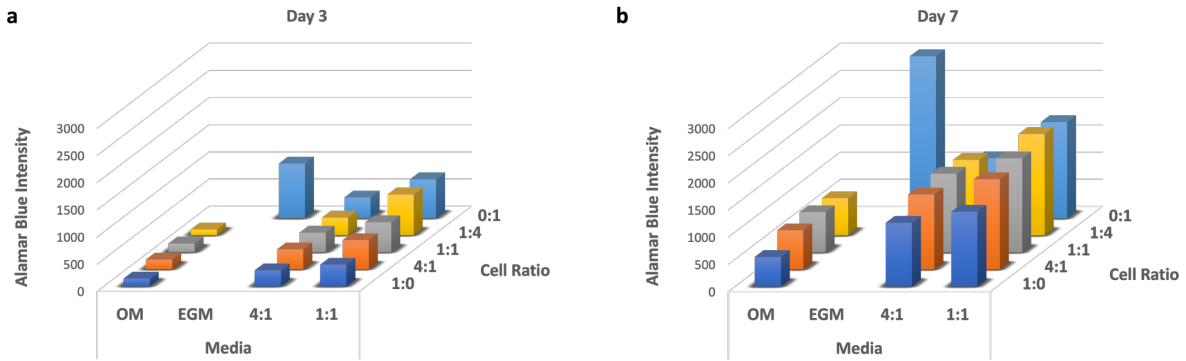

Figure 3-6. Alamar Blue assay (n = 3) showing metabolic activity on days (a) 3 and (b) 7 during co-culture optimization in TCPS. Conditions included different mono- and co-cultures with various cell ratios and media compositions. Data are presented as mean values.

On day 21, ALP activity quantification varied across groups and media conditions (**Figure 3-7**). In OM alone, the 4:1 cell ratio exhibited the highest activity, followed closely by the 1:1 group. The 1:4 group showed lower ALP activity, while the hMSC monoculture in OM maintained a baseline level consistent with its osteogenic nature. When the culture medium included an endothelial component (OM: EGM), the ALP activity increased across all experimental groups compared to those cultured in OM alone. In OM: EGM (4:1), elevated ALP activity was observed in the 1:0, 4:1, and 1:4 groups, although the trend across the cell ratios was less distinct. In contrast, the OM: EGM (1:1) condition showed even higher ALP activity, with the 1:1 cell ratio, demonstrating the highest ALP activity overall, followed by 4:1, 1:4, and 1:0. The increase in ALP activity was consistent across both OM:EGM media conditions, suggesting that the inclusion of endothelial components in the culture medium enhances osteogenic signaling, even though the effect varied by cell ratio.

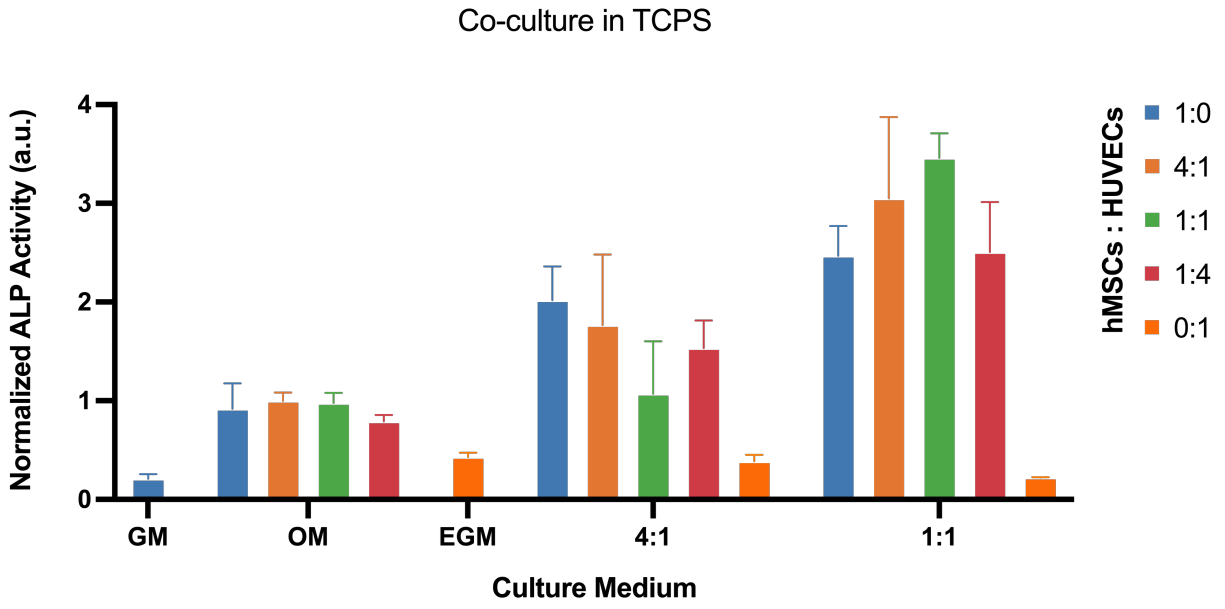

Figure 3-7. Normalized ALP activity quantification (n = 3) on day 21 in TCPS cultures under different mono- and co-culture conditions with various media compositions. Data were normalized to housekeeping genes and are presented as mean ± SD.

Gene expression analysis was conducted on day 7 to evaluate the early response of the co-culture groups by assessing the expression of genes associated with osteogenic differentiation and early bone formation. Runx2 is a key transcription factor that governs the commitment of MSCs to the osteoblastic lineage, driving their proliferation and differentiation, and can serve as an early marker of osteogenesis.[164, 165] On the other hand, OPN is a multifunctional glycoprotein involved in both bone remodeling and angiogenesis.[166, 167] While it is predominantly secreted by osteoblasts, OPN expression has also been observed in endothelial cells under specific conditions, such as growth factor stimulation (e.g., VEGF), metabolic stress, or co-culture with other vascular cells. In tissue repair, it is frequently associated with matrix remodeling and early vascular signaling.[168] Runx2 expression varied among the testing conditions and was influenced not only by the cell-to-cell ratio but also by the balance of osteogenic and endothelial components in the culture medium (**Figure 3-8**a). In OM alone, fold change increased slightly in the 1:1 and 1:0 groups, with more noticeable upregulation in the 1:4 group. Interestingly, the 4:1 group in OM showed downregulation below baseline. In OM: EGM (4:1), Runx2 expression was elevated in the 1:0, 4:1, and 1:1 groups, with minimal expression in the 1:4 group. In OM: EGM (1:1), overall expression was lower than those observed in the 4:1 media condition, with only the 4:1 group exhibiting a fold change above one. The expression of OPN showed a different trend and appeared to correlate more closely with the HUVEC content than with osteogenic conditions (**Figure 3-8**b). In the OM group, expression remained low across all cell ratios, with the 1:0 group showing a slight increase; however, the fold change remains below 1. HUVECs cultured alone in EGM exhibited elevated OPN expression. In OM: EGM (4:1), only the 0:1 group showed a fold change closer to 1, and the expression remained low in the other cell ratios. In contrast, in the OM: EGM (1:1), OPN expression increased in the 1:4 group and was more pronounced in the 0:1 group, which had no hMSCs. The overall trend observed was that OPN expression increased with greater endothelial presence, regardless of the osteogenic components. This may support the interpretation that OPN upregulation in this context likely reflects early endothelial or angiogenic

signaling rather than osteogenic differentiation. This is consistent with the fact that OPN is typically associated with late-stage osteogenic differentiation as a bone matrix protein and may not be upregulated in early time points. Thus, the elevated OPN expression appears to be more closely linked to endothelial activity rather than to osteoblastic differentiation. Although the gene expression results provided a useful insight into the early osteogenic and angiogenic responses of the co-culture system, some results were difficult to interpret in relation to the assays due to differences in measurement time points. While Runx2 is known to initiate osteogenic differentiation and can upregulate the downstream markers such as ALP, direct comparison should be made carefully, given the time gap between gene expression and functional outcomes.[167]

The results of the optimization study should be interpreted with caution, especially the overall low gene expression trend observed. Taken together, the expression of Runx2 and OPN, along with ALP and cell viability data, the 4:1 and 1:1 hMSCs to HUVECs co-culture in OM: EGM (1:1) medium was selected for subsequent experimentation with the SF-BG scaffolds. Given that osteogenic differentiation is the primary outcome of this study, these groups were chosen based on their balanced osteogenic activity and cell viability under the tested conditions.

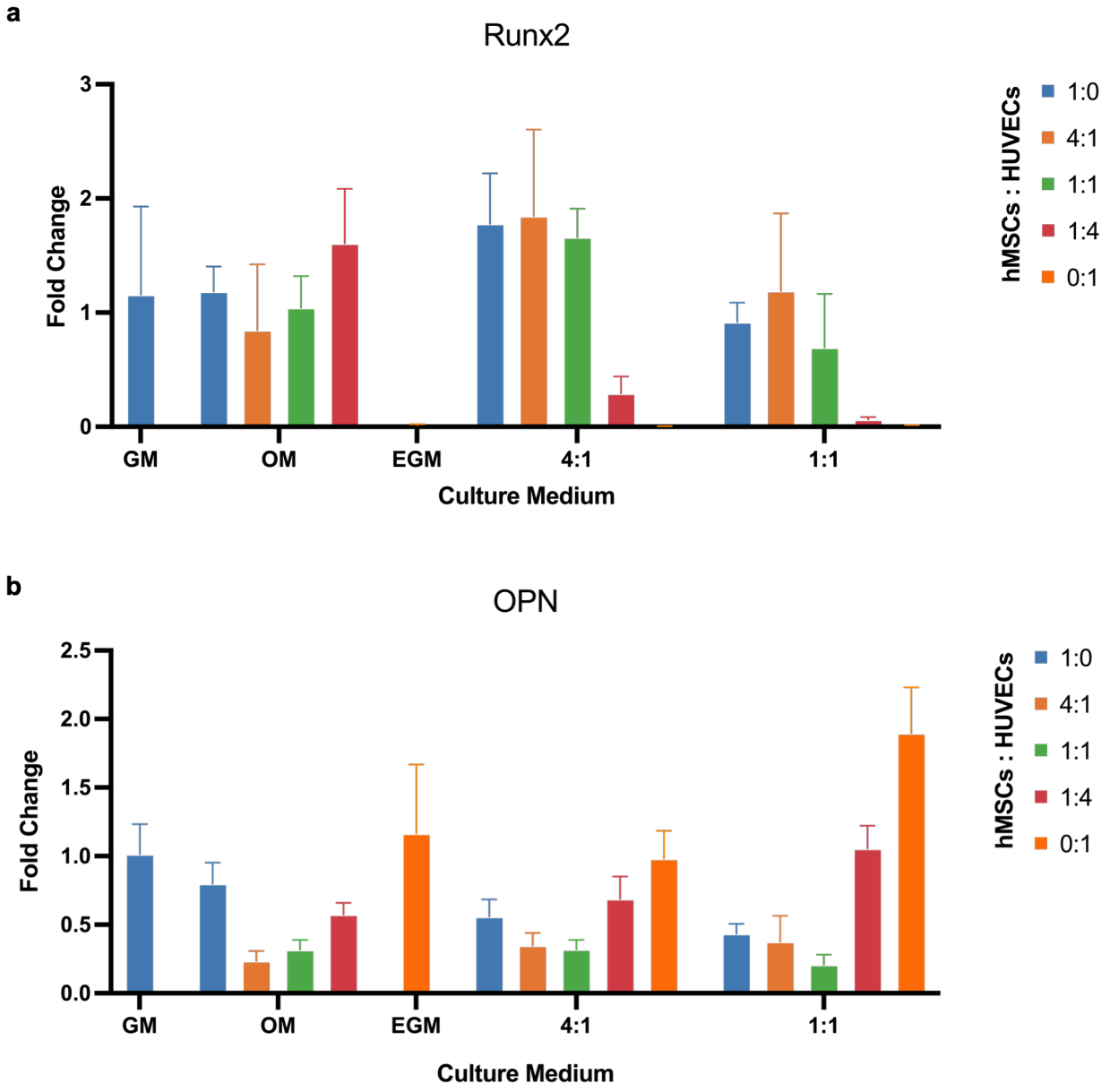

Figure 3-8. Gene expression of **(a)** Runx2 and **(b)** OPN on day 7 in TCPS cultures under different mono- and co-culture conditions with various media compositions. Data were normalized to housekeeping genes and are presented as mean ± SD.

3.4.3. Biological performance of SF-BG scaffolds

The goal of the biological evaluation was to assess the capacity of the developed SF-BG 63S scaffolds to support cellular activity and promote osteogenic differentiation. Given the potential of this bone cement as a bioactive material for scaffold fabrication, the study aimed to evaluate its cytocompatibility and role in guiding early bone formation in vitro using monoculture and co-culture conditions.

3.4.3.1. Testing with monoculture of hMSCs and HUVECs. Monocultures of hMSCs and HUVECs were seeded on SF-BG 63S scaffolds to evaluate their cellular response independently of each other. In hMSC-seeded scaffolds, the cells exhibited early signs of spreading along the filaments and pore walls. Over time, they continued to proliferate and gradually occupied the margins of the pores (**Figure 3-9**). The metabolic activity of the cells was monitored over 35 days using the Alamar Blue assay under both GM and OM conditions. A steady increase in cell viability was observed across the groups, with a more pronounced rise starting on day 14 and continuing to increase up to the final time point, particularly in the scaffolds incubated in OM. Although the assay does not distinguish between proliferation and differentiation, the cell response in vitro reflects a positive response to osteoconductive conditions (**Error! Reference source not found.**). Further, SEM imaging on day 35 showed a positive cellular response on the scaffolds in both GM and OM conditions. In both groups, the cells adhered, proliferated, and formed ECM along the surfaces of the filaments and pore walls. However, in the OM condition, the coverage was more extensive, and the cells exhibited a flattened morphology with visible cellular extensions that anchored to the scaffold and interconnected with neighboring cells, forming a continuous network. This osteoblast-like morphology is typically observed in silk-based scaffolds with differentiated hMSCs (**Figure 3-11**).

In scaffolds seeded with HUVECs, the metabolic activity was monitored over 21 days and showed a moderate but consistent level of activity throughout the observation period. The Alamar

Blue assay showed a gradual increase in metabolism, reaching a peak on day 14, followed by a slight decline to initial levels by day 21 (**Figure *3-12***). Although the observed values here were lower than those observed with hMSCs monoculture, the SEM results after 21 days of HUVECs monoculture indicate that the scaffold provided a cytocompatible environment. The cells adhered and proliferated on the filaments; however, no significant ECM was observed (**Figure *3-13***).

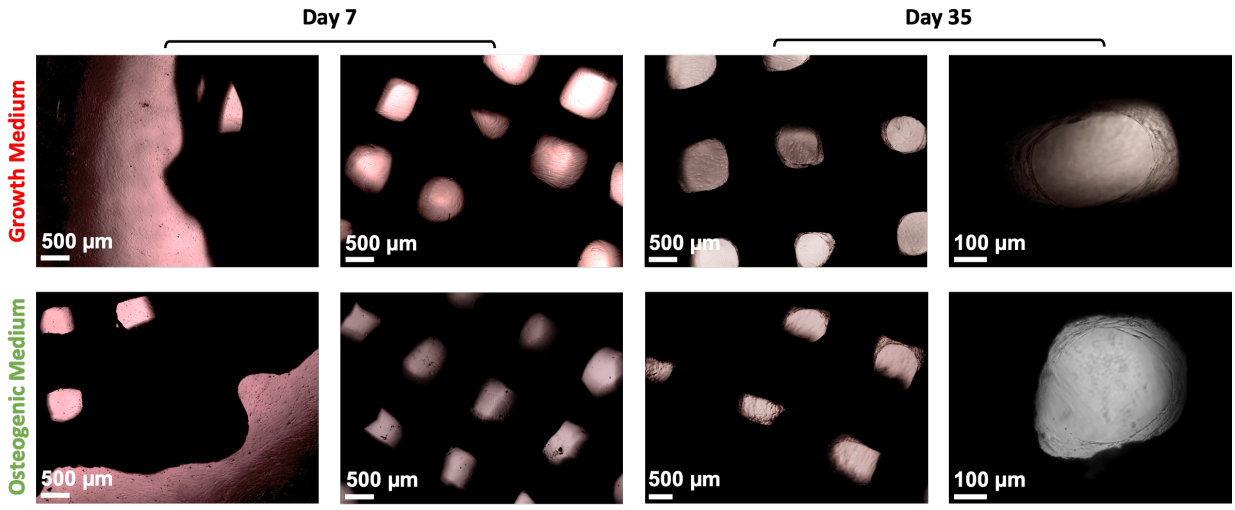

Figure 3-9. Light microscopy images of hMSCs seeded on SF-BG 63S scaffolds after **(a)** 7 and **(b)** 35 days of culture. Images show samples maintained in growth medium and osteogenic medium.

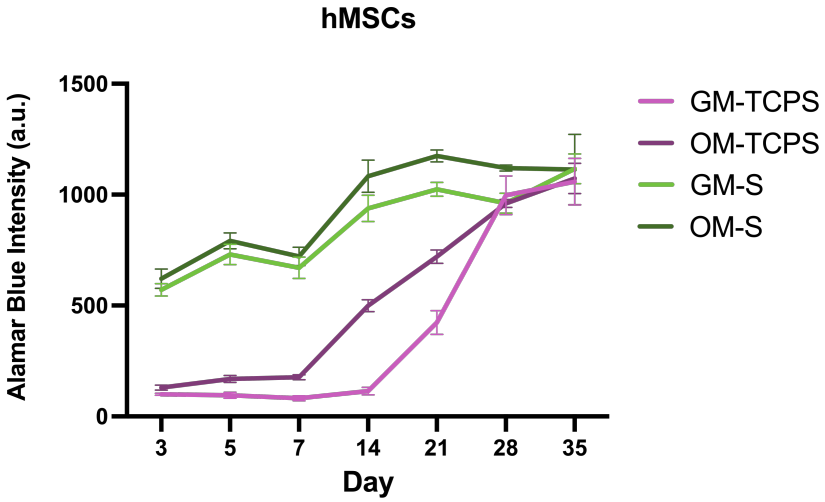

Figure 3-10. Alamar Blue assay (n = 3) showing metabolic activity of hMSCs-seeded SF-BG scaffolds over 35 days. Conditions include tissue culture polystyrene with growth medium (GM-TCPS) and osteogenic medium (OM-TCPS), as well as scaffolds in growth medium (GM-S)

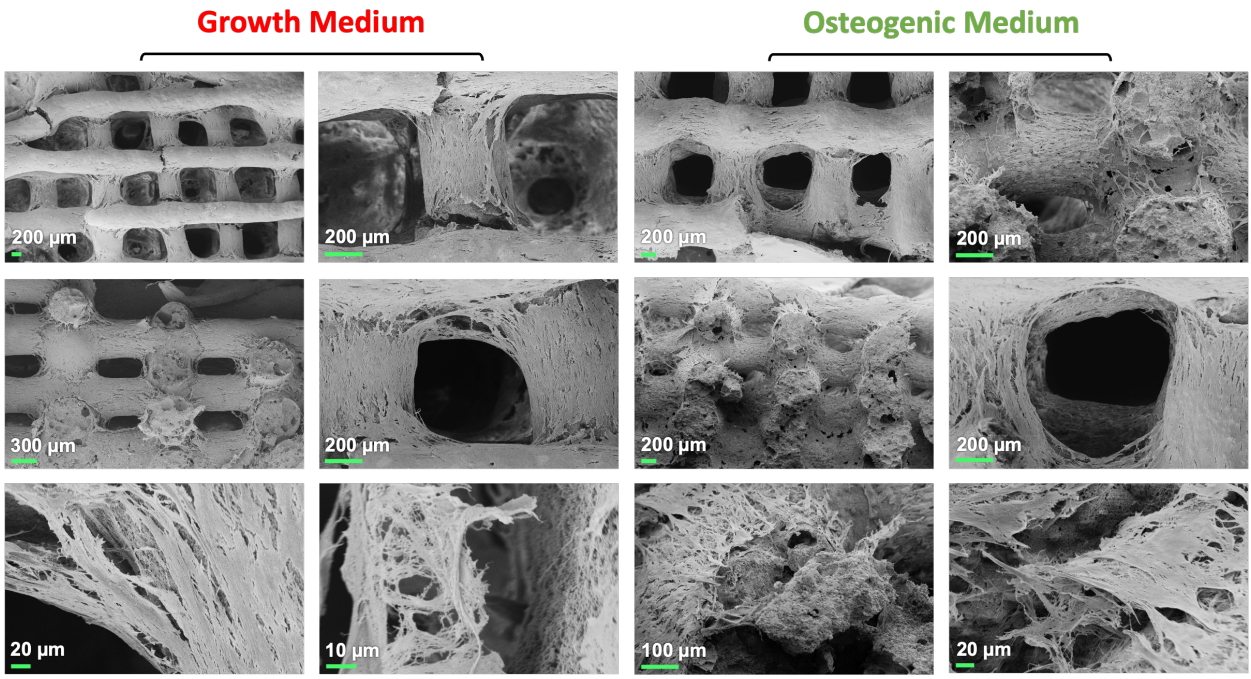

Figure 3-11. SEM images of hMSCs-seeded SF-BG 63S scaffolds on day 35. Conditions include scaffolds in growth medium (left) and osteogenic medium (right).

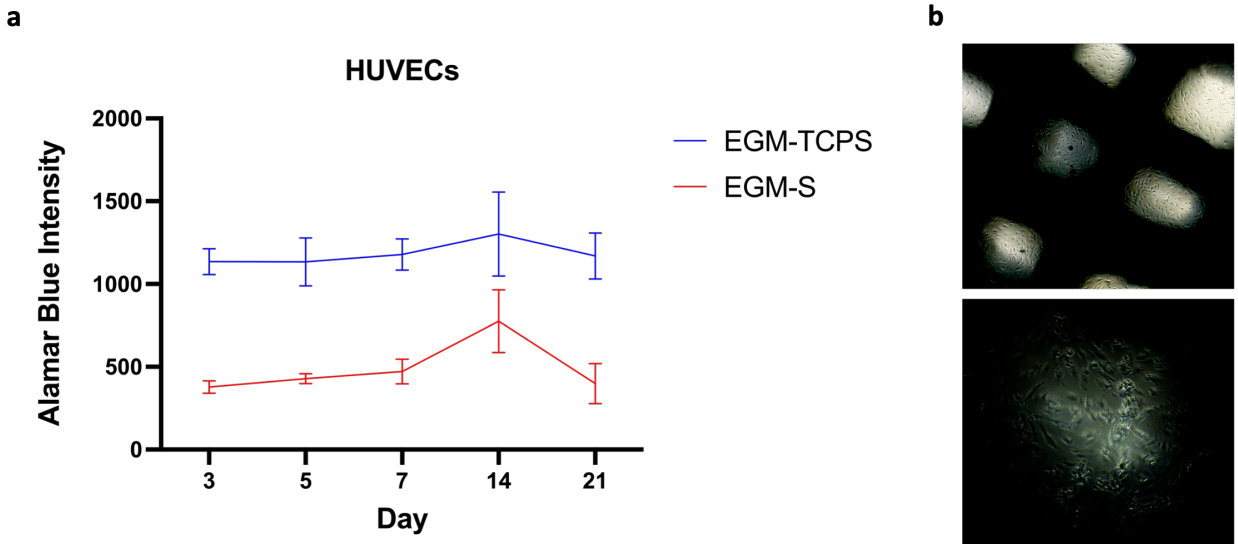

Figure 3-12. (a) Alamar Blue assay (n = 3) showing metabolic activity of HUVECs-seeded SF-BG scaffolds over 21 days. Conditions include TCPS with endothelial growth medium (EGM-TCPS) and scaffolds in EGM (EGM-S). **(b)** Light microscopy images of HUVECs seeded on SF-BG 63S scaffolds and cultured in EGM for 21 days. Data presented as mean and ±SD.

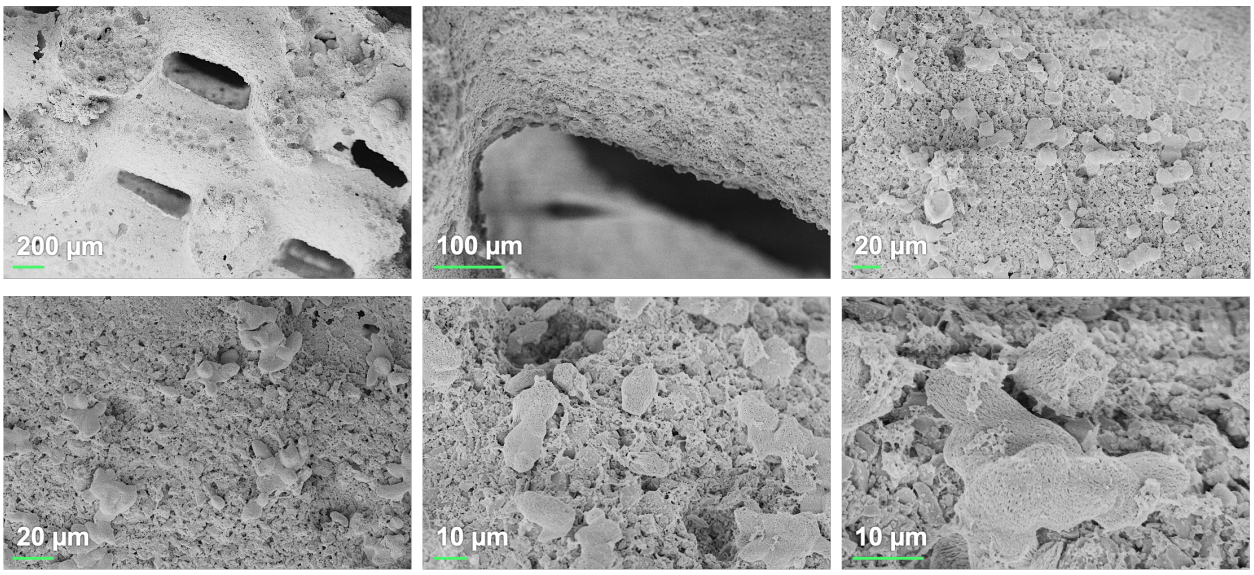

Figure 3-13. SEM images of HUVECs-seeded SF-BG 63S scaffolds on day 35.

3.4.3.2. Testing with hMSCs and HUVECs co-culture. Based on the optimization study, hMSCs and HUVECs were co-cultured on SF-BG 63S scaffolds at cell ratios of 4:1 and 1:1 in a 1:1 media mixture of OM and EGM. Cell viability and metabolic activity were monitored over 21 days using the Alamar Blue assay. All experimental groups showed good metabolic activity throughout the culture period, with a trend of increasing activity over time. The 4:1 co-culture on scaffolds exhibited a sharp increase on day 7, followed by a slight decline, but remained higher than other groups. The 1:1 co-culture on the scaffold showed a gradual and contiguous increase, peaking at day 21. Similar trends were observed in the corresponding TCPS controls. The observed metabolic activity confirms that the SF-BG scaffolds supported cell survival and proliferation under co-culture conditions (**Figure 3-14**).

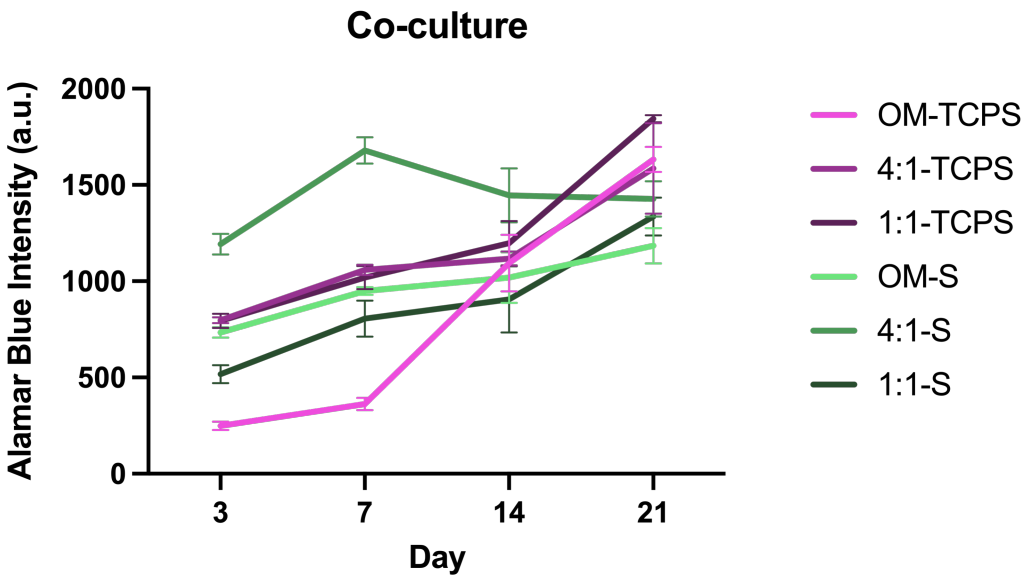

Figure 3-14. Alamar Blue assay (n = 3) showing metabolic activity of co-cultures on SF-BG 63S scaffolds and TCPS over 21 days. Conditions include: **(1)** OM-TCPS – hMSCs cultured in TCPS in OM, **(2)** 4:1-TCPS – co-culture on TCPS in 1:1 mixed medium, **(3)** 1:1-TCPS – co-culture on TCPS in 1:1 mixed medium, **(4)** OM-S – hMSCs on scaffolds in OM, **(5)** 4:1-S – co-culture on scaffold in 1:1 mixed medium, **(6)** 1:1-S – co-culture on scaffold in 1:1 mixed medium. Data presented as mean and ±SD.

Visual inspection for scaffolds co-cultured for 35 days revealed new matrix formation bridging the pores in the 4:1 cell ratio but it was absent in the 1:1 co-culture seeding condition (**Figure 3-15**). An SEM was conducted for those samples to evaluate ECM deposition and cellular growth in scaffolds with co-cultures, and to visualize the nature of the newly formed matrix and how variation in cellular composition influenced the type of tissue growth. Compared to the HUVECs monoculture condition, the presence of hMSCs provided a matrix that supported HUVECs adhesion and proliferation on the filament surfaces. For the 4:1 condition, scaffolds exhibited extensive ECM formation across the entire structure of the scaffold, covering the surfaces of the filaments and pore walls, with partial occlusion observed in some regions (**Figure 3-16**). At higher SEM magnification, the ECM appeared predominantly as a dense fibrillar matrix due to the higher presence of hMSCs. Globular ECM structure was occasionally present but less prominent, which is consistent with the lower proportion of HUVECs. In addition, the ECM was

found to be covered with small nodules suggestive of early signs of mineralization all over the filaments. Both types of cells successfully adhered to the scaffold surfaces. Embedded hMSCs exhibited flattened morphology with visible extensions anchored to the scaffolds, suggesting possible osteogenic differentiation. HUVECs displayed spherical morphology and were sparsely distributed, likely due to their reduced presence relative to hMSCs (**Figure 3-17** and **Figure 3-18**).

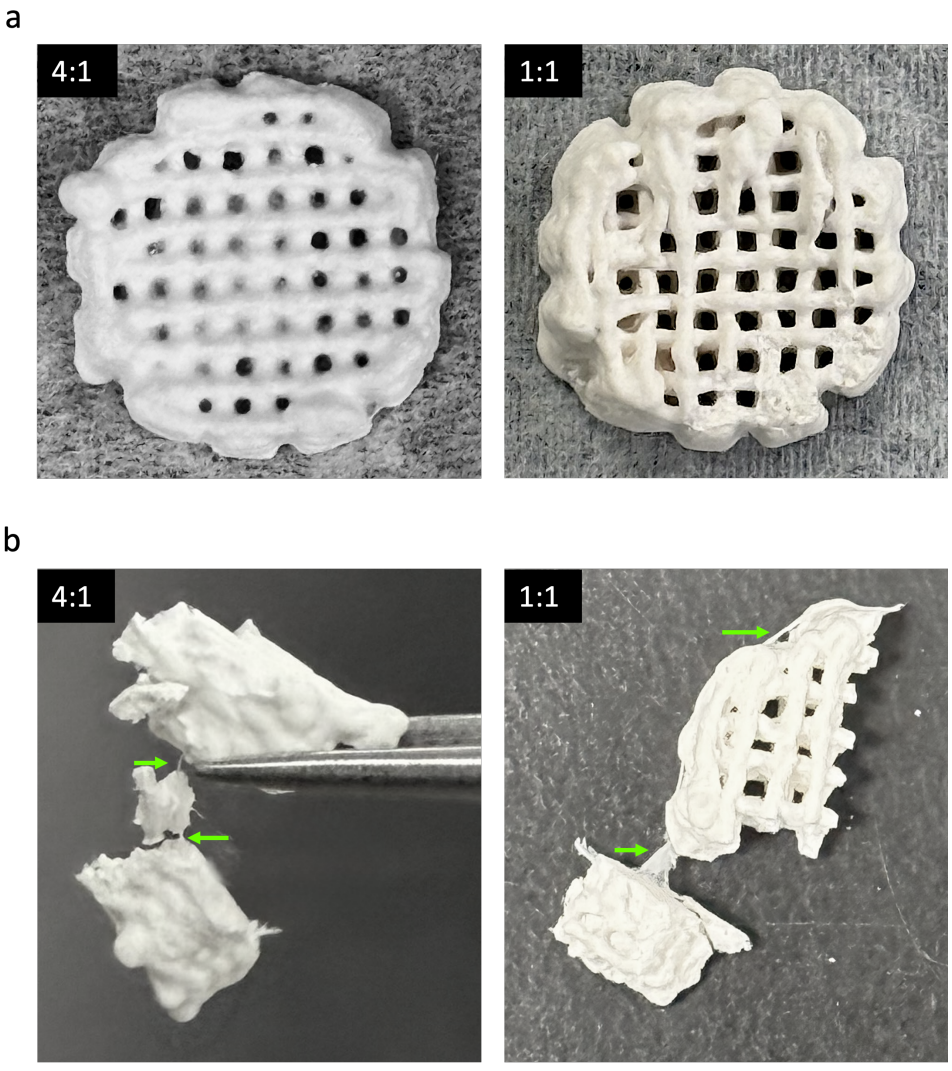

Figure 3-15. Gross images of SF-BG 63S scaffolds after 35 days of co-culture with hMSCs and HUVECs at 4:1 (left) and 1:1 (right) cell ratios in mixed OM:EGM media. **(a)** top view of intact scaffolds showing visible ECM coverage over the filaments and pores, more prominent in the 4:1 condition. **(b)** Sectioned scaffolds showing internal ECM structure. Green arrows indicate strand-like structures connecting different fragments of the scaffolds, observed spanning the constructs both externally and internally

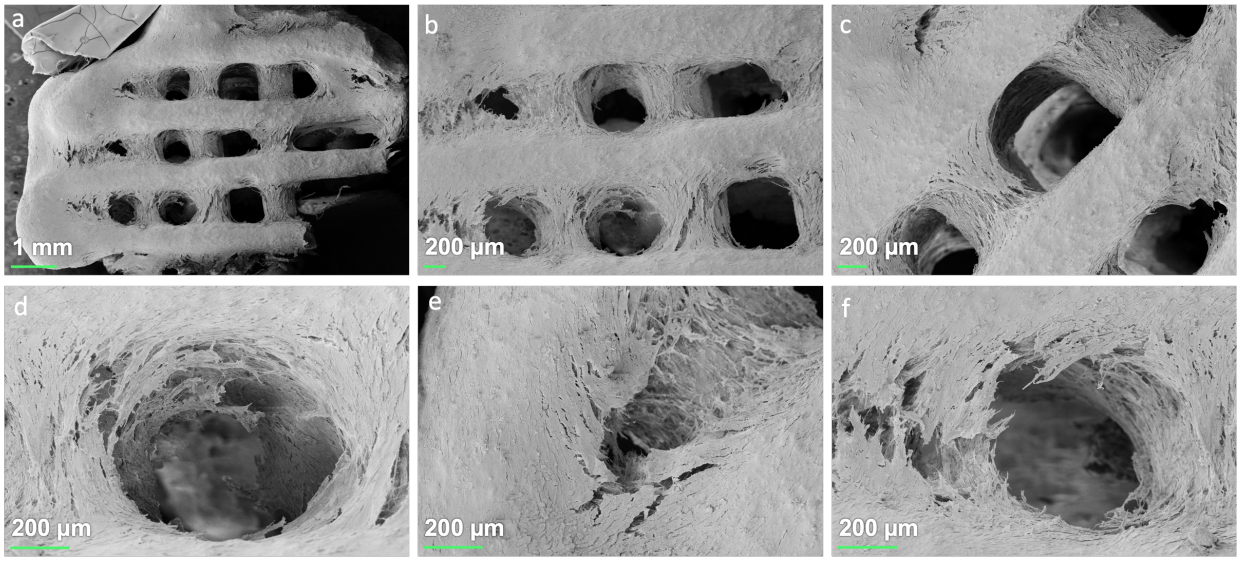

Figure 3-16. SEM images showing newly formed ECM on SF-BG 63S scaffold co-cultured at a 4:1 cell ratio for 35 days. **(a)** Scaffold morphology and structure, **(b)** and **(c)** filaments extensively covered with new matrix along the surfaces, **(d-f)** pore walls showing ECM coverage and partial occlusion at different regions on the scaffolds.

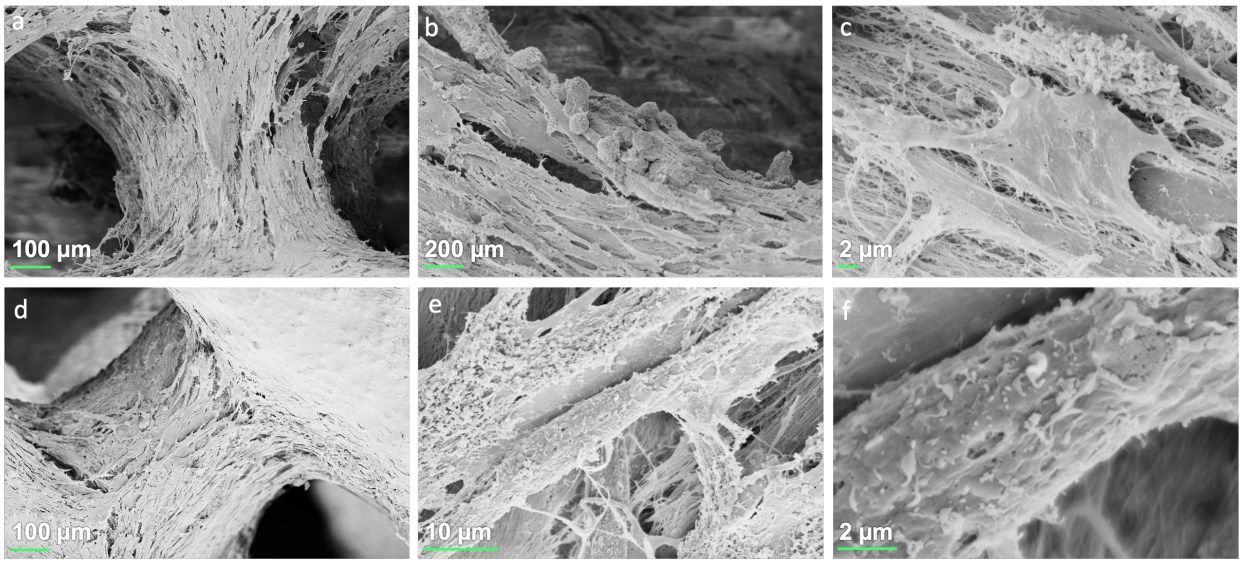

Figure 3-17. SEM images showing filament coverage and cellular interaction on SF-BG 63S scaffold co-cultured at a 4:1 cell ratio for 35 days. **(a-b)** Filament coverage with dense fibrillar ECM **(c)**, higher magnification showing a cell embedded within the ECM with visible extensions; **(d-f)** another filament showing similar matrix coverage with globular surface features and nodules along the ECM.

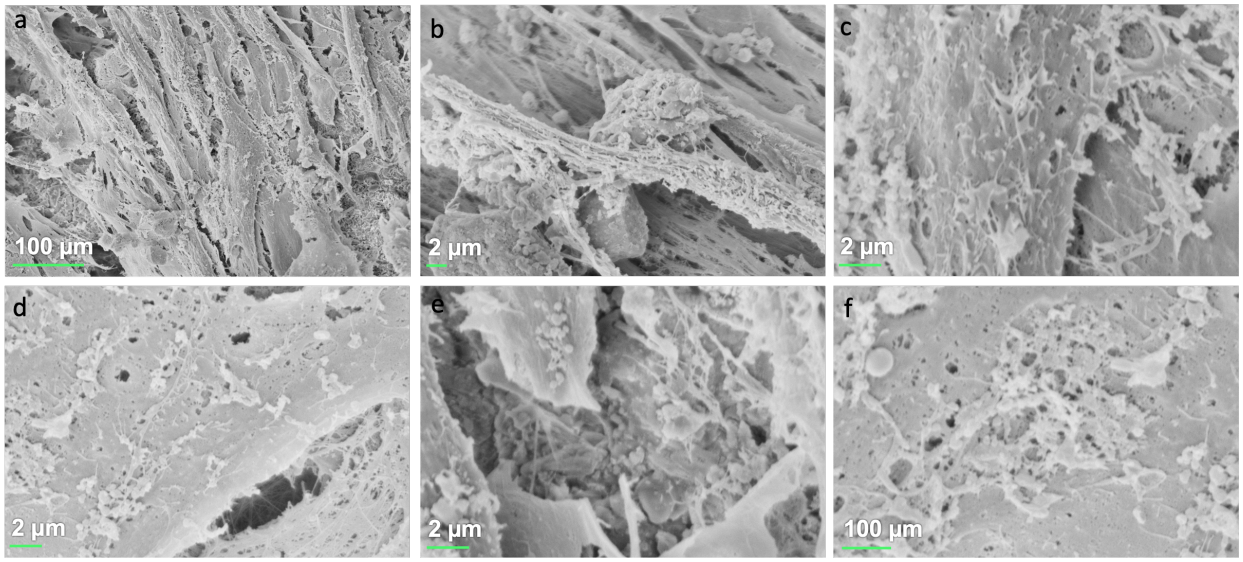

Figure 3-18. SEM images at higher magnification showing dense fibrillar ECM with globular surface features and areas of cell attachments on SF-BG 63S scaffold co-cultured at a 4:1 cell ratio and cultured for 35 days. Images were captured from various regions across the scaffold.

In contrast, the 1:1 co-culture condition exhibited an ECM organization comprising both fibrillar and globular matrix structures. They appeared more evenly distributed compared to the 4:1 co-culture condition. This reflects the equal contribution of both cell types in ECM formation along the filaments of the scaffolds. However, the newly formed ECM in this cell ratio was less dense, and limited pore coverage was observed at this time point (**Figure 3-19**). The cell morphology observed here was similar to that in the 4:1 co-culture; however, the HUVECs appeared as flattened spheres and integrated into the matrix (**Figure 3-20**). The balanced cell ratio in the 1:1 co-culture allowed both types of cells to successfully adhere and contribute to ECM formation. In addition, the presence of small nodules was also evident, scattered along the ECM in the 1:1 co-cultured scaffold (**Figure 3-20**g,h**Error! Reference source not found.**).

Notably, scaffolds in both co-culture conditions tested showed a visually visible strand-like structure spanning some of the external and internal surfaces of the scaffolds (**Figure 3-15**b). SEM imaging of these structures showed a fibrous ECM bridging between sectioned scaffold fragments. In the 4:1 co-culture, the strand appeared more fibrous with globular features and

embedded HUVECs. On the other hand, in the 1:1 co-culture, the cells appeared to be embedded into a less fibrous matrix with prominent globular features (**Figure 3-21**, and **Figure 3-22**).

The structural difference between the two co-culture groups is similar to trends previously reported by Carvalho et al.[169] In their study, they characterized ECM morphologies produced from varying MSC:HUVEC ratios. They found that decellularized matrices produced from MSC-dominant cultures displayed a dense fibrillar structure, while co-cultures with equal or HUVEC-dominant ratios resulted in ECM with globular features.[170] Although their model was based on a decellularized monolayer rather than a 3D construct, the influence of cell ratio on ECM production was comparable to those observed in the current study. The ECM formed by the 4:1 ratio in the current study displayed a predominantly fibrous arrangement, with cells embedded within the matrix, featuring osteoblast-like morphology typically associated with the osteogenic differentiation of hMSCs. In contrast, the 1:1 coculture exhibited both globular and fibrillar components, with the globular morphology being more pronounced, reflecting the higher contribution of HUVECs in ECM production.

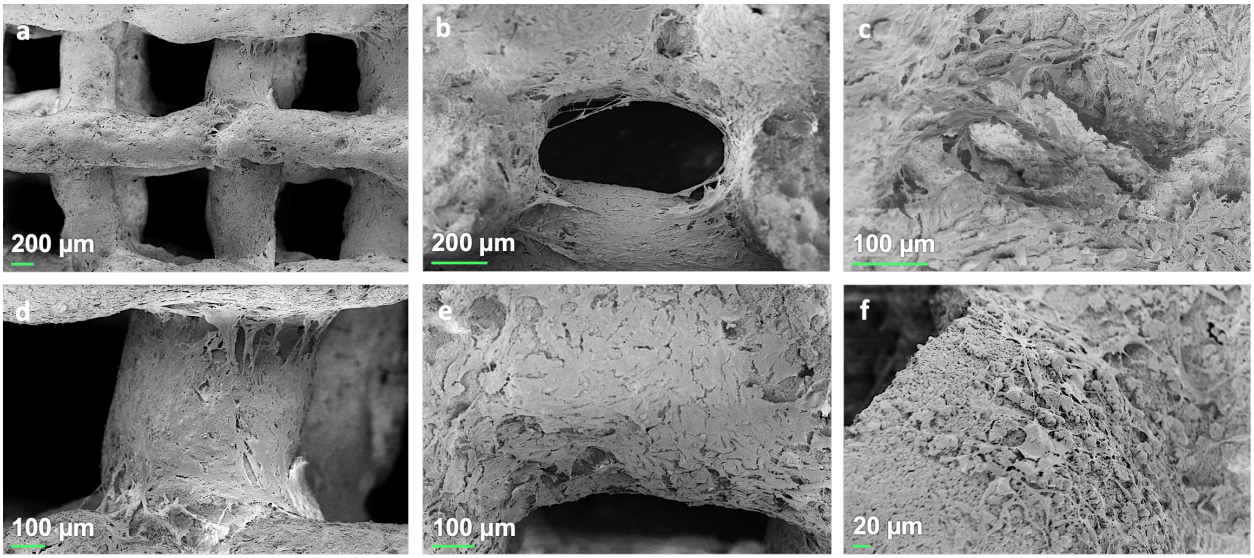

Figure 3-19. SEM images of an SF-BG 63S scaffold seeded with hMSCs and HUVECs at a 1:1 ratio and cultured for 35 days. **(a–c)** Macropores with new ECM formation. **(d–e)** Images showing Surfaces of scaffold filaments and pore walls covered with cellular growth and ECM deposition. **(f)** cells embedded and adhered to the surfaces of a filament.

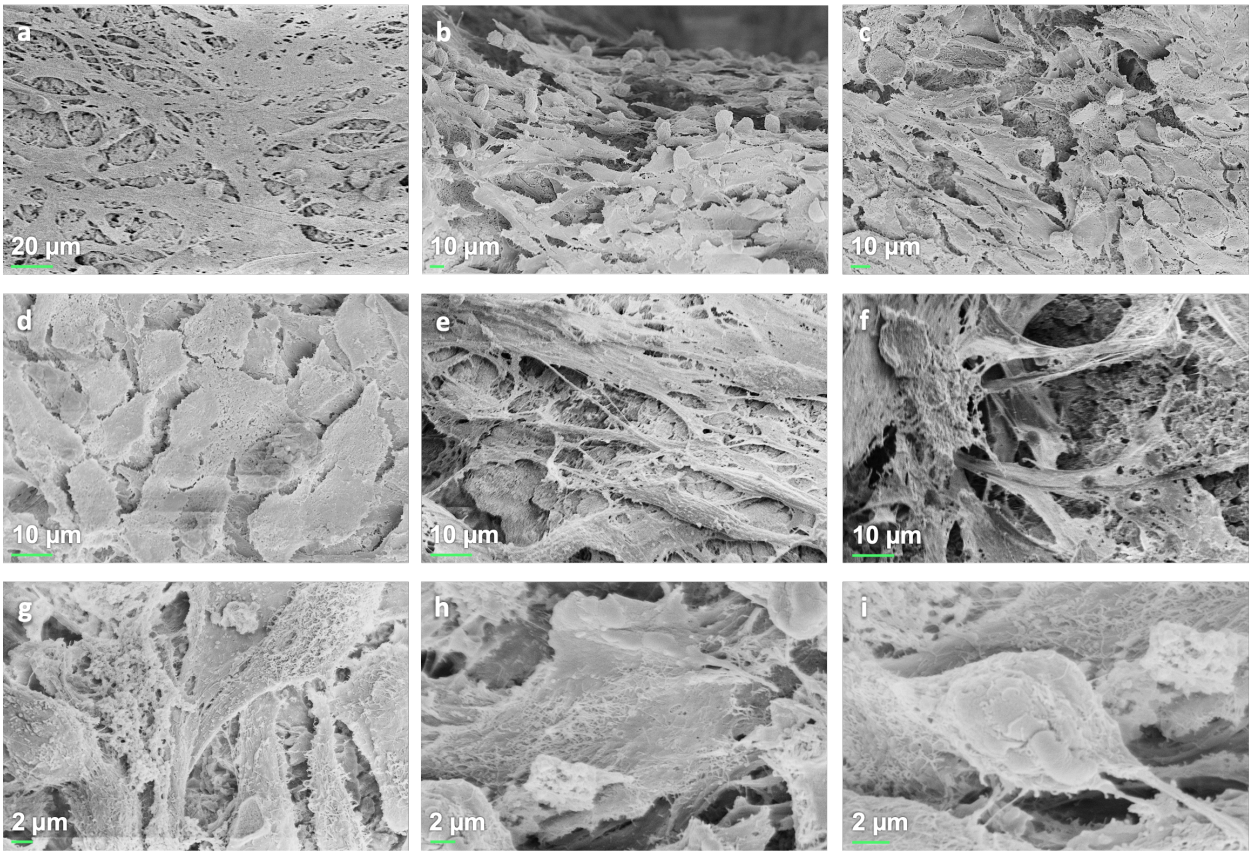

Figure 3-20. SEM images at higher magnification showing various regions across an SF-BG 63S scaffold seeded with hMSCs and HUVECs at a 1:1 ratio and cultured for 35 days. **(a–i)** Images showing the surfaces of scaffold filaments and pore walls covered with newly formed ECM and cells embedded and adhered within the matrix.

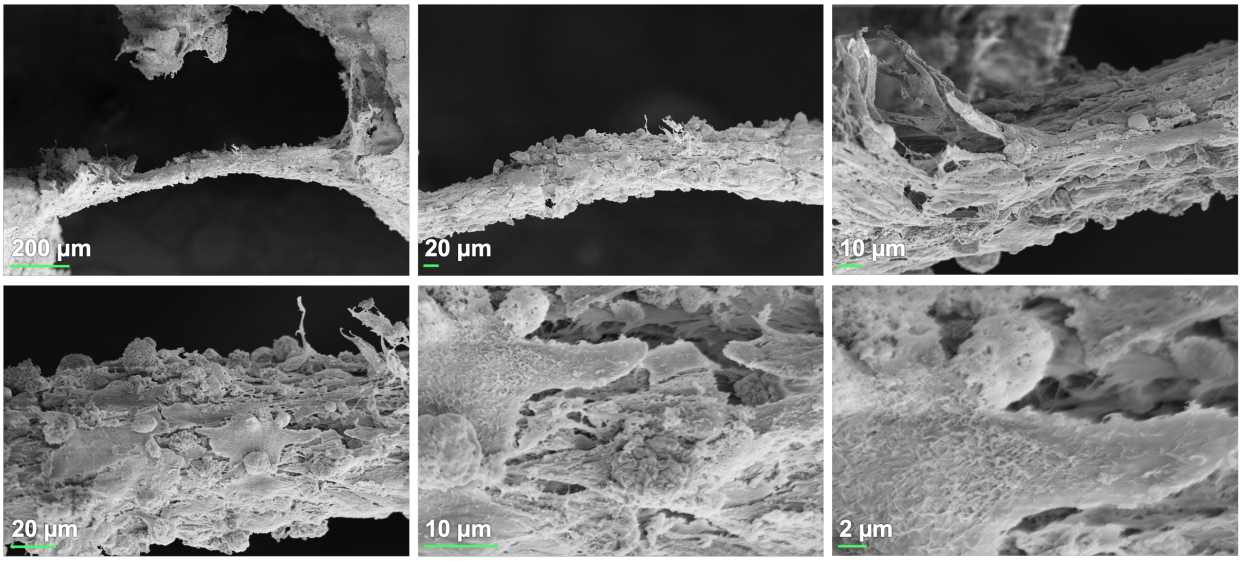

Figure 3-21. SEM images showing strand-like structures formed on SF-BG 63S scaffolds co-cultured at a 4:1 cell ratio for 35 days. **(a)** Strand-like structure spanning between two scaffold fragments. **(b–d)** Surface topography of strands at different magnifications. **(e–f)** High-magnification images showing cellular morphology and ECM organization across the strand surface.

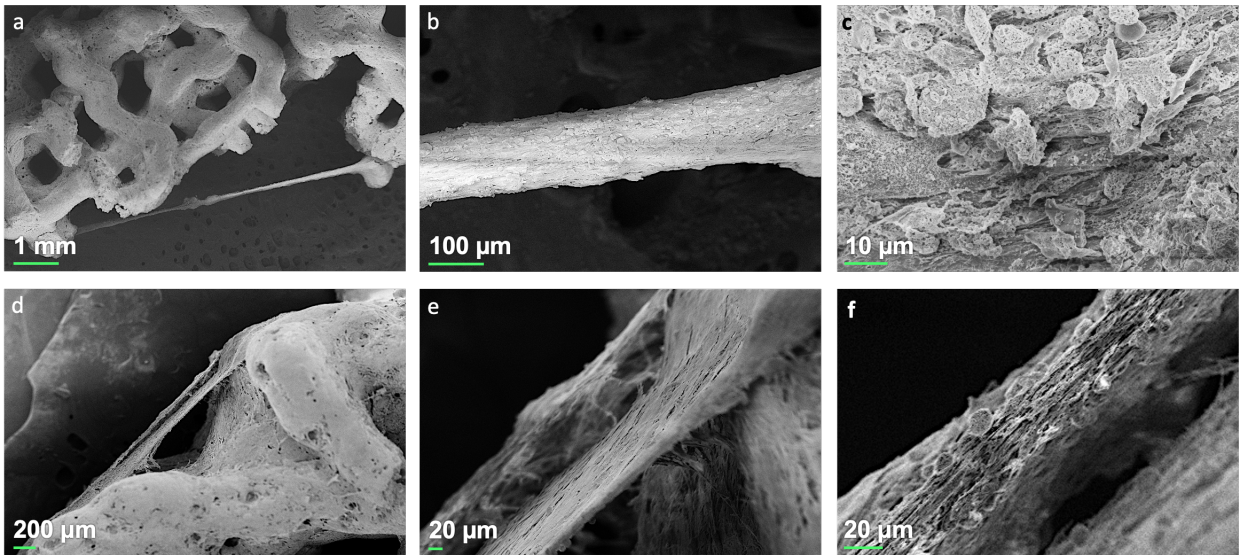

Figure 3-22. SEM images showing strand-like structures formed on SF-BG 63S scaffolds co-cultured at a 1:1 cell ratio for 35 days. **(a)** Strand-like structure extension between two scaffold fragments. **(b)** Surface topography and **(c)** cells embedded within the matrix. **(e–f)** Another strand spans along the external surface of the scaffolds at different magnifications.

To investigate the early osteogenic differentiation of the co-culture systems on the SF-BG 63S scaffolds, the quantification of ALP activity normalized to total protein content was attempted on day 21. However, the results were inconclusive, with minimal or undetectable enzymatic activity across all groups (**Figure S *3-3***). This outcome was attributed to suboptimal cellular conditions, where initial seeding appeared to be acceptable, but cell density declined over time. On day 21, the cells appeared sparse around the scaffolds with compromised morphology. Nevertheless, visual inspection of ALP-stained samples revealed a faint purple stain on the surface of a scaffold with hMSCs monoculture in OM, and it was slightly more pronounced in scaffolds with co-cultures at 4:1 and 1:1 cell ratios. This indicates a low level of early osteogenic activity despite the compromised conditions (**Figure 3-23**).

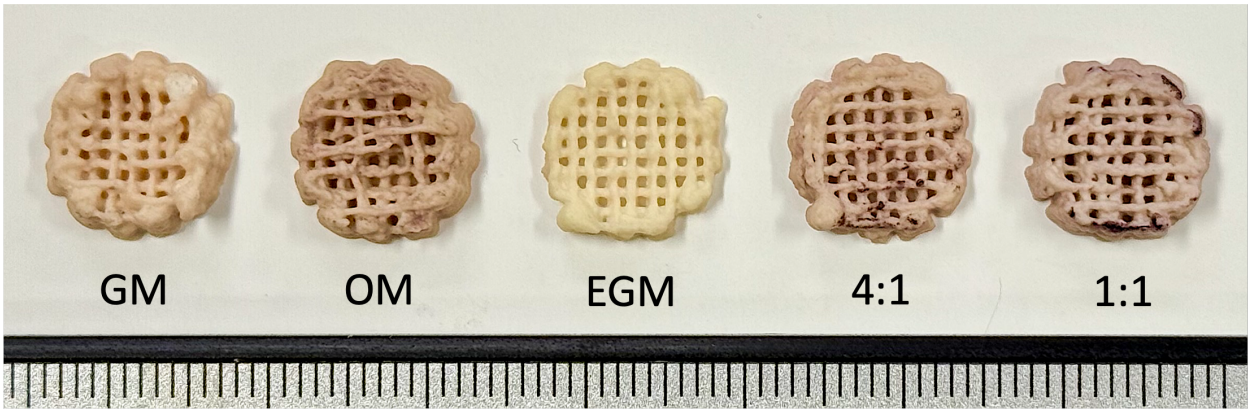

Figure 3-23. ALP staining of SF-BG 36S scaffolds at day 21 under different culture conditions. From left to right: hMSCs in GM, hMSCs in OM, HUVECs in EGM, co-cultures of hMSCs:HUVECs at 4:1 and 1:1 ratio in a blend of 1:1 OM:EGM. Purple staining reflects ALP activity and early osteogenic differentiation.

3.5. Future Directions

While the current study demonstrated the promising potential of the SF-BG 63S scaffold in supporting cell growth and early osteogenic response, it represents only a portion of a broader investigation. Future work aims to improve the material further for scaffold 3D printing, comprehensively evaluate the efficacy of the co-culture system, and assess its suitability for bone tissue regeneration.

From a material standpoint, improving the homogeneity of the ink and its ability to form stable, continuous filaments suitable for extrusion is essential for achieving consistent and scalable printing. This may be achieved by ensuring a homogeneous dispersion of bioactive glass particles and optimizing the ink formulation to enhance rheological performance. Incorporating gelatin into the ink formulation may improve the viscosity and enable thermally responsive gelation, which in turn can support shape retention after extrusion. Additionally, adopting advanced mixing techniques (e.g., planetary centrifugal mixing) may reduce particle aggregation and result in a uniform distribution of BG particles within the silk matrix.

Although the co-culture optimization study primarily focused on early osteogenic outcomes, future work will involve repeating gene expression experiments across independent studies to validate observed trends and reduce experimental variability, and provide insight into the nature of cellular responses within the co-culture system. A broader panel of osteogenic and angiogenic genes will be assessed, including Osterix, COL-1, OCN, OPN, VEGF, and CD31. Additional testing with scaffolds will evaluate the cellular behavior within the 3D printed constructs and assess the nature of the newly formed matrix. Cell tracking will be conducted to distinguish the interaction and distribution of hMSCs and HUVECs on the scaffold. To evaluate early and late differentiation and matrix formation, immunofluorescent staining of osteogenic markers, including Runx2, COL-I, OCN, and OPN, as well as angiogenic markers such as VEGF and CD31, will be employed. Given the compromised cellular conditions encountered during the ALP enzyme

quantification assay, the experiment will be repeated with optimal co-culture seeding conditions to assess early osteogenic differentiation. Altogether, these investigations aim to provide a comprehensive understanding of the co-culture system on SF-BG scaffolds in promoting bone regeneration with vascularization.

3.6. Conclusion

This study explored a co-culture-based approach to enhance the biological performance of 3D printed scaffolds for bone regeneration. By combining SF with BG 63S, we developed a printable bone cement material that supports the fabrication of scaffolds with structural features suitable for bone tissue regeneration. Using a co-culture system of hMSCs and HUVECs helped to create a biomimetic environment that simulates some aspects of native bone healing through cell-to-cell communication. This was evident by the influence of the different tested cell ratios in ECM production and organization. Although ALP results on the scaffolds were limited, the biological response seems to be promising. Overall, within the limits of this study, our results show how combining material design with a co-culture system can support the development of functional scaffolds for bone regeneration. These findings demonstrate the potential of this bioengineered system developed in this study for bone regeneration applications in non-lead-bearing areas such as the alveolar ridge.

3.7. Supplementary Figures

a

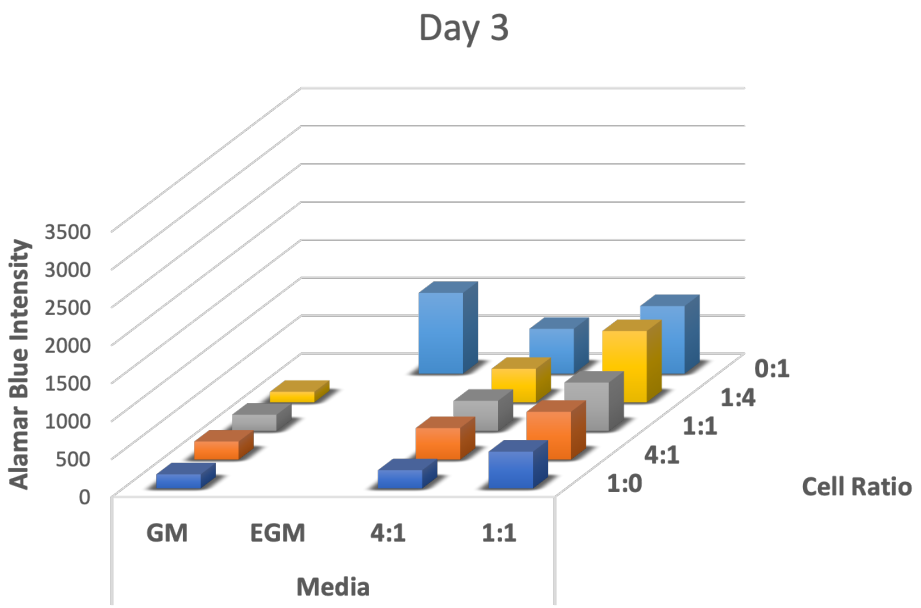

b

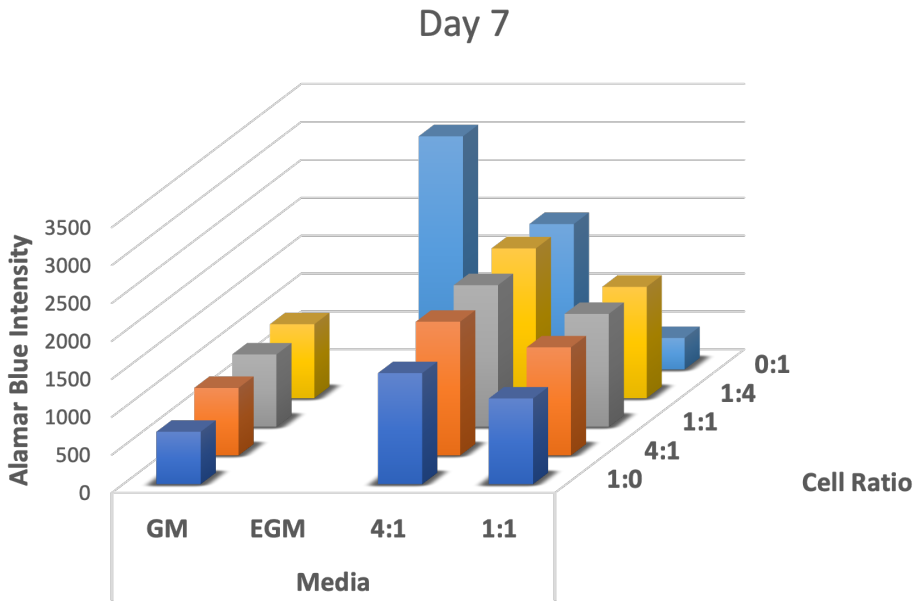

Figure S 3-1. Alamar Blue assay (n = 3) showing metabolic activity on days **(a)** 3 and **(b)** 7 during co-culture optimization in TCPS. Conditions included different mono- and co-cultures with various cell ratios and media compositions, without osteogenic differentiation. Data are presented as mean values. (Shown for reference only).

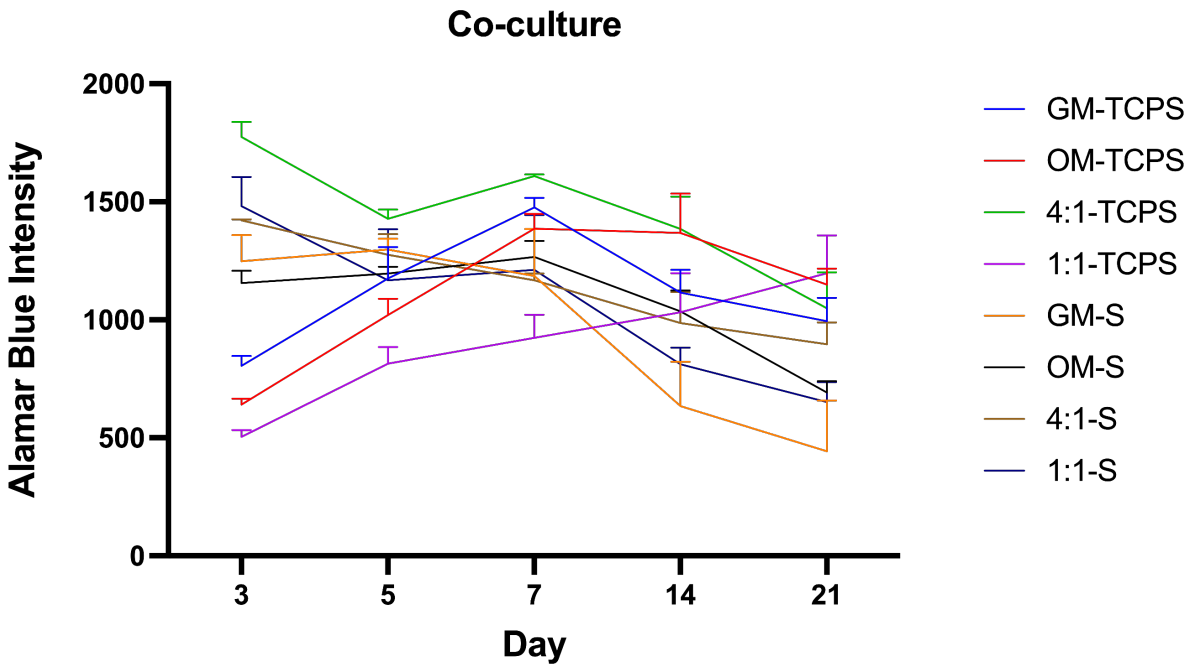

Figure S 3-2. Alamar Blue assay (n = 3) from an independent experiment assessing the metabolic activity of hMSCs and HUVECs co-culture on SF-BG 63S scaffolds and TCPS over 21 days. Conditions include: **(1)** GM-TCPS – hMSCs cultured in TCPS in GM, **(2)** OM-TCPS – hMSCs cultured in TCPS in OM, **(3)** 4:1-TCPS – co-culture on TCPS in 1:1 mixed medium, **(4)** 1:1-TCPS – co-culture on TCPS in 1:1 mixed medium, **(5)** GM-S – hMSCs on scaffolds in GM, **(6)** OM-S – hMSCs on scaffolds in OM, **(7)** 4:1-S – co-culture on scaffold in 1:1 mixed medium, **(8)** 1:1-S – co-culture on scaffold in 1:1 mixed medium. Data presented as mean and ± SD.

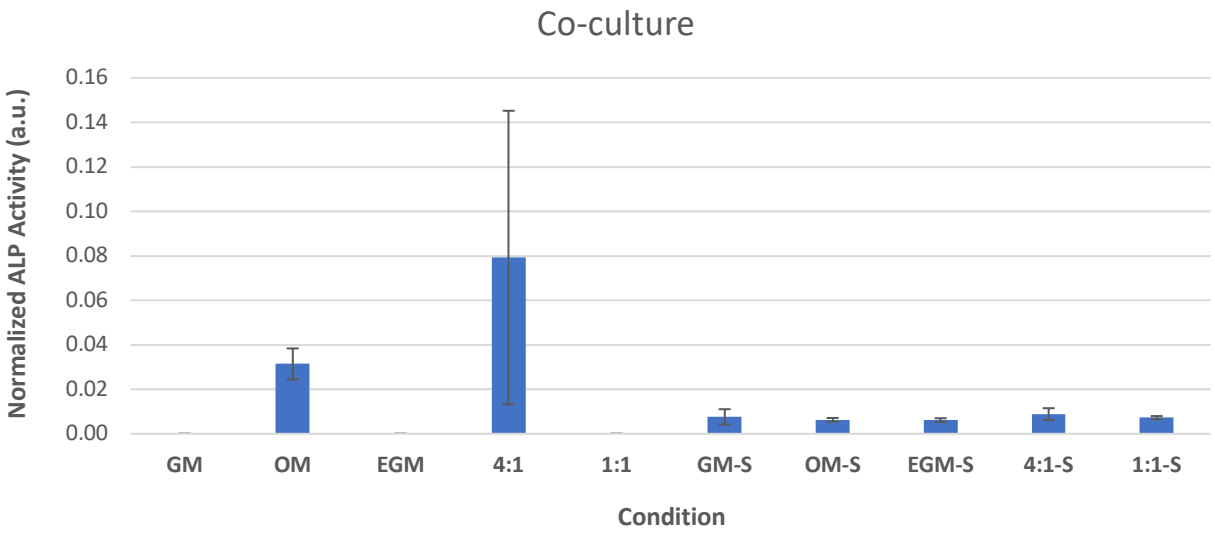

Figure S 3-3. Normalized ALP activity for SF-BG 63S scaffolds under various seeding conditions on day 21. Conditions included TCPS controls with hMSCs in GM and OM, HUVECs in EGM; co-culture on TCPS at 4:1 and 1:1 cell ratio in 1:1 mixed media; hMSCs monoculture on scaffolds in GM (GM-S), and OM (OM-S), HUVECs in EGM (EGM-S); co-culture on scaffolds at 4:1 (4:1-S) and 1:1 (1:1-S0 in 1:1 mixed media. Data presented as mean and ± SD. Due to compromised testing conditions, the results are presented for reference only

References

1. Hienz SA, Paliwal S, Ivanovski S. Mechanisms of Bone Resorption in Periodontitis. J Immunol Res. 2015;2015:615486.

2. Caton JG, Armitage G, Berglundh T, Chapple ILC, Jepsen S, Kornman KS, et al. A new classification scheme for periodontal and peri-implant diseases and conditions - Introduction and key changes from the 1999 classification. Journal of periodontology. 2018;89 Suppl 1:S1-S8.

3. Eke PI, Wei L, Borgnakke WS, Thornton-Evans G, Zhang X, Lu H, et al. Periodontitis prevalence in adults >/= 65 years of age, in the USA. Periodontol 2000. 2016;72:76-95.

4. Hou K, Song W, He J, Ma Z. The association between non-high-density lipoprotein cholesterol to high-density lipoprotein cholesterol ratio (NHHR) and prevalence of periodontitis among US adults: a cross-sectional NHANES study. Sci Rep. 2024;14:5558.

5. Eke PI, Borgnakke WS, Genco RJ. Recent epidemiologic trends in periodontitis in the USA. Periodontol 2000. 2020;82:257-67.

6. Urban IA, Monje A. Guided Bone Regeneration in Alveolar Bone Reconstruction. Oral Maxillofac Surg Clin North Am. 2019;31:331-8.

7. Kaigler D, Misch J, Alrmali A, Inglehart MR. Periodontists and stem cell-based therapy for alveolar bone regeneration: A national survey. J Periodontol. 2024;95:789-98.

8. Vo TN, Kasper FK, Mikos AG. Strategies for controlled delivery of growth factors and cells for bone regeneration. Adv Drug Deliv Rev. 2012;64:1292-309.

9. Latimer JM, Maekawa S, Yao Y, Wu DT, Chen M, Giannobile WV. Regenerative Medicine Technologies to Treat Dental, Oral, and Craniofacial Defects. Front Bioeng Biotechnol. 2021;9:704048.

10. Holly D, Klein M, Mazreku M, Zamborsky R, Polak S, Danisovic L, et al. Stem Cells and Their Derivatives-Implications for Alveolar Bone Regeneration: A Comprehensive Review. International journal of molecular sciences. 2021;22.

11. Vaquette C, Mitchell J, Fernandez-Medina T, Kumar S, Ivanovski S. Resorbable additively manufactured scaffold imparts dimensional stability to extraskeletally regenerated bone. Biomaterials. 2021;269:120671.

12. Florencio-Silva R, Sasso GR, Sasso-Cerri E, Simoes MJ, Cerri PS. Biology of Bone Tissue: Structure, Function, and Factors That Influence Bone Cells. Biomed Res Int. 2015;2015:421746.

13. Datta HK, Ng WF, Walker JA, Tuck SP, Varanasi SS. The cell biology of bone metabolism. J Clin Pathol. 2008;61:577-87.

14. Buck DW, 2nd, Dumanian GA. Bone biology and physiology: Part I. The fundamentals. Plast Reconstr Surg. 2012;129:1314-20.

15. Bartold M, Gronthos S, Haynes D, Ivanovski S. Mesenchymal stem cells and biologic factors leading to bone formation. Journal of clinical periodontology. 2019;46 Suppl 21:12-32.

16. Jonasson G, Skoglund I, Rythen M. The rise and fall of the alveolar process: Dependency of teeth and metabolic aspects. Arch Oral Biol. 2018;96:195-200.

17. Guo S, Dipietro LA. Factors affecting wound healing. J Dent Res. 2010;89:219-29.

18. Schenk RK, Buser D, Hardwick WR, Dahlin C. Healing pattern of bone regeneration in membrane-protected defects: a histologic study in the canine mandible. Int J Oral Maxillofac Implants. 1994;9:13-29.

19. Schemitsch EH. Size Matters: Defining Critical in Bone Defect Size! J Orthop Trauma. 2017;31 Suppl 5:S20-S2.

20. Lindhe J, Lang NP, Karring T. Text Book of clinical Periodontology and implant dentistry. :: Munksgaard; 2003.

21. EzEldeen M, Moroni L, Nejad ZM, Jacobs R, Mota C. Biofabrication of engineered dento-alveolar tissue. Biomater Adv. 2023;148:213371.

22. Nanci A, Bosshardt DD. Structure of periodontal tissues in health and disease. Periodontology 2000. 2006;40:11-28.

23. Araujo MG, Silva CO, Misawa M, Sukekava F. Alveolar socket healing: what can we learn? Periodontology 2000. 2015;68:122-34.

24. Zhao R, Yang R, Cooper PR, Khurshid Z, Shavandi A, Ratnayake J. Bone Grafts and Substitutes in Dentistry: A Review of Current Trends and Developments. Molecules. 2021;26.

25. Titsinides S, Agrogiannis G, Karatzas T. Bone grafting materials in dentoalveolar reconstruction: A comprehensive review. Jpn Dent Sci Rev. 2019;55:26-32.

26. Schropp L, Wenzel A, Kostopoulos L, Karring T. Bone healing and soft tissue contour changes following single-tooth extraction: a clinical and radiographic 12-month prospective study. Int J Periodontics Restorative Dent. 2003;23:313-23.

27. Tan WL, Wong TL, Wong MC, Lang NP. A systematic review of post-extractional alveolar hard and soft tissue dimensional changes in humans. Clin Oral Implants Res. 2012;23 Suppl 5:1-21.

28. Reich KM, Huber CD, Lippnig WR, Ulm C, Watzek G, Tangl S. Atrophy of the residual alveolar ridge following tooth loss in an historical population. Oral Dis. 2011;17:33-44.

29. Lam RV. Contour changes of the alveolar processes following extractions. The Journal of Prosthetic Dentistry. 1960;10:25-32.

30. Araujo MG, Lindhe J. Ridge alterations following tooth extraction with and without flap elevation: an experimental study in the dog. Clinical oral implants research. 2009;20:545-9.

31. Mardas N, Macbeth N, Donos N, Jung RE, Zuercher AN. Is alveolar ridge preservation an overtreatment? Periodontology 2000. 2023;93:289-308.

32. Araujo MG, Lindhe J. Dimensional ridge alterations following tooth extraction. An experimental study in the dog. Journal of clinical periodontology. 2005;32:212-8.

33. Tallgren A, Tallgren A. The continuing reduction of the residual alveolar ridges in complete denture wearers: a mixed-longitudinal study covering 25 years. 1972. The Journal of prosthetic dentistry. 2003;89:427-35.

34. Nemcovsky CE, Serfaty V. Alveolar ridge preservation following extraction of maxillary anterior teeth. Report on 23 consecutive cases. Journal of periodontology. 1996;67:390-5.

35. Atwood DA. Bone Loss of Edentulous Alveolar Ridges. Journal of periodontology. 1979;50 Suppl 4S:11-21.

36. Clementini M, Morlupi A, Canullo L, Agrestini C, Barlattani A. Success rate of dental implants inserted in horizontal and vertical guided bone regenerated areas: a systematic review. Int J Oral Maxillofac Surg. 2012;41:847-52.

37. Rocchietta I, Fontana F, Simion M. Clinical outcomes of vertical bone augmentation to enable dental implant placement: a systematic review. J Clin Periodontol. 2008;35:203-15.

38. Stavropoulos A, Nyengaard JR, Kostopoulos L, Karring T. Implant placement in bone formed beyond the skeletal envelope by means of guided tissue regeneration: an experimental study in the rat. Journal of clinical periodontology. 2005;32:1108-15.

39. Jepsen S, Schwarz F, Cordaro L, Derks J, Hammerle CHF, Heitz-Mayfield LJ, et al. Regeneration of alveolar ridge defects. Consensus report of group 4 of the 15th European Workshop on Periodontology on Bone Regeneration. Journal of clinical periodontology. 2019;46 Suppl 21:277-86.

40. Tolstunov L, Hamrick JFE, Broumand V, Shilo D, Rachmiel A. Bone Augmentation Techniques for Horizontal and Vertical Alveolar Ridge Deficiency in Oral Implantology. Oral Maxillofac Surg Clin North Am. 2019;31:163-91.

41. Bernstein S, Cooke J, Fotek P, Wang H-L. Vertical bone augmentation: where are we now? Implant dentistry. 2006;15:219-28.

42. Stavropoulos A, Marcantonio CC, de Oliveira VXR, Marcantonio E, Jr., de Oliveira GJPL. Fresh-frozen allogeneic bone blocks grafts for alveolar ridge augmentation: Biological and clinical aspects. Periodontology 2000. 2023;93:139-52.

43. Khojasteh A, Kheiri L, Motamedian SR, Khoshkam V. Guided Bone Regeneration for the Reconstruction of Alveolar Bone Defects. Ann Maxillofac Surg. 2017;7:263-77.

44. Liu J, Kerns DG. Mechanisms of guided bone regeneration: a review. Open Dent J. 2014;8:56-65.

45. Wang HL, Boyapati L. "PASS" principles for predictable bone regeneration. Implant Dent. 2006;15:8-17.

46. Jung RE, Fenner N, Hammerle CHF, Zitzmann NU. Long-term outcome of implants placed with guided bone regeneration (GBR) using resorbable and non-resorbable membranes after 12-14 years. Clinical oral implants research. 2013;24:1065-73.

47. Heimes D, Pabst A, Becker P, Hartmann A, Kloss F, Tunkel J, et al. Comparison of morbidity-related parameters between autologous and allogeneic bone grafts for alveolar ridge augmentation from patients' perspective-A questionnaire-based cohort study. Clinical implant dentistry and related research. 2024;26:170-82.

48. Donos N, Akcali A, Padhye N, Sculean A, Calciolari E. Bone regeneration in implant dentistry: Which are the factors affecting the clinical outcome? Periodontol 2000. 2023;93:26-55.

49. Fontana F, Maschera E, Rocchietta I, Simion M. Clinical classification of complications in guided bone regeneration procedures by means of a nonresorbable membrane. The International journal of periodontics & restorative dentistry. 2011;31:265-73.

50. Campana V, Milano G, Pagano E, Barba M, Cicione C, Salonna G, et al. Bone substitutes in orthopaedic surgery: from basic science to clinical practice. Journal of materials science Materials in medicine. 2014;25:2445-61.

51. Finkemeier CG. Bone-Grafting and Bone-Graft Substitutes. JBJS. 2002;84:454-64.

52. Haugen HJ, Lyngstadaas SP, Rossi F, Perale G. Bone grafts: which is the ideal biomaterial? Journal of clinical periodontology. 2019;46 Suppl 21:92-102.

53. Fillingham Y, Jacobs J. Bone grafts and their substitutes. Bone Joint J. 2016;98-B:6-9.

54. Whitehouse MR, Blom AW. The Use of Ceramics as Bone Substitutes in Revision Hip Arthroplasty: Materials (Basel). 2009 Nov 19;2(4):1895-907. doi: 10.3390/ma2041895. eCollection 2009 Dec.

55. Bose S, Tarafder S. Calcium phosphate ceramic systems in growth factor and drug delivery for bone tissue engineering: a review. Acta biomaterialia. 2012;8:1401-21.

56. Lobo SE, Arinzeh TL. Biphasic Calcium Phosphate Ceramics for Bone Regeneration and Tissue Engineering Applications: Materials (Basel). 2010 Jan 29;3(2):815-26. doi: 10.3390/ma3020815. eCollection 2010 Feb.

57. Habibovic P, Kruyt MC, Juhl MV, Clyens S, Martinetti R, Dolcini L, et al. Comparative in vivo study of six hydroxyapatite-based bone graft substitutes. J Orthop Res. 2008;26:1363-70.

58. Oliveira HL, Da Rosa WLO, Cuevas-Suarez CE, Carreno NLV, da Silva AF, Guim TN, et al. Histological Evaluation of Bone Repair with Hydroxyapatite: A Systematic Review. Calcif Tissue Int. 2017;101:341-54.

59. Mohd Pu'ad NAS, Koshy P, Abdullah HZ, Idris MI, Lee TC. Syntheses of hydroxyapatite from natural sources. Heliyon. 2019;5:e01588.

60. Bouler JM, Pilet P, Gauthier O, Verron E. Biphasic calcium phosphate ceramics for bone reconstruction: A review of biological response. Acta Biomater. 2017;53:1-12.

61. Bellucci D, Sola A, Cannillo V. Hydroxyapatite and tricalcium phosphate composites with bioactive glass as second phase: State of the art and current applications. Journal of biomedical materials research Part A. 2016;104:1030-56.

62. Korn P, Schulz MC, Range U, Lauer G, Pradel W. Efficacy of tissue engineered bone grafts containing mesenchymal stromal cells for cleft alveolar osteoplasty in a rat model. J Craniomaxillofac Surg. 2014;42:1277-85.

63. Pilipchuk SP, Plonka AB, Monje A, Taut AD, Lanis A, Kang B, et al. Tissue engineering for bone regeneration and osseointegration in the oral cavity. Dent Mater. 2015;31:317-38.

64. Janicki P, Schmidmaier G. What should be the characteristics of the ideal bone graft substitute? Combining scaffolds with growth factors and/or stem cells. Injury. 2011;42 Suppl 2:S77-81.

65. Zakrzewski W, Dobrzynski M, Rybak Z, Szymonowicz M, Wiglusz RJ. Selected Nanomaterials' Application Enhanced with the Use of Stem Cells in Acceleration of Alveolar Bone Regeneration during Augmentation Process. Nanomaterials (Basel). 2020;10.

66. Liao X, Lu S, Zhuo Y, Winter C, Xu W, Li B, et al. Bone Physiology, Biomaterial and the Effect of Mechanical/Physical Microenvironment on MSC Osteogenesis: A Tribute to Shu Chien's 80th Birthday. Cell Mol Bioeng. 2011;4:579-90.

67. Guan N, Liu Z, Zhao Y, Li Q, Wang Y. Engineered biomaterial strategies for controlling growth factors in tissue engineering. Drug Deliv. 2020;27:1438-51.

68. Zhao X, Hu DA, Wu D, He F, Wang H, Huang L, et al. Applications of Biocompatible Scaffold Materials in Stem Cell-Based Cartilage Tissue Engineering. Frontiers in bioengineering and biotechnology. 2021;9:603444.

69. Porter JR, Ruckh TT, Popat KC. Bone tissue engineering: a review in bone biomimetics and drug delivery strategies. Biotechnol Prog. 2009;25:1539-60.

70. Cheng N, Wang Y, Zhang Y, Shi B. The osteogenic potential of mesoporous bioglasses/silk and non-mesoporous bioglasses/silk scaffolds in ovariectomized rats: in vitro and in vivo evaluation. PloS one. 2013;8:e81014.

71. Huang X, Lou Y, Duan Y, Liu H, Tian J, Shen Y, et al. Biomaterial scaffolds in maxillofacial bone tissue engineering: A review of recent advances. Bioactive materials. 2024;33:129-56.

72. Karageorgiou V, Kaplan D. Porosity of 3D biomaterial scaffolds and osteogenesis. Biomaterials. 2005;26:5474-91.

73. Zhu L, Luo D, Liu Y. Effect of the nano/microscale structure of biomaterial scaffolds on bone regeneration. Int J Oral Sci. 2020;12:6.

74. Richards DJ, Tan Y, Jia J, Yao H, Mei Y. 3D Printing for Tissue Engineering. Isr J Chem. 2013;53:805-14.

75. Haleem A, Javaid M, Khan RH, Suman R. 3D printing applications in bone tissue engineering. J Clin Orthop Trauma. 2020;11:S118-S24.

76. Wasti S, Adhikari S. Use of Biomaterials for 3D Printing by Fused Deposition Modeling Technique: A Review. Front Chem. 2020;8:315.

77. Song X, Philpott MA, Best SM, Cameron RE. Controlling the Architecture of Freeze-Dried Collagen Scaffolds with Ultrasound-Induced Nucleation. Polymers. 2024;16.

78. Fu Q, Saiz E, Tomsia AP. Direct ink writing of highly porous and strong glass scaffolds for load-bearing bone defects repair and regeneration. Acta biomaterialia. 2011;7:3547-54.

79. Schwab A, Levato R, D'Este M, Piluso S, Eglin D, Malda J. Printability and Shape Fidelity of Bioinks in 3D Bioprinting. Chem Rev. 2020;120:11028-55.

80. Saadi MASR, Maguire A, Pottackal NT, Thakur MSH, Ikram MM, Hart AJ, et al. Direct Ink Writing: A 3D Printing Technology for Diverse Materials. Adv Mater. 2022;34:e2108855.

81. Milazzo M, Fitzpatrick V, Owens CE, Carraretto IM, McKinley GH, Kaplan DL, et al. 3D Printability of Silk/Hydroxyapatite Composites for Microprosthetic Applications. ACS Biomater Sci Eng. 2023;9:1285-95.

82. Fitzpatrick V, Martin-Moldes Z, Deck A, Torres-Sanchez R, Valat A, Cairns D, et al. Functionalized 3D-printed silk-hydroxyapatite scaffolds for enhanced bone regeneration with innervation and vascularization. Biomaterials. 2021;276:120995.

83. Midha S, Kumar S, Sharma A, Kaur K, Shi X, Naruphontjirakul P, et al. Silk fibroin-bioactive glass based advanced biomaterials: towards patient-specific bone grafts. Biomed Mater. 2018;13:055012.

84. DeBari MK, Keyser MN, Bai MA, Abbott RD. 3D printing with silk: considerations and applications. Connect Tissue Res. 2020;61:163-73.

85. Vepari C, Kaplan DL. Silk as a Biomaterial. Prog Polym Sci. 2007;32:991-1007.

86. Li C, Wu J, Shi H, Xia Z, Sahoo JK, Yeo J, et al. Fiber-Based Biopolymer Processing as a Route toward Sustainability. Adv Mater. 2022;34:e2105196.

87. Sun W, Gregory DA, Tomeh MA, Zhao X. Silk Fibroin as a Functional Biomaterial for Tissue Engineering. International journal of molecular sciences. 2021;22.

88. Farokhi M, Mottaghitalab F, Samani S, Shokrgozar MA, Kundu SC, Reis RL, et al. Silk fibroin/hydroxyapatite composites for bone tissue engineering. Biotechnol Adv. 2018;36:68-91.

89. Gupta P, Adhikary M, M JC, Kumar M, Bhardwaj N, Mandal BB. Biomimetic, Osteoconductive Non-mulberry Silk Fiber Reinforced Tricomposite Scaffolds for Bone Tissue Engineering. ACS Appl Mater Interfaces. 2016;8:30797-810.

90. Nguyen TP, Nguyen QV, Nguyen V-H, Le T-H, Huynh VQN, Vo D-VN, et al. Silk Fibroin-Based Biomaterials for Biomedical Applications: A Review. Polymers. 2019;11.

91. McNamara SL, Rnjak-Kovacina J, Schmidt DF, Lo TJ, Kaplan DL. Silk as a biocohesive sacrificial binder in the fabrication of hydroxyapatite load bearing scaffolds. Biomaterials. 2014;35:6941-53.

92. Sun L, Parker ST, Syoji D, Wang X, Lewis JA, Kaplan DL. Direct-write assembly of 3D silk/hydroxyapatite scaffolds for bone co-cultures. Adv Healthc Mater. 2012;1:729-35.

93. Ding Z, Han H, Fan Z, Lu H, Sang Y, Yao Y, et al. Nanoscale Silk-Hydroxyapatite Hydrogels for Injectable Bone Biomaterials. ACS Appl Mater Interfaces. 2017;9:16913-21.

94. Alvarez P, Hee CK, Solchaga L, Snel L, Kestler HK, Lynch SE, et al. Growth factors and craniofacial surgery. J Craniofac Surg. 2012;23:20-9.

95. De Witte TM, Fratila-Apachitei LE, Zadpoor AA, Peppas NA. Bone tissue engineering via growth factor delivery: from scaffolds to complex matrices. Regen Biomater. 2018;5:197-211.

96. Wang ZM, Wang ZF, Lu WW, Zhen WX, Yang DZ, Peng SL. Novel biomaterial strategies for controlled growth factor delivery for biomedical applications. Npg Asia Mater. 2017;9.

97. Hettiaratchi MH, Krishnan L, Rouse T, Chou C, McDevitt TC, Guldberg RE. Heparin-mediated delivery of bone morphogenetic protein-2 improves spatial localization of bone regeneration. Sci Adv. 2020;6:eaay1240.

98. Hollinger JO, Hart CE, Hirsch SN, Lynch S, Friedlaender GE. Recombinant human platelet-derived growth factor: biology and clinical applications. J Bone Joint Surg Am. 2008;90 Suppl 1:48-54.

99. Lee J, Yun J, Kim K-H, Koo K-T, Seol Y-J, Lee Y-M. Periodontal Regeneration Using Recombinant Human Bone Morphogenetic Protein-2 and a Bilayer Collagen Matrix. The Journal of craniofacial surgery. 2020;31:1602-7.

100. Paulini M, Camal Ruggieri IN, Ramallo M, Alonso M, Rodriguez-Cabello JC, Esbrit P, et al. Recombinant Proteins-Based Strategies in Bone Tissue Engineering. Biomolecules. 2021;12.

101. Cheng H, Jiang W, Phillips FM, Haydon RC, Peng Y, Zhou L, et al. Osteogenic activity of the fourteen types of human bone morphogenetic proteins (BMPs). The Journal of bone and joint surgery American volume. 2003;85:1544-52.

102. Boyne PJ, Lilly LC, Marx RE, Moy PK, Nevins M, Spagnoli DB, et al. De novo bone induction by recombinant human bone morphogenetic protein-2 (rhBMP-2) in maxillary sinus floor augmentation. J Oral Maxillofac Surg. 2005;63:1693-707.

103. On S-W, Park S-Y, Yi S-M, Park I-Y, Byun S-H, Yang B-E. Current Status of Recombinant Human Bone Morphogenetic Protein-2 (rhBMP-2) in Maxillofacial Surgery: Should It Be Continued? Bioengineering (Basel). 2023;10.

104. Kim MS, Lee JS, Shin HK, Kim JS, Yun JH, Cho KS. Prospective randomized, controlled trial of sinus grafting using Escherichia-coli-produced rhBMP-2 with a biphasic calcium phosphate carrier compared to deproteinized bovine bone. Clin Oral Implants Res. 2015;26:1361-8.

105. Kim H-S, Park J-C, Yun P-Y, Kim Y-K. Evaluation of bone healing using rhBMP-2 soaked hydroxyapatite in ridge augmentation: a prospective observational study. Maxillofacial plastic and reconstructive surgery. 2017;39:40.

106. Galarraga-Vinueza ME, Barootchi S, Nevins ML, Nevins M, Miron RJ, Tavelli L. Twenty-five years of recombinant human growth factors rhPDGF-BB and rhBMP-2 in oral hard and soft tissue regeneration. Periodontology 2000. 2024;94:483-509.

107. Tavelli L, Ravida A, Barootchi S, Chambrone L, Giannobile WV. Recombinant Human Platelet-Derived Growth Factor: A Systematic Review of Clinical Findings in Oral Regenerative Procedures. JDR Clin Trans Res. 2021;6:161-73.

108. Shields LB, Raque GH, Glassman SD, Campbell M, Vitaz T, Harpring J, et al. Adverse effects associated with high-dose recombinant human bone morphogenetic protein-2 use in anterior cervical spine fusion. Spine (Phila Pa 1976). 2006;31:542-7.

109. Marian D, Toro G, D'Amico G, Trotta MC, D'Amico M, Petre A, et al. Challenges and Innovations in Alveolar Bone Regeneration: A Narrative Review on Materials, Techniques, Clinical Outcomes, and Future Directions. Medicina (Kaunas). 2024;61.

110. Daniels TR, Anderson J, Swords MP, Maislin G, Donahue R, Pinsker E, et al. Recombinant Human Platelet-Derived Growth Factor BB in Combination With a Beta-Tricalcium Phosphate (rhPDGF-BB/beta-TCP)-Collagen Matrix as an Alternative to Autograft. Foot Ankle Int. 2019;40:1068-78.

111. Boda SK, Almoshari Y, Wang H, Wang X, Reinhardt RA, Duan B, et al. Mineralized nanofiber segments coupled with calcium-binding BMP-2 peptides for alveolar bone regeneration. Acta Biomater. 2019;85:282-93.

112. Zhai P, Peng X, Li B, Liu Y, Sun H, Li X. The application of hyaluronic acid in bone regeneration. Int J Biol Macromol. 2020;151:1224-39.

113. Bai X, Gao M, Syed S, Zhuang J, Xu X, Zhang XQ. Bioactive hydrogels for bone regeneration. Bioact Mater. 2018;3:401-17.

114. Khunmanee S, Jeong Y, Park H. Crosslinking method of hyaluronic-based hydrogel for biomedical applications. J Tissue Eng. 2017;8:2041731417726464.

115. Kisiel M, Martino MM, Ventura M, Hubbell JA, Hilborn J, Ossipov DA. Improving the osteogenic potential of BMP-2 with hyaluronic acid hydrogel modified with integrin-specific fibronectin fragment. Biomaterials. 2013;34:704-12.

116. Kim J, Kim IS, Cho TH, Lee KB, Hwang SJ, Tae G, et al. Bone regeneration using hyaluronic acid-based hydrogel with bone morphogenic protein-2 and human mesenchymal stem cells. Biomaterials. 2007;28:1830-7.

117. Bhakta G, Lim ZXH, Rai B, Lin T, Hui JH, Prestwich GD, et al. The influence of collagen and hyaluronan matrices on the delivery and bioactivity of bone morphogenetic protein-2 and ectopic bone formation. Acta biomaterialia. 2013;9:9098-106.

118. Bhakta G, Rai B, Lim ZXH, Hui JH, Stein GS, van Wijnen AJ, et al. Hyaluronic acid-based hydrogels functionalized with heparin that support controlled release of bioactive BMP-2. Biomaterials. 2012;33:6113-22.

119. Bae MS, Ko NR, Lee SJ, Lee JB, Heo DN, Byun W, et al. Development of novel photopolymerizable hyaluronic acid/heparin-based hydrogel scaffolds with a controlled release of growth factors for enhanced bone regeneration. Macromolecular Research. 2016;24:829-37.

120. Rindone AN, Kachniarz B, Achebe CC, Riddle RC, O'Sullivan AN, Dorafshar AH, et al. Heparin-Conjugated Decellularized Bone Particles Promote Enhanced Osteogenic Signaling of PDGF-BB to Adipose-Derived Stem Cells in Tissue Engineered Bone Grafts. Adv Healthc Mater. 2019;8:e1801565.

121. Rolny C, Spillmann D, Lindahl U, Claesson-Welsh L. Heparin amplifies platelet-derived growth factor (PDGF)- BB-induced PDGF alpha -receptor but not PDGF beta -receptor tyrosine phosphorylation in heparan sulfate-deficient cells. Effects on signal transduction and biological responses. J Biol Chem. 2002;277:19315-21.

122. Rockwood DN, Preda RC, Yucel T, Wang X, Lovett ML, Kaplan DL. Materials fabrication from Bombyx mori silk fibroin. Nat Protoc. 2011;6:1612-31.

123. Parfenov VA, Mironov VA, Koudan EV, Nezhurina EK, Karalkin PA, Pereira FD, et al. Fabrication of calcium phosphate 3D scaffolds for bone repair using magnetic levitational assembly. Sci Rep. 2020;10:4013.

124. Pereira P, Neto AS, Rodrigues AS, Barros I, Miranda C, Ramalho-Santos J, et al. In Vitro Evaluation of Biphasic Calcium Phosphate Scaffolds Derived from Cuttlefish Bone Coated with Poly(ester urea) for Bone Tissue Regeneration. Polymers (Basel). 2023;15.

125. Vrchovecka K, Pavkova-Goldbergova M, Engqvist H, Pujari-Palmer M. Cytocompatibility and Bioactive Ion Release Profiles of Phosphoserine Bone Adhesive: Bridge from In Vitro to In Vivo. Biomedicines. 2022;10.

126. Vaquette C, Fan W, Xiao Y, Hamlet S, Hutmacher DW, Ivanovski S. A biphasic scaffold design combined with cell sheet technology for simultaneous regeneration of alveolar bone/periodontal ligament complex. Biomaterials. 2012;33:5560-73.

127. Misch CE, Qu Z, Bidez MW. Mechanical properties of trabecular bone in the human mandible: implications for dental implant treatment planning and surgical placement. J Oral Maxillofac Surg. 1999;57:700-6; discussion 6-8.

128. Gerhardt LC, Boccaccini AR. Bioactive Glass and Glass-Ceramic Scaffolds for Bone Tissue Engineering. Materials (Basel). 2010;3:3867-910.

129. Yan Y, Chen H, Zhang H, Guo C, Yang K, Chen K, et al. Vascularized 3D printed scaffolds for promoting bone regeneration. Biomaterials. 2019;190-191:97-110.

130. Fahimipour F, Rasoulianboroujeni M, Dashtimoghadam E, Khoshroo K, Tahriri M, Bastami F, et al. 3D printed TCP-based scaffold incorporating VEGF-loaded PLGA microspheres for craniofacial tissue engineering. Dent Mater. 2017;33:1205-16.

131. Brachet A, Belzek A, Furtak D, Geworgjan Z, Tulej D, Kulczycka K, et al. Application of 3D Printing in Bone Grafts. Cells. 2023;12.

132. Agostinacchio F, Fitzpatrick V, Dire S, Kaplan DL, Motta A. Silk fibroin-based inks for in situ 3D printing using a double crosslinking process. Bioact Mater. 2024;35:122-34.

133. Chakraborty J, Majumder N, Sharma A, Prasad S, Ghosh S. 3D bioprinted silk-reinforced Alginate-Gellan Gum constructs for cartilage regeneration. Bioprinting. 2022;28:e00232.

134. Farokhi M, Mottaghitalab F, Samani S, Shokrgozar MA, Kundu SC, Reis RL, et al. Silk fibroin/hydroxyapatite composites for bone tissue engineering. Biotechnology Advances. 2018;36:68-91.

135. Hwang HS, Lee CS. Recent Progress in Hyaluronic-Acid-Based Hydrogels for Bone Tissue Engineering. Gels. 2023;9.

136. Nguyen TB, Lee BT. A combination of biphasic calcium phosphate scaffold with hyaluronic acid-gelatin hydrogel as a new tool for bone regeneration. Tissue Eng Part A. 2014;20:1993-2004.

137. Lin Y-C, Nixon EJ, Wang H-Y, Dhawan U, Huang Y-W, Huang S-H, et al. Photocrosslinked Gelatin Methacryloyl (GelMA)/Hyaluronic Acid Methacryloyl (HAMA) Composite Scaffold Using Anthocyanidin as a Photoinitiator for Bone Tissue Regeneration. ACS Applied Polymer Materials. 2023;5:6012-21.

138. Zara JN, Siu RK, Zhang X, Shen J, Ngo R, Lee M, et al. High doses of bone morphogenetic protein 2 induce structurally abnormal bone and inflammation in vivo. Tissue Eng Part A. 2011;17:1389-99.

139. Mumcuoglu D, Fahmy-Garcia S, Ridwan Y, Nicke J, Farrell E, Kluijtmans SG, et al. Injectable BMP-2 delivery system based on collagen-derived microspheres and alginate induced bone formation in a time- and dose-dependent manner. Eur Cell Mater. 2018;35:242-54.

140. Kao D, Kubota A, Nevins M, Fiorellini J. The Negative Effect of Combining rhBMP-2 and Bio-Oss on Bone Formation for Maxillary Sinus Augmentation. Int J Periodontics Restorative Dent. 2012;32:61-7.

141. Li F, Yu F, Liao X, Wu C, Wang Y, Li C, et al. Efficacy of Recombinant Human BMP2 and PDGF-BB in Orofacial Bone Regeneration: A Systematic Review and Meta-analysis. Sci Rep. 2019;9:8073.

142. Li F, Yu F, Xu X, Li C, Huang D, Zhou X, et al. Evaluation of Recombinant Human FGF-2 and PDGF-BB in Periodontal Regeneration: A Systematic Review and Meta-Analysis. Sci Rep. 2017;7:65.

143. Bai Y, Yin G, Huang Z, Liao X, Chen X, Yao Y, et al. Localized delivery of growth factors for angiogenesis and bone formation in tissue engineering. Int Immunopharmacol. 2013;16:214-23.

144. Kwon B, Jenis LG. Carrier materials for spinal fusion. Spine J. 2005;5:224S-30S.

145. Farokhi M, Mottaghitalab F, Shokrgozar MA, Ou KL, Mao C, Hosseinkhani H. Importance of dual delivery systems for bone tissue engineering. J Control Release. 2016;225:152-69.

146. Schliephake H, Weich HA, Dullin C, Gruber R, Frahse S. Mandibular bone repair by implantation of rhBMP-2 in a slow release carrier of polylactic acid--an experimental study in rats. Biomaterials. 2008;29:103-10.

147. Luca L, Rougemont AL, Walpoth BH, Gurny R, Jordan O. The effects of carrier nature and pH on rhBMP-2-induced ectopic bone formation. J Control Release. 2010;147:38-44.

148. Novak S, Madunic J, Shum L, Vucetic M, Wang X, Tanigawa H, et al. PDGF inhibits BMP2-induced bone healing. NPJ Regen Med. 2023;8:3.

149. Wang X, Matthews BG, Yu J, Novak S, Grcevic D, Sanjay A, et al. PDGF Modulates BMP2-Induced Osteogenesis in Periosteal Progenitor Cells. JBMR Plus. 2019;3:e10127.

150. Tokunaga A, Oya T, Ishii Y, Motomura H, Nakamura C, Ishizawa S, et al. PDGF receptor beta is a potent regulator of mesenchymal stromal cell function. J Bone Miner Res. 2008;23:1519-28.

151. Baino F, Hamzehlou S, Kargozar S. Bioactive Glasses: Where Are We and Where Are We Going? J Funct Biomater. 2018;9.

152. Hench LL. The story of Bioglass. J Mater Sci Mater Med. 2006;17:967-78.

153. Bellucci D, Salvatori R, Giannatiempo J, Anesi A, Bortolini S, Cannillo V. A New Bioactive Glass/Collagen Hybrid Composite for Applications in Dentistry. Materials (Basel). 2019;12.

154. Jones JR. Review of bioactive glass: from Hench to hybrids. Acta Biomater. 2013;9:4457-86.

155. Skallevold HE, Rokaya D, Khurshid Z, Zafar MS. Bioactive Glass Applications in Dentistry. Int J Mol Sci. 2019;20.

156. Shuai C, Cao Y, Gao C, Feng P, Xiao T, Peng S. Hydroxyapatite whisker reinforced 63s glass scaffolds for bone tissue engineering. Biomed Res Int. 2015;2015:379294.

157. Tavakolizadeh A, Ahmadian M, Fathi MH, Doostmohammadi A, Seyedjafari E, Ardeshirylajimi A. Investigation of Osteoinductive Effects of Different Compositions of Bioactive Glass Nanoparticles for Bone Tissue Engineering. ASAIO J. 2017;63:512-7.

158. Zhang C, Chen S, Vigneshwaran M, Qi Y, Zhou Y, Fu G, et al. Effect of Different Contents of 63s Bioglass on the Performance of Bioglass-PCL Composite Bone Scaffolds. Inventions. 2023;8:138.

159. Wu C, Zhang Y, Zhou Y, Fan W, Xiao Y. A comparative study of mesoporous glass/silk and non-mesoporous glass/silk scaffolds: physiochemistry and in vivo osteogenesis. Acta biomaterialia. 2011;7:2229-36.

160. Nguyen LH, Annabi N, Nikkhah M, Bae H, Binan L, Park S, et al. Vascularized bone tissue engineering: approaches for potential improvement. Tissue Eng Part B Rev. 2012;18:363-82.

161. Liu X, Zhao N, Liang H, Tan B, Huang F, Hu H, et al. Bone tissue engineering scaffolds with HUVECs/hBMSCs cocultured on 3D-printed composite bioactive ceramic scaffolds promoted osteogenesis/angiogenesis. J Orthop Translat. 2022;37:152-62.

162. Chen J, Deng L, Porter C, Alexander G, Patel D, Vines J, et al. Angiogenic and Osteogenic Synergy of Human Mesenchymal Stem Cells and Human Umbilical Vein Endothelial Cells Cocultured on a Nanomatrix. Scientific reports. 2018;8:15749.

163. Piard C, Jeyaram A, Liu Y, Caccamese J, Jay SM, Chen Y, et al. 3D printed HUVECs/MSCs cocultures impact cellular interactions and angiogenesis depending on cell-cell distance. Biomaterials. 2019;222:119423.

164. Vimalraj S, Arumugam B, Miranda PJ, Selvamurugan N. Runx2: Structure, function, and phosphorylation in osteoblast differentiation. International journal of biological macromolecules. 2015;78:202-8.

165. Komori T. Regulation of Proliferation, Differentiation and Functions of Osteoblasts by Runx2. International journal of molecular sciences. 2019;20.

166. Wang Y, Yan W, Lu X, Qian C, Zhang J, Li P, et al. Overexpression of osteopontin induces angiogenesis of endothelial progenitor cells via the avbeta3/PI3K/AKT/eNOS/NO signaling pathway in glioma cells. Eur J Cell Biol. 2011;90:642-8.

167. Perepletchikova D, Malashicheva A. Communication between endothelial cells and osteoblasts in regulation of bone homeostasis: Notch players. Stem Cell Res Ther. 2025;16:56.

168. Chakraborty G, Jain S, Kundu GC. Osteopontin promotes vascular endothelial growth factor-dependent breast tumor growth and angiogenesis via autocrine and paracrine mechanisms. Cancer Res. 2008;68:152-61.

169. Carvalho MS, Silva JC, Cabral JMS, da Silva CL, Vashishth D. Cultured cell-derived extracellular matrices to enhance the osteogenic differentiation and angiogenic properties of human mesenchymal stem/stromal cells. J Tissue Eng Regen Med. 2019;13:1544-58.

170. Lorencetti-Silva F, Arnez MFM, Thome JPQ, Carvalho MS, Carvalho FK, Queiroz AM, et al. Leukotriene B4 Loaded in Microspheres Inhibits Osteoclast Differentiation and Activation. Braz Dent J. 2022;33:35-45.